SERS nanosensors for real time multiplexing of intracellular hydrogen peroxide and pH dynamics

Can Xiao

TESI DOCTORAL UPF / 2021

Thesis supervisor:

Dra. Pilar Rivera Gil

THESIS DEPARTMENT:

DEPARTMENT OF EXPERIMENTAL AND HEALTH SCIENCES

Universitat Pompeu Fabra Barcelona

This Thesis was supported by the Ministry of Science, Innovation and Universities (MICINN) (PID2019-106755RB-I00/AEI/10.13039/501100011033, CTQ2013-45433-P[FEDER], MAT2016-75362-C3-2-R).

Can Xiao acknowledges the Chinese Scholarship Council for financial support (NSCIS No: 201609110104).

ACKNOWLEDGMENTS

I still remember the moment when I decided to pursue my PhD degree abroad in Spain. It was hard to make the decision at the very beginning considering I am going to stay here in Spain for approx. four years with all my families in China. Many thanks to my families. With their support and encouragement, I could enjoy my adventure here in Barcelona.

My supervisor Dr. Pilar Rivera Gil from UPF helps me a lot in scientific field and in life here. Her passion about work and her open mind thinking give me deep impressions. She always encourages me about my experiments and she offered me many opportunities to practice my speaking skills. I feel grateful for her help and support, and our relations will be a great treasure. I also would like to thank Dr. Victor Izquierdo Roca. He showed his great patient to me while introducing me knowledges about Raman and the skills for data processing. Many thanks to Dr. Bernat Mir, with his technical help, lab time was much easier. And I also miss the time we enjoyed different kinds of food together.

Many thanks and kisses to my colleagues. Special thanks to Yolanda who always supports me with technical and administrative help, and gives me advices for living in Barcelona. I missed her cookies for Happy Chinese New Year. Thanks to Dr. Marcos Sanles, Dr. Dionysia Tsoutsi, Dr. Muriel Rovira, Dr. Oihane Fragueiro, Dr. Markus Martincic and Dr. Vladimir Mulens for their professionally personal support. Thanks to my lab colleagues Paula Zamora, Ruixue Xu, Weiteng An, and Ting Zhou for their

friendship. We enjoyed great time here in our lab and office. We shared the culture exchange. We enjoyed the food, the beer and the beautiful holidays together. Those memories will last in my mind.

Many thanks to Javi and the rest of the laboratory members of Dr. David Andreu group. Thanks for their kindness and friendship which made lab life colorful.

Many thanks to my collaborators: the Translational Synthetic Biology group led by Dr. Marc Güell Cargol, and the MISTRAL group of the ALBA synchrotron led by Dr. Eva Pereiro. Especially to Maria Pallarès and Nastassia Knödlseder, and Dr. Javier Conesa, many thanks to their help. I really enjoyed the time we working together.

Thanks also to the CRG (Xavi, Raquel, Arrate, Timo) and Flow cytometry unit (Oscar, Eva) for their kindness support with each technology. Thanks to the administrative staff of UPF and PRBB, they helped me a lot and made my life in PRBB much easier and happier. Thanks to their contribution.

Many thanks to my committee members Dr Andreu Cabot Codina, Dr. Jordi Garcia Ojalvo, Dr. Duncan Graham, Dr. Elena Hidalgo Hernando and Dr. Victor Izquierdo Roca, for taking the time out of their busy schedule to review my thesis.

I got my economic support from China Scholarship Council (CSC) which allows me study abroad and makes my life here in Barcelona much easier. Thanks to this support.

Finally, I want to thank all the people helped me during my life in Barcelona. During these four years, I learned a lot from all the people I met. I enjoyed a lot the climate, the beach and the culture here in Spain. These four years of experience not only trained me better in scientific field, but also broaden my mind on understanding the world. I wish a better future for all.

ABSTRACT

The existence and progression of certain diseases are associated with the imbalances of different biomolecules. The multiplex sensing of hydrogen peroxide and pH can be potentially used for understanding the progression of certain diseases (*e.g.*, Alzheimer's disease) and applied for diagnosis. In this thesis, nanosensors based on surface-enhanced Raman scattering (SERS) were provided for real time multiplexing of intracellular hydrogen peroxide and pH dynamics.

We systematically studied the fundamental factors and the impact aspects for the synthesis and modification of metallic nanostructure as SERS platform. Then we synthesized gold silica nanocapsules which anchored ensembles of interparticle hot spots in their inner surface offering robust Raman signals. The performance of 3-mercaptophenylboronic acid and 4-mercaptobenzoic acid modified gold silica nanocapsules coupling with SERS was further verified for multiplexing intracellular hydrogen peroxide and pH monitoring under different conditions. Facile and reliable multiplex nanosensors for intracellular hydrogen peroxide and pH were reported here.

RESUMEN

El desarrollo de determinadas enfermedades se asocia a los desequilibrios de diferentes biomoléculas. La detección múltiple del peróxido de hidrógeno y el pH puede usarse potencialmente para comprender la progresión de ciertas enfermedades y su diagnóstico como la enfermedad de Alzheimer. En esta tesis, se desarrollaron nanosensores para La espectroscopía Raman de superficie mejorada (del inglés SERS) para la detección concomitante de las dinámicas del peróxido de hidrógeno y del pH intracelulares en tiempo real.

Estudiamos los factores fundamentales que afectan la síntesis y modificación de nanoestructura metálica como plataforma *SERS*. Luego, sintetizamos nanocápsulas de sílice y oro provistos de conjuntos de puntos calientes entre partículas en su superficie interna que ofrecen señales Raman robustas. Se verificó el rendimiento de la señal Raman para la detección concomitante del peróxido de hidrógeno intracelular y la monitorización del pH en diferentes condiciones, usando nanocápsulas de sílice y oro modificadas con ácido 3-mercaptofenilborónico y ácido 4-mercaptobenzoico. Reportamos el uso de nanosensores múltiples, fáciles y fiables, para la detección del peróxido de hidrógeno y el pH intracelulares.

PREFACE

This Doctoral Thesis entitled ¨SERS nanosensors for real time multiplexing of intracellular hydrogen peroxide and pH dynamics¨ comprises two different research articles (in preparation) and is divided into chapters. The main content of these chapters will be introduced briefly below.

Chapter 1 introduces the fundamental theories of Raman and SERS which are the theoretical supporting of our methods. The state of the art of hydrogen peroxide and its measurements and limitations were discussed. Multiplexing technologies based on SERS for hydrogen peroxide and more intracellular species (here pH) are proposed under these circumstances.

Chapter 2 presents the work of ¨Synthesis and applications of SERS encoded silver silica nanocomposites¨. In this chapter we systematically studied the synthesis and modification of one designed nanostructure which made of silver silica nanocomposites. We studied the fundamental factors, including pH and solvent for the modification of metallic surface. Then different aspects were discussed for the final packing quality, including the metal-thiol bonding formation speed under specific conditions, the electrostatic repulsion on the metallic surfaces and the competition between Raman probes and thiolated stabilizers. Also controlled method to create ¨hot spots¨ resulting the increase of Raman enhancement and the protection layer were applied and discussed. The performance of this nanostructure was validated by SARS-CoV-2 detection with SERS-based ELISA assay. One robust nanostructure as SERS

platform is detailed introduced including the design, the synthesis, the modification and its potential applications. This nanostructure gives us the idea and direction for a controlled synthesis of nanostructures for multiplexing intracellular species monitoring.

Chapter 3 presents the work of ¨Real time and spatiotemporal quantification of hydrogen peroxide and pH imbalances with a multiplex SERS nanosensor¨. In this chapter we provided a plasmonic multiplex nanosensor for reliable *in vitro* hydrogen peroxide and pH determination based on 3-mercaptophenylboronic acid and 4-mercaptobenzoic acid functionalized gold/silica nanocapsules coupled with surface-enhanced Raman spectroscopy, to meet the requirement of the facile devices for potential diseases monitoring (*e.g.,* Alzheimer's disease) based on intracellular hydrogen peroxide and pH measurements. pH effect on the oxidation of 3-mercaptophenylboronic acid by hydrogen peroxide was studied since the complexation of this boronic acid with a third hydroxyl group makes this reaction base promoted. We should highlight here that the pH effect can be further applied to all hydrogen peroxide measurements which are based on aromatic boronic acid oxidation. We validated the performance of this nanosensors under different conditions and studied the concentration gradient between intracellular and extracellular hydrogen peroxide. This multiplex nanosensor has the potential to be applied for diseases monitoring.

Chapter 4 summarizes the conclusions of this Thesis.

Table of contents

	Pag.
ACKNOWLEDGMENTS.....	v
ABSTRACT.....	ix
RESUMEN.....	xi
PREFACE.....	xiii
1. INTRODUCTION.....	1
1.1 RAMAN.....	1
1.2 SERS.....	5
1.3 MULTIPLEX SERS.....	9
1.4 HYDROGEN PEROXIDE.....	12
1.5 REFERENCES.....	16
2. SYNTHESIS AND APPLICATIONS OF SERS ENCODED SILVER SILICA NANOCOMPOSITES.....	25
2.1 ABSTRACT.....	25
2.2 INTRODUCTION.....	26
2.3 EXPERIMENTAL SECTION.....	29
2.3.1 Materials and Reagents.....	29
2.3.2 Silver and gold nanoparticles synthesis.....	29
2.3.3 Modification and controllable agglomeration of AgNPs and AuNPs.....	30
2.3.4 SiO_2 encapsulation.....	32
2.3.5 AgNPs@MBA@SiO_2 deposited materials preparation.....	33
2.3.6 Antibody immobilization on AgNPs@MBA@SiO_2.....	34
2.3.7 SERS based Elisa biosensing.....	35
2.4 RESULTS AND DISCUSSION.....	36
2.4.1 AgNPs@MBA@SiO_2 synthesis and characterization.....	37
2.4.2 AgNPs@MBA@SiO_2 SERS signal robustness analysis.....	44
2.4.3 SERS based ELISA for sensing spike protein of SARS-CoV-2.....	47
2.5 CONCLUSION.....	50
2.6 REFERENCES.....	51

2.7 SUPPORTING INFORMATION..... 56

3. REAL TIME AND SPATIOTEMPORAL QUANTIFICATION OF PH AND HYDROGEN PEROXIDE IMBALANCES WITH A MULTIPLEX SERS NANOSENSOR..... 65
3.1 ABSTRACT..... 65
3.2 INTRODUCTION..... 66
3.3 EXPERIMENTAL SECTION..... 70
3.3.1 Materials and Reagents..... 70
3.3.2 NCs synthesis..... 71
3.3.3 Morphological characterization..... 72
3.3.4 SERS sensor preparation..... 72
3.3.5 SERS measurements..... 73
3.3.6 Cell culture and viability assay..... 74
3.3.7 *In vitro* experiments..... 74
3.4 RESULTS AND DISCUSSION..... 75
3.4.1 Synthesis and characterization of 3-MPBA modified NCs..... 75
3.4.2 NCs cell internalization and biocompatibility..... 79
3.4.3 Influence of pH on NCs@3-MPBA H_2O_2 sensing..... 81
3.4.4 Synthesis of a multiplex sensor to study pH and H_2O_2 interrelation..... 84
3.4.5 Intracellular and extracellular H_2O_2 monitoring with NCs@3-MPBA..... 88
3.4.6 Intracellular and extracellular H_2O_2 and pH monitoring with NCs@3-MPBA&4-MBA..... 90
3.5 CONCLUSION..... 95
3.6 REFERENCES..... 96
3.7 SUPPORTING INFORMATION..... 103
3.7.1 Section 1: Synthesis and characterization of 3-MPBA modified NCs..... 103
3.7.2 Section 2: NCs cell internalization and biocompatibility..... 105
3.7.3 Section 3: Influence of pH on NCs@3-MPBA H_2O_2 sensing..... 107
3.7.4 Section 4: Synthesis of 3-MPBA and 4-MBA modified NCs and detection of H_2O_2 and pH in phosphate buffered saline..... 111

3.7.5 Section 5: Intracellular and extracellular H_2O_2 monitoring with NCs@3-MPBA..... 116
3.7.6 Section 6: Intracellular and extracellular H_2O_2 and pH monitoring with NCs@3-MPBA&4-MBA..... 119

4. CONCLUSIONS..... 127

1. INTRODUCTION

1.1 Raman

In 1923, Smekal hypothesized the phenomenon of inelastic scattering of light, and then in 1928 this phenomenon was experimentally observed by Raman and Krishnan, which is referred to Raman scattering[1].

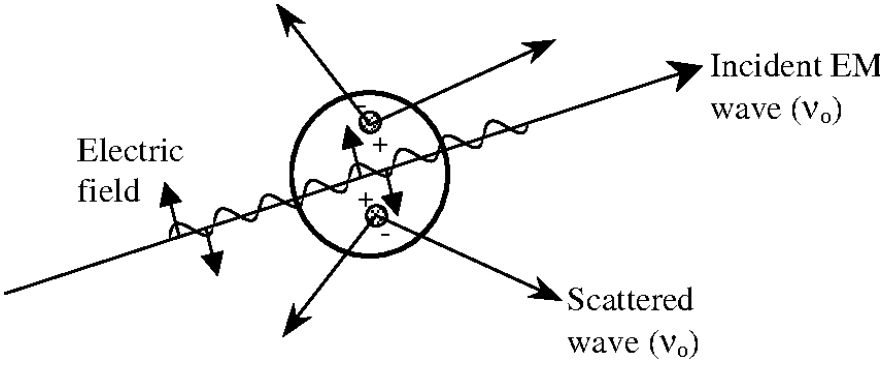

Figure 1: Light scattering process by an induced dipole moment during the interaction of incident proton and molecules. Reproduced from reference[2].

Incident light or photons can be absorbed or scattered by molecules. When incident photons interact and scatter from molecules, scattering happens. With an angle between incident beam, scattering can be observed and collected. The efficiency of scattering is proportional to the fourth power of the incident energy [1]. When the interaction between incident light (also can be called as electromagnetic wave) and molecules happens, molecules electron orbits can be perturbed periodically by the electric field of the incident electromagnetic (EM) wave with the same frequency. This

will form a ¨virtual state¨ and result in induced dipole moment, as the electron cloud are perturbed and oscillating (see Figure 1)[2], which will further become the source of electromagnetic radiation resulting in scattered light. The majority of the scattered light has the same frequency as the incident light. This elastic scattering process only involves electron cloud distortion, and can be called Rayleigh scattering for molecules. Inelastic scattering process occur when nuclear motion is induced, and energy transfer from incident light to molecules or from molecules to scattered light happens. This small fraction (around 1 per 10^6 to 10^8 photons) of the scattered light is emitted at different frequencies as incident light with one vibrational unit of energy. Raman scattering is the inelastic scattering of photons which is an inherently weak process. Figure 2 [1] shows the Rayleigh and Raman scattering processes. Majority of the scattered light is Rayleigh scattering without energy exchange. The majority of the molecules are in their lowest vibrational energy level (shown in m) at room temperature. The energy of ¨virtual states¨, which are created when polarization occurs, is determined by the incident light frequency. If vibrational energy is gained by a molecule lading the process from ground vibrational state (m) to excited vibrational state (n) with scattered photons shifted to lower energy, Stokes Raman scattering occurs. While, for the fraction of excited molecules, the process from excited states to ground state is anti-Stokes Raman scattering, in which the scattered light shifted to higher energy. The proportion between Stokes and anti-Stokes Raman scattering is determined by the molecules energy distribution which is a factor affected by the temperature.

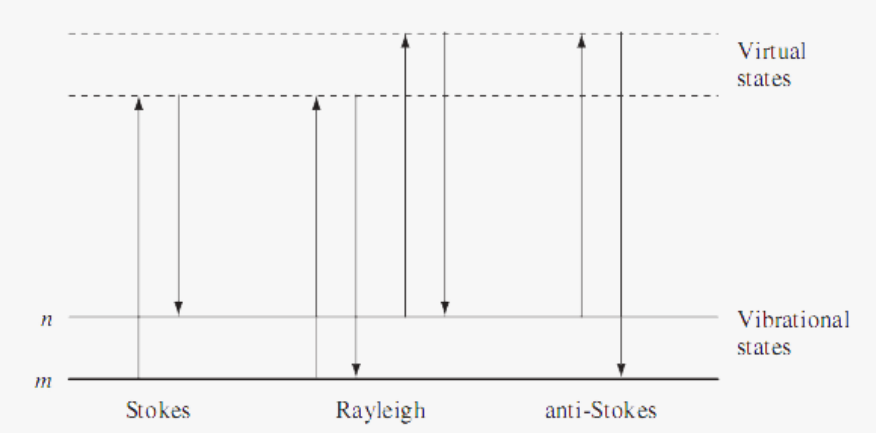

Figure 2: Rayleigh and Raman scattering processes, with the ground vibrational state indicated with m, and vibrational states indicated with n. Reproduced from reference[1].

Infrared spectroscopy, in which molecules are excited to a higher vibrational state with the absorption of matched incident irradiation, is a different technology as Raman spectroscopy. As shown in Figure 2, infrared absorption occurs when a molecule is excited by incident proton with exactly matched energy and directly process from ground state (m) to excited vibrational state (n) happens. While Raman scattering happens without incident light matching the energy differences between vibrational states. Intense Raman scattering happen when vibrations induce the polarizability changes of molecules. While infrared absorption is resulted by changes in dipole. Those two techniques are complementary for better understanding of molecule structure.

The relations between the strength of this induced dipole moment (P) by the electric field (E) of incident electromagnetic wave during the incident proton and molecules interaction and the polarizability (α) of a molecule can be described by Equation 1.

$$P = \alpha \bar{E} \quad (Eq.1)$$

The polarizability is a factor for measuring the ease of electron cloud to be distorted, which is an inherent property of molecule structure. Raman scattering happens only when the polarizability of molecules changes during the process, which is the selection rule for Raman-active vibration. The polarizability derivative (dα /dQ) is used for describing the changes and the selection rule can be described by Equation 2, in which Q is the normal coordinate of the vibration [2].

$$\frac{d\alpha}{dQ} \neq 0 \quad (Eq.2)$$

The molecular structure information of the sample is revealed by the shifted frequencies of Raman scattered light. Raman shift is determined by vibrational energy difference as shown in Figure 2, and is calculated through Equation 3, in which the $\lambda_{incident}$ and $\lambda_{scattered}$ are the wavelengths (cm) of the incident photons and Raman scattered photons, separately.

$$\Delta \bar{v} = \frac{1}{\lambda_{incident}} - \frac{1}{\lambda_{scattered}} \quad (Eq.3)$$

The four main components for a typical Raman spectroscopy system include laser for illumination, optics for light collection, filter or spectrophotometer to separate Raman scattering from incident light and detector for frequency measurements (see Figure 3)[3]. For bio-applications, near infrared excitation is commonly used, as near infrared light has less mutagenic effect and deeper penetration, and also minimized fluorescence interfere[4].

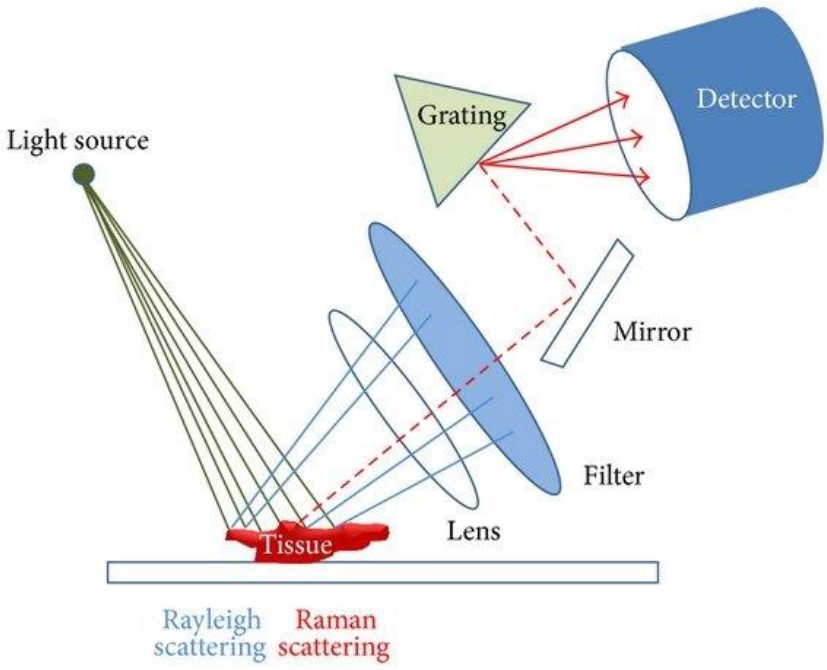

Figure 3: Schematic diagram of Raman spectroscopy instrument. Excitation light (in green line), Rayleigh scattering (in blue line) and Raman scattering (in red dotted line). Reproduced from reference[3].

1.2 Surface-Enhanced Raman spectroscopy

Taking into account the low cross-section of Raman scattering (around 10^{-31}~10^{-26} cm^2 per molecule)[5], its application has been further broadened with the discovery of surface-enhanced Raman spectroscopy (SERS).

SERS was first reported by Fleischmann and his co-workers in 1974 and this high intensity of signal was explained by the absorption sites increase on a roughened surface[6]. Later in 1977, the theory started to be developed by the groups of Van Duyne[7], and Moskovits[8] confirming the increase of cross section of molecules.

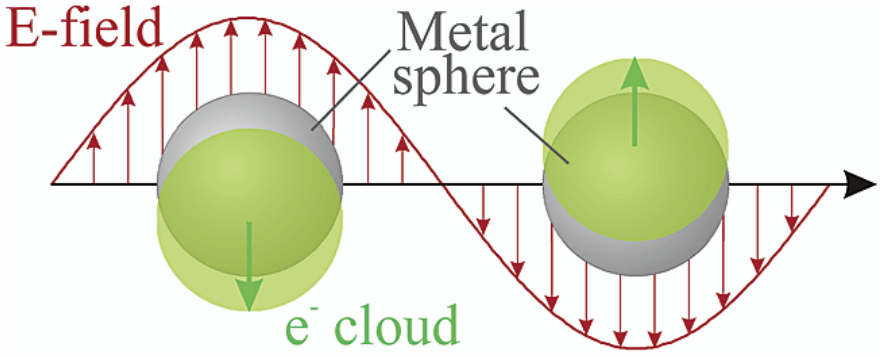

Figure 4: Scheme representing the plasmon oscillations with metal spheres induced by electromagnetic wave. Reproduced from reference [9].

In comparison with Raman, in general, average enhancement factors for typical SERS are amplified by 10^6 to 10^8 orders of magnitude[10]. Thus SERS is a sensitive technology allowing low concentration analytes detection. Both the interaction between light and molecules for Raman and the interactions between light and nanostructure which is SERS platform need to be considered to understand SERS. The electromagnetic and the chemical mechanisms are the two enhancement mechanisms for SERS phenomenon. The electromagnetic enhancement is caused by the appearance of localized surface plasmon resonances (LSPR), which will offer enhanced localized electromagnetic fields, as seen in Figure 4 using metal sphere nanoparticle representing the plasmon oscillations with the displacement of electron cloud induced by the light[9]. Those electromagnetic fields which localized within few nanometers of the metallic surface decay exponentially from the surface. Only the molecules which are located close to the metallic surface can be SERS active. The electromagnetic enhancement is

the dominant contributor to SERS processes since this enhancement provides factors generally 10^4-10^5 [11]. The chemical enhancement involves resonant charge transfer between molecules and metal[12]. Chemical enhancement is molecular dependent which can contribute 10^2-10^3 to the enhancement factor theoretically.

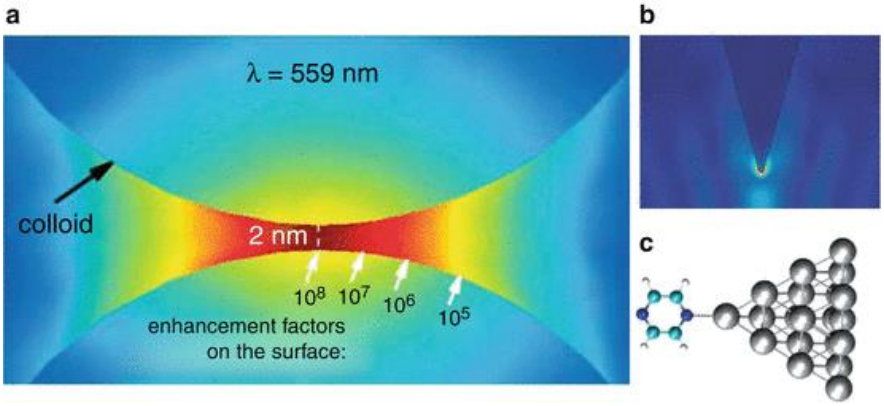

Figure 5: Reported types of generic hot spots. (a) hot spots formed between two close located nanoparticles (b) hot spot formed at a sharp tip of nanostructures and (c) hot spots formed with strongly chemical absorbed molecules onto metal surfaces. Reproduced from references[10,13,14,15].

Moreover, this enhancement can be further increased by hot spots. Those highly localized regions of intense local field enhancement which are caused by LSPR are called ¨hot spots¨ [10]. Hot spots could increase enhancement factor of SERS signal up to 10^{15} orders of magnitude [16]. Thus it is critical important to control the hot spots in order to obtain robust SERS signal. Hot spots can be formed within the interstitial crevices of metallic nanostructures. Reported different type of hot spots are shown in Figure 5[10,13,14,15]. The first type of hot spots is caused by the plasmonic coupling of the particles when they are very close to each other. And the second type of hot spots is formed at the sharp tips of specific

nanostructures, like nanostars. And the third type of hot spots is built at the chemical bonding sites with highly chemical absorbed molecules onto metal surfaces. Hot spot can potentially dominate the property of SERS active substrates with sufficient density, which will play a key role in low concentration analytes detection.

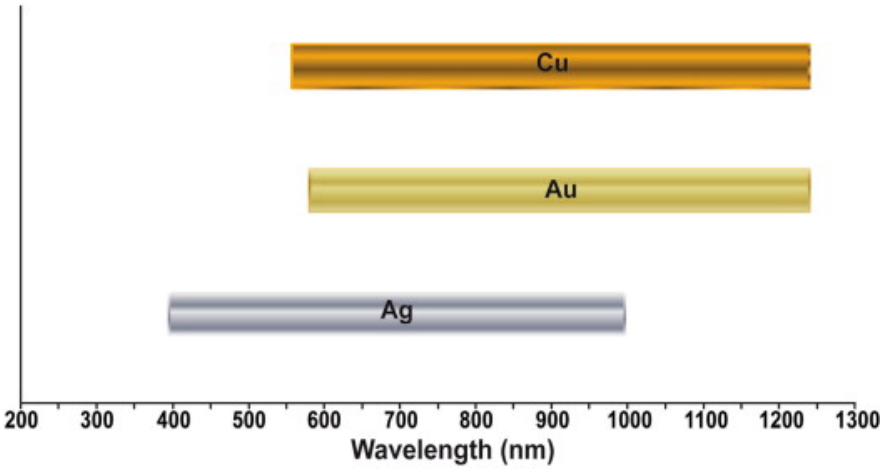

Figure 6: Approximate wavelength ranges for Ag, Au, and Cu materials supporting SERS. Reproduced from reference[17].

Plasmonic nanostructure is the core factor for SERS. Generally, gold silver and copper are the classic materials for SERS, since they offer high field enhancement in the visible to near infrared wavelength range, as shown in Figure 6[17]. Also gold and silver are more commonly used as they have better air stability. Plasmonic nanostructure as an integral component is necessary for SERS. Figure 7 shows one typical SERS device using Au/Ag nanoparticles as example[8].

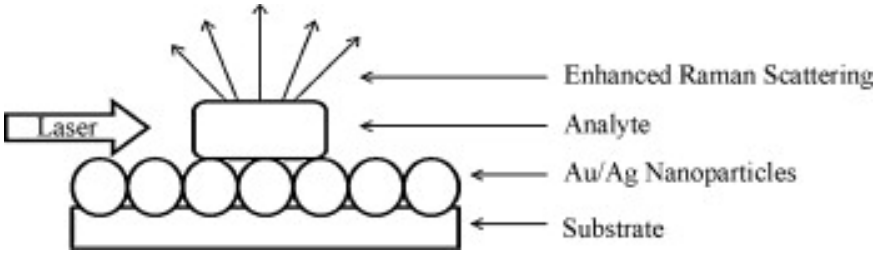

Figure 7: Scheme representing surface-enhanced Raman scattering devices. Reproduced from reference[8].

SERS spectroscopy is a powerful analytical technology which can be used for single molecule detection under ambient conditions[18]. The unique advantages for SERS quantifying bioanalytes directly from aqueous environments make it a nondestructive technology. The biocompatibility of SERS platform made of gold nanometrails allows *in vitro* and *in vivo* SERS detection [19]. Thus SERS has been widely used for qualitative and quantitative detection of biological species and diseases, including RNA[20], enzyme[21], small molecules (*e.g.,* hydrogen peroxide13[22]) and others (*e.g.,* staphylococcal enterotoxin B14[23]).

1.3 Multiplex SERS

Sensitive and selective biosensor has great importance in human health care. Compared with classical bioanalytical methods which always involved the determination of a single analyte, multiplex technologies allow simultaneous investigation of mutiple analytes within one samples[24]. Certain number of biomolecules or biomarkers can be involved into the progression of a disease. More accurate diagnosis can be made by detecting multiple biomarkers.

Multiplex sensing provides more information within short time and limited samples. Therefore, multiple technologies can achieve rapid and accurate diagnosis, and show great potential in human disease monitoring and medical care [25].

Many analytical technologies can be applied for multiplexing, including fluorescence spectroscopy[26], electrochemical sensing[27], colorimetric detection[28], UV-vis[23], Rayleigh scattering[23], *etc*. In general, molecular structure and composition can be obtained by applying light and analyzing the interaction between light and molecules for spectroscopy. Therefore, spectroscopy has attracted more interest in multiplexing. Compared with other technologies, SERS is an ideal technology for multiplexing, offering extremely low detection limits and characteristic fingerprint spectra information, as shown in Figure 8[23] the basic concept of multiplex SERS. Electrochemical sensing has its own issues with interference and non-specific adsorption. Fluorescent signals are characterized by a broad and simple structure, and resulting broad fluorescence emission bands. While, for SERS multiplex, without sample preparation, narrow width peaks offering characteristic structural information are obtained even with lower detection limit than fluorescence[26]. Similar things happen when comparing colorimetric sensing with SERS[28]. Microarrays combined SERS also has been investigated for diagnosis, to achieve desired sensitivity with high-throughput capabilities[29]. In summary, SERS multiplex analysis can be performed directly in aqueous environment with minimal sample preparation, which makes SERS great potential for clinical diagnosis, as water has extremely low Raman cross-section[30].

Furthermore, characteristic vibrational information obtained by SERS are fingerprint information of molecular structure, which makes SERS a selective multiplex detection technology. Also, SERS is an ultrasensitive detection technology which has the potential for single molecule analysis, allowing extremely low detection limit and more importantly, real-time multiplexing applications [23].

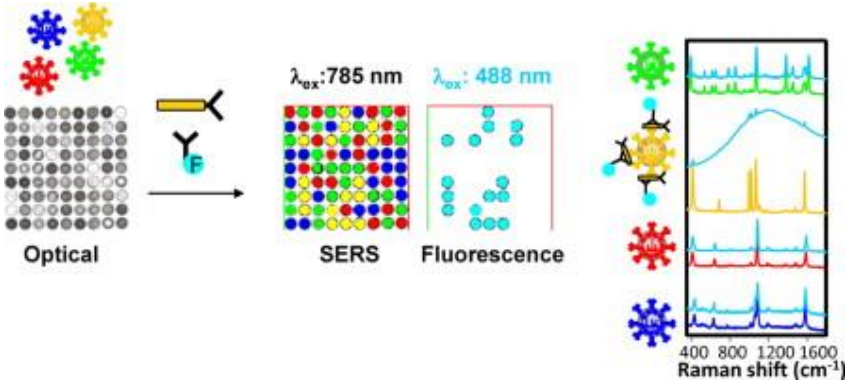

Figure 8: Schematic illustration of multiplex SERS technology. Reproduced from reference[23].

Multiplex SERS can be categorized into direct methods and indirect methods. Performing SERS multiplex analysis by incubating samples directly onto the surface of SERS platform is direct methods, which is restricted by the complexity of real samples. The more commonly used methods are indirect methods by using functionalized or encoded SERS nanostructures. Depending on the targeted analytes, this functionalized or encoded SERS nanostructure can be ligands functionalized or biomolecule encoded[23]. Since the distance between the SERS platform and targeted or sensing analytes is critical for the signal enhancement, to

ensure the distance of targeted analytes, molecules functionalized with thiol or amine groups are normally used for the functionalization of SERS platform.

The performance of SERS in multiplexing has been validated in biodiagnosis. Lin et al. designed geometrically metal carbonyl encoded SERS nanobarcodes for the detection of nasopharyngeal carcinoma biomarkers which could potentially use in clinical diagnosis and help physicians understanding the progression and design for follow-up treatment[31]. Wu et al. reported a magnetically assisted sandwich type nanostructures for multiplexing three microRNA for early diagnosis and prognosis of Hepatocellular Carcinoma[32]. Zhang et al. proposed a multiplexing of three cardiac biomarkers by using a lateral flow assay with silver gold core shell nanoparticles for the early diagnosis of acute myocardial infarction[33]. SESR has shown its great performances as a diagnosis tool and its future for clinical applications.

1.4 Hydrogen peroxide

Reactive oxygen species (ROS) involve in many biological effects, covering physiological regulatory functions and pathological progression. ROS are the metabolic products and play key role in oxidative regulation, including immune defense, antibacterial action and signal transduction. While, under imbalance states, this metabolic disorders could result in such as chronic inflammation, aging, cancer[34] and neurodegenerative disorder (*e.g.,* Alzheimer disease[35]).

Among all the reactive oxygen species, mainly including these four species: hydroxyl and peroxy radicals, superoxide anions, and hydrogen peroxide (H_2O_2), H_2O_2 is an outstanding signaling molecule because of its unique physicochemical properties[36]. H_2O_2 has relatively long lifetime in aqueous environments as it is not a high reactive radical. Uncharged feature allows H_2O_2 diffusion and transportation across membrane and further to realize remote signaling. Also, high concentrations of H_2O_2 are needed to oxidize targeted protein, which makes the oxidation by H_2O_2 locally at the high concentration site and easier to be monitored. H_2O_2 is considered as the most suitable signaling messenger for redox signaling[37]. Thus, H_2O_2 has attracted interest and become the major redox metabolite in redox biology. In mammalian cells, physiological concentration of H_2O_2 high likely ranges from 1 to 700 nM, supraphysiological and pathological level of H_2O_2 will lead to damage of biomolecules, and resulted in stress and adaptive stress responses, even inflammatory responses and cell death[38]. Figure 9[39] shows the role H_2O_2 playing in oxidative stress. Endogenous H_2O_2 sources are identified by many one- or two-electron reduction reactions with the generators including NADPH oxidases and other oxidases. Also in mitochondria, H_2O_2 can be converted from superoxide anion radials by three superoxide dismutases, SODs. And then with the help of aquaporins, H_2O_2 can diffuse and transport across the membranes for further functions. Under physiological conditions, H_2O_2 perticipates redox signaling (shown in green) and under pathophysiological conditions, H_2O_2 causes oxidative distress and diseases (shown in red). The

measurements of intracellular H_2O_2 is a focused topic in redox biology, with the purpose to understand redox reactions and design redox therapeutics.

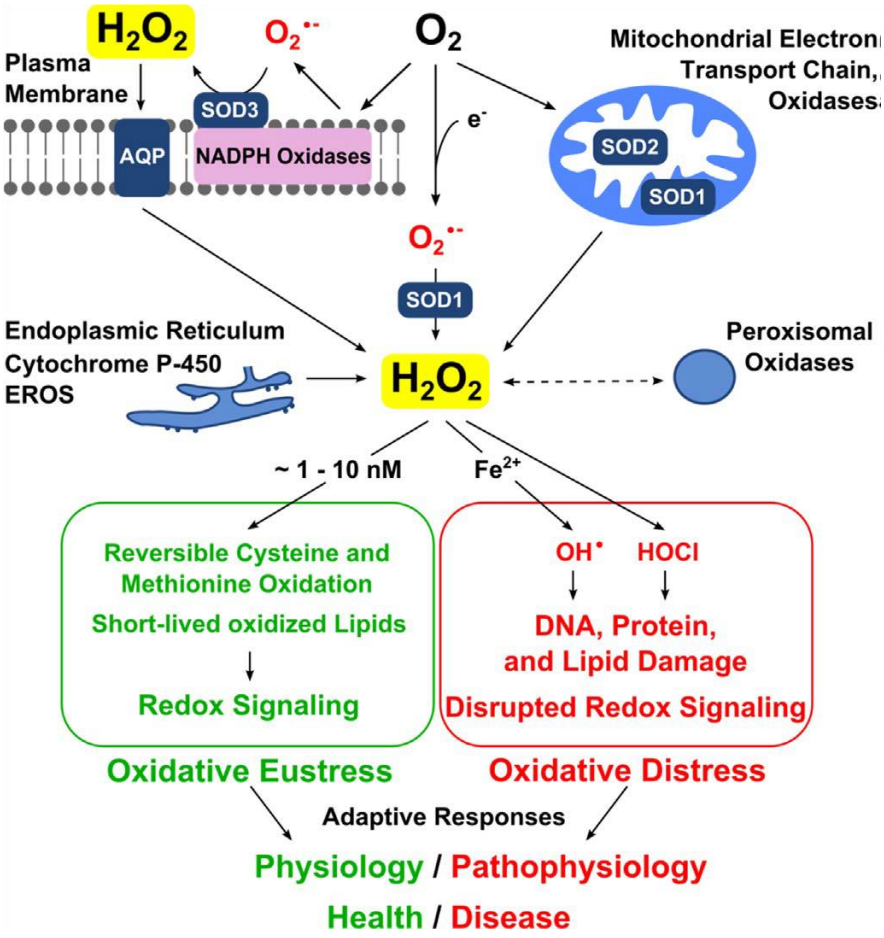

Figure 9: Hydrogen peroxide in oxidative stress. Reproduced from reference[39].

The classical methods are using fluorescent dyes to identify the concentration of H_2O_2. The most commonly used methods are based on horseradish peroxide (HRP)-dependent probes[36]. However, most of those HRP-dependent probes is restricted for extracellularly available H_2O_2 determination[36]. Genetically encoded fluorescent

protein indicators are designed to meet the need of intact cells and tissues H_2O_2 detection. HyPer probes[40] and roGFP-orp1[41] are those ones outstanding with the potential for spatiotemporal H_2O_2 detection. While, hyper probes are pH interfered, and roGFP-orp1 are used with lentivirus transfected cells. Fluorescent probes are complicated synthesized, and photo-bleaching and photo-toxicity may happen during manipulation. Further, it is hard to realize *in situ* quantification[36]. All those features hamper their popularity.

SERS based methods nowadays attract interest, and people are making the efforts to design suitable nanostructures for intracellular spatiotemporal H_2O_2 quantification. Boronate molecules are mostly used Raman probes for H_2O_2 sensing as they are sensitive to H_2O_2 oxidation and they have relatively high Raman cross-section. Mercaptophenylboronic acid (3-MPBA and 4-MPBA)[42,43] and others[44] based on nanosphere [42,44], core-satellite[43] and core-shell[22] nanoparticles were reported for H_2O_2 SERS sensing. However, we studied the pH effects on the oxidation reaction of boronate molecules by H_2O_2, and found that pH affected the readout, which will be discussed deeply in Chapter 3. Yet none of those reported SESR based methods sensing H_2O_2 based on boronate molecules took this into consideration, as the best of our knowledge. Further, with the Raman probes carried in the outer side of nanostructure, biomolecules will be absorbed on the modified surface, resulting the replacement of Raman probes or interfered signals, when nanostructures are suspended in biological media[45]. And uncontrollable agglomeration or aggregation may happen with

unprotected nanostructures and strong heterogeneous SERS responses will aslo affect the readout.

Thus we designed and synthesized one protected gold-silica nanocapsule with Raman probes functionalized inside the cavity. This nanostructure performed its stability in intracellular H_2O_2 sensing. Moreover, we also modified Raman probe for pH determination onto our nanostructure to realize multiplexing pH and H_2O_2 sensing, ensuring the accurate readout for H_2O_2 and offering more information about cellular environment. For instance, pH and H_2O_2 level are both reported to be abnormal when Alzheimer's disease occurs [46,47,48,49]. This multiplex nanosensor has the potential applications for diseases monitoring.

1.5 References

1. Smith, E. & Dent, G. Modern Raman spectroscopy-a practical approach. Wiley: Chichester, U.K., (2005).
2. Hahn, D. W. Raman Scattering Theory. (2007). Available from: http://plaza.ufl.edu/dwhahn/Raman%20Scattering%20Theory.pdf
3. Kim, H. H. Endoscopic Raman Spectroscopy for Molecular Fingerprinting of Gastric Cancer: Principle to Implementation. *Biomed Res. Int.* **2015**, (2015).

4. Almond, L. M. *et al.* Raman spectroscopy: A potential tool for early objective diagnosis of neoplasia in the oesophagus. *J. Biophotonics* **4**, 685–695 (2011).

5. Sur, U. K. Surface-Enhanced Raman Spectroscopy. *Resonance* 154–164 (2010).

6. Schatz, G. C. Electrodynamics of nonspherical noble metal nanoparticles and nanoparticle aggregates. *J. Mol. Struct.* **573**, 73–80 (2001).

7. Haynes, C.L., McFarland, A.D. & Van Duyne, R.P. Surface-enhanced Raman spectroscopy. *Anal. Chem.* **77**, 338A-346A (2005).

8. Ruchita, S. D. & Agrawal, Y. K. Raman spectroscopy: Recent advancements, techniques and applications. *Vib. Spectrosc.* **57**, 163–176 (2011).

9. Kelly, K. L., Coronado, E., Zhao, L. & Schatz, G. C. The Optical Properties of Metal Nanoparticles: The Influence of Size, Shape, and Dielectric Environment. *J. Phys. Chem. B* **107**, 668–677 (2003).

10. Maher R. C. SERS Hot Spots. In: Kumar C.S.S.R. (eds) Raman Spectroscopy for Nanomaterials Characterization. Springer, Berlin, Heidelberg. https://doi.org/10.1007/978-3-642-20620-7_10. (2012).

11. Moskovits, M. Surface-enhanced spectroscopy. *Rev. Mod. Phys.* **57**, 783–826 (1985).

12. Jensen, L., Aikens, C. M. & Schatz, G. C. Electronic structure methods for studying surface-enhanced Raman scattering. *Chem. Soc. Rev.* **37**, 1061–1073 (2008).

13. Etchegoin, P. G. & Le Ru, E. C. A perspective on single molecule SERS: Current status and future challenges. *Phys. Chem. Chem. Phys.* **10**, 6079–6089 (2008).

14. Zhang, W., Cui, X. & Martin, O. J. F. Local field enhancement of an infinite conical metal tip illuminated by a focused beam. *J. Raman Spectrosc.* **40**, 1338–1342 (2009).

15. Zhao, L. L., Jensen, L. & Schatz, G. C. Surface-enhanced raman scattering of pyrazine at the junction between two Ag 20 nanoclusters. *Nano Lett.* **6**, 1229–1234 (2006).

16. Anderson, D. J. & Moskovits, M. A SERS-active system based on silver nanoparticles tethered to a deposited silver film. *J. Phys. Chem. B* **110**, 13722–13727 (2006).

17. Sharma, B., Frontiera, R. R., Henry, A.-I., Ringe, E. & Van Duyne, R. P. SERS: Materials, applications, and the future. *Mater. Today* **15**, 16–25 (2012).

18. Alvarez-Puebla, R. A. & Liz-Marzán, L. M. SERS-based diagnosis and biodetection. *Small* **6**, 604–610 (2010).

19. Chan, J., Fore, S., Wachsmann-Hogiu, S. & Huser, T. Raman spectroscopy and microscopy of individual cells and cellular components. *Laser Photonics Rev.* **2**, 325–349 (2008).

20. Kang, T. *et al.* Ultra-specific zeptomole MicroRNA detection by plasmonic nanowire interstice sensor with Bi-temperature hybridization. *Small* **10**, 4200–4206 (2014).

21. Si, Y. *et al.* Alkyne-DNA-Functionalized Alloyed Au/Ag Nanospheres for Ratiometric Surface-Enhanced Raman Scattering Imaging Assay of Endonuclease Activity in Live Cells. *Anal. Chem.* **90**, 3898–3905 (2018).

22. Zhang, C., Liu, X., Xu, Z. & Liu, D. Multichannel Stimulus-Responsive Nanoprobes for H_2O_2 Sensing in Diverse Biological Milieus. *Anal. Chem.* **92**, 12639–12646 (2020).

23. Hwang, J., Lee, S. & Choo, J. Application of a SERS-based lateral flow immunoassay strip for the rapid and sensitive detection of staphylococcal enterotoxin B. *Nanoscale* **8**, 11418–11425 (2016).

24. Rodriguez-Lorenzo, L., Fabris, L. & Alvarez-Puebla, R. A. Multiplex optical sensing with surface-enhanced Raman scattering: A critical review. *Anal. Chim. Acta* **745**, 10–23 (2012).

25. Laing, S., Gracie, K. & Faulds, K. Multiplex *in vitro* detection using SERS. *Chem. Soc. Rev.* **45**, 1901–1918 (2016).

26. Faulds, K., Barbagallo, R. P., Keer, J. T., Smith, W. E. & Graham, D. SERRS as a more sensitive technique for the detection of labelled oligonucleotides compared to fluorescence. *Analyst* **129**, 567–568 (2004).

27. Wang, Y., Xu, H., Zhang, J. & Li, G. Electrochemical sensors for clinic analysis. *Sensors* **8**, 2043–2081 (2008).

28. Guarrotxena, N. & Bazan, G. C. Antibody-functionalized SERS tags with improved sensitivity. *Chem. Commun.* **47**, 8784–8786 (2011).

29. Roy, S., Soh, J. H. & Ying, J. Y. A microarray platform for detecting disease-specific circulating miRNA in human serum. *Biosens. Bioelectron.* **75**, 238–246 (2016).

30. Bartlett, J. S., Voss, K. J., Sathyendranath, S. & Vodacek, A. Raman scattering by pure water and seawater. *Appl. Opt.* **37**, 3324 (1998).

31. Lin, D. *et al.* Geometrically encoded SERS nanobarcodes for the logical detection of nasopharyngeal carcinoma-related progression biomarkers. *Nat. Commun.* **12**, 1–16 (2021).

32. Wu, J. *et al.* Ultrasensitive and Simultaneous SERS Detection of Multiplex MicroRNA Using Fractal Gold Nanotags for Early Diagnosis and Prognosis of Hepatocellular Carcinoma. *Anal. Chem.* **93**, 8799–8809 (2021).

33. Zhang, D. *et al.* Quantitative and ultrasensitive detection of multiplex cardiac biomarkers in lateral flow assay with core-shell SERS nanotags. *Biosens. Bioelectron.* **106**, 204–211 (2018).

34. Alfadda, A. A. & Sallam, R. M. Reactive oxygen species in health and disease. *J. Biomed. Biotechnol.* **2012**, (2012). DOI: 10.1155/2012/936486.

35. Dumont, M. & Beal, M. F. Neuroprotective strategies involving ROS in Alzheimer disease. *Free Radic. Biol. Med.* **51**, 1014–1026 (2011).

36. Rezende, F., Brandes, R. P. & Schröder, K. Detection of hydrogen peroxide with fluorescent dyes. *Antioxidants Redox Signal.* **29**, 585–602 (2018).

37. Marinho, H. S., Real, C., Cyrne, L., Soares, H. & Antunes, F. Hydrogen peroxide sensing, signaling and regulation of transcription factors. *Redox Biol.* **2**, 535–562 (2014).

38. Brewer, T. F., Garcia, F. J., Onak, C. S., Carroll, K. S. & Chang, C. J. Chemical approaches to discovery and study of sources and targets of hydrogen peroxide redox signaling through NADPH oxidase proteins. *Annu. Rev. Biochem.* **84**, 765–790 (2015).

39. Sies, H. Hydrogen peroxide as a central redox signaling molecule in physiological oxidative stress: Oxidative eustress. *Redox Biol.* **11**, 613–619 (2017).

40. Belousov, V. V. *et al.* Genetically encoded fluorescent indicator for intracellular hydrogen peroxide. *Nat. Methods* **3**, 281–286 (2006).

41. Gutscher, M. *et al.* Proximity-based protein thiol oxidation by H_2O_2-scavenging peroxidases. *J. Biol. Chem.* **284**, 31532–31540 (2009).

42. Gu, X., Wang, H., Schultz, Z. D. & Camden, J. P. Sensing Glucose in Urine and Serum and Hydrogen Peroxide in Living Cells by Use of a Novel Boronate Nanoprobe Based on Surface-Enhanced Raman Spectroscopy. *Anal. Chem.* **88**, 7191-7197 (2016).

43. Li, Q. *et al.* Dual Ratiometric SERS and Photoacoustic Core–Satellite Nanoprobe for Quantitatively Visualizing Hydrogen Peroxide in Inflammation and Cancer. *Angew. Chemie - Int. Ed.* **60**, 7323–7332 (2021).

44. Li, X., Duan, X., L., Yang, P. Li, L. & Tang, B. Accurate *in situ* monitoring of mitochondrial H_2O_2 by robust SERS nanoprobes with a Au−Se interface. *Anal. Chem.* **93**, 4059–4065 (2021).

45. Hu, B. *et al.* Avoiding Thiol Compound Interference: A Nanoplatform Based on High-Fidelity Au-Se Bonds for Biological Applications. *Angew. Chemie* **130**, 5404–5407 (2018).

46. Halliwell, B. Oxidants and the central nervous system: some fundamental questions. Is oxidant damage relevant to Parkinson's disease, Alzheimer's disease, traumatic injury or stroke? *Acta Neurol. Scand.* **80**, 23–33 (1989).

47. Zhang, L., Zhao, B., Yew, D. T., Kusiak, J. W. & Roth, G. S. Processing of Alzheimer's amyloid precursor protein during H_2O_2-induced apoptosis in human neuronal cells. *Biochem. Biophys. Res. Commun.* **235**, 845–848 (1997).

48. Harguindey, S., Reshkin, S., Orive, G., Luis Arranz, J. & Anitua, E. Growth and Trophic Factors, pH and the Na+/H+ Exchanger in Alzheimers Disease, Other Neurodegenerative Diseases and Cancer: New Therapeutic Possibilities and Potential Dangers. *Curr. Alzheimer Res.* **4**, 53–65 (2007).

49. Lyros, E. *et al.* Normal brain aging and Alzheimer's disease are associated with lower cerebral pH: an *in vivo* histidine 1H-MR spectroscopy study. *Neurobiol. Aging* **87**, 60–69 (2020).

2. Synthesis and applications of SERS encoded silver silica nanocomposites

2.1 ABSTRACT

Early and precise healthcare diagnosis is critically important for preventing an outbreak of a pandemic disease. Biosensors, especially the ones based on surface-enhanced Raman scattering (SERS) have made their contribution in biodiagnosis. The most critical feature which hampers SERS bioapplications is to build up homogenous, sensitive and reproducible SERS platforms. Here we reported one nanostructure which confined silver nanoagglomerates inside silica coating. We studied the fundamental aspects including pH and solvent for the conformation of silver thiol bond. We found that solvent had little effect on the modification and stability of this covalent bond, while pH was critical for an optimized conformation of silver thiol bond. With controlled agglomeration, we increased the percentage of hot spots, which exhibited high Raman enhancement. And with the biofunctionalization with antibody onto the protecting silica layer, we managed to perform SERS-based ELISA SARS-CoV-2 spike protein detection. We offered herein one nanostructure with robust and homogeneous SERS signal which can be potentially applied for biodiagnosis.

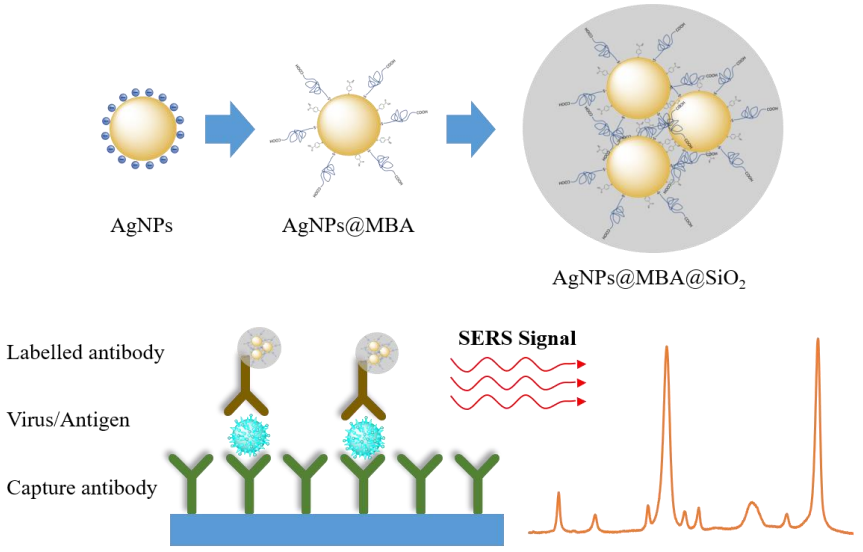

2.2 INTRODUCTION

The design for precise diagnosis is critical to human health as for preventing pandemics or other biothreads. Nanosystems have been widely developed in sensor devices for diagnostics, *in vitro* and *in vivo* diagnosis[1]. This diagnosis field definitely takes benefits from the design and synthesis of nanomaterials, especially noble metal nanomaterials showing localized surface plasmon resonance (LSPR) properties. LSPR originates from the interaction of metallic nanomaterials with electromagnetic irradiation. This LSPR phenomenon limits nanomaterials absorbing specific region of light, and makes the nanomaterials sensitive to the modifications of physical properties of nanomaterials and their environments showing plasmonic absorption shifts[2]. Based on their optical properties, flexible functionalized nanomaterials have already been

applied in sensing varieties of biomolecules, including biomarkers for cancer[3], enzyme[4], DNA[5], and other biological species[6].

Surface-enhanced Raman spectroscopy (SERS) also depends on plasmonic platforms. SERS signals can be collected from the molecules which are in close proximity of nanometallic surfaces with confined LSPR[7]. In general, average enhancement factors for typical SERS substrates are amplified by 10^6 to 10^8 orders of magnitude comparing with their Raman signature[8] which is explained with two enhancement mechanisms: the electromagnetic and the chemical or charge transfer mechanisms. Moreover, this enhancement can be further increased up to 10^{15} orders of magnitude to SERS signal by hot spots[9]. Hot spots are highly localized regions of intense local field enhancement caused by the plasmonic coupling of the particles when they are very close to each other[8]. Thus, hot spots have critical importance when designing a SERS nanostructure. Gold and silver are the most commonly applied materials for SERS substrates, as they offer high field enhancement in the visible to near infrared range due to their high density of electrons[10]. SERS as a nondestructive technology provides chemical information in aqueous environments. Thus SERS has been an effective tool to realize qualitative and quantitative detection of biological species, including micro RNA analysis[11], enzyme[12], hydrogen peroxide[13] and staphylococcal enterotoxin B[14] with gold nanowire, gold-silver alloy NPs and gold-MnO_2 core-shell, hollow gold nanospheres separately. However, producing homogenous, sensitive and reproducible SERS platform

is the main difficulty which hampers SERS bioapplications[15]. Thus, the design and controllable synthesis of nanostructures is critical.

Here we present a controllable design and synthesis of one nanostructure which confined encoded silver nano-agglomerates inside silica coating. We systematically studied the fundamental aspects and optimized the thiol silver bonding for encoding silver nanoparticles. With the help of controlled agglomeration, we improved the percentage of hot spots which guaranteed the extremely high Raman enhancement. These encoded agglomerates were further encapsulated with silica which could protect these agglomerates from oxidation, contaminations and increase the stability for a long period of time. With further biofunctionalization with antibody, we also demonstrated the performance of our devices for SARS-CoV-2 spike protein detection. The reference diagnosis for SARS-CoV-2 is based on reverse transcription polymerase chain reaction (RT-PCR)[16]. Yet there are false positive or negative reports, especially for the early stages. Biosensors as alternative or supplementary solutions have been developed based on plasmonic nanomaterials. Gold nanoparticles have been developed for colorimetric detection of SARS-CoV-2 with isolated RNA samples[17] and for IgM Antibodies against the SARS-CoV‑2 Virus detection based on a lateral flow device[18]. A more sophisticated device based on gold nanoislands was reported for SARS-CoV-2 detection targeting selected sequences[19]. Compared with the biosensors mentioned, we selected the detection of SARS-CoV-2 with spike protein, which are the major immnodominant protein[20]. One of the promising advantage is our biosensor can be potentially

applied for screening SARS-CoV-2 without prior sample treatment. This whole designed procedure promised our nanostructure high Raman enhancement and robust intensity for sensitive sensing, and uniform synthesis for stability and repeatability. We offered one nanostructure which can be reliably applied in biosensing.

2.3 EXPERIMENTAL SECTION

2.3.1 Materials and Reagents

Ammonia solution, Tetraethyl orthosilicate, Silver nitrate ($AgNO_3$), Gold (III) chloride hydrate, Magnesium sulfate ($MgSO_4$), Ascorbic acid, 4-Mercaptobenzoic acid, Sodium hydroxide, carboxy-PEG12-thiol (CTPEG12), Ethanol, (3-Glycidyloxypropyl) trimethoxysilane (GPTMS), Ammonium Sulfate, Bovine Serum Albumin, HBSS, PBS, EIA/RIA 96 well plate, hydrogen peroxide (H_2O_2, 50wt.% in water), hydrochloric acid (HCl), nitric acid (HNO_3), were purchased from Merck. tri-Sodium Citrate 2-Hydrate (Na_3Cit) was purchased from PanReac Applichem. SARS-CoV/SARS-CoV-2 Spike antibody, Chimeric Mab (Cat: 40150-D001 and Cat: 40150-D003) and SARS-CoV Spike/RBD Protein (Cat: 40150-V08B2) were purchased from Sino Biological. Alexa Fluor® 488 AffiniPure Goat Anti-Mouse IgG (H+L) was purchased from JacksonImmuno. All the chemicals were used without further purification.

2.3.2 Silver and gold nanoparticles synthesis

$AgNO_3$ 0.1 M, $MgSO_4$ 0.1 M, Na_3Cit 0.1 M and Ascorbic acid 0.1 M were prepared in aqueous solution. Solutions were prepared and

used freshly. To avoid contamination, the glassware and magnets used were cleaned with Aqua Regia, basic piranha (RCA) before synthetizing silver nanoparticles (AgNPs) and gold nanoparticles (AuNPs).

For synthesizing AgNPs, two solutions were prepared separately. Solution 1 is prepared by mixing 5.115 mL 0.1 M Na_3Cit solution with 375 µL 0.1 M Ascorbic acid solution and solution 2 is prepared by mixing 839 µL 0.1 M $MgSO_4$ solution and 1.116 µL 0.1 M $AgNO_3$ solution. Two solutions were prepared at the same time when 250 mL Milli Q water was already boiled in an Erlenmeyer flask under homogeneous and strong stirring. Solution 1 was first added in one shot into this boiling aqueous solution after prepared for 4min. Then solution 2 was added in one shot after one more minute. The mixture was kept stirring at 300 ºC for 30 minutes. Then the solution was cooled down at room temperature without stirring. The nanoparticles (NPs) were protected from the light and stored at 4 ºC.

For synthesizing AuNPs, 250 mL Milli-Q water was heated in an Erlenmeyer flask at 300 ºC under homogeneous and strong stirring. Once water started boiling, 678 µL 0.1 M Na_3Cit added after water boiled. 2 min later, 623.7 µL 0.1 M $HAuCl_4$ added in one shot. Reaction was kept at 300 ºC for 30 min under stirring. Then the NPs was kept undisturbed and cooled down to room temperature, and further stored at 4 ºC and protected from the light.

2.3.3 Modification and controllable agglomeration of AgNPs and AuNPs

The modification and controllable agglomeration procedure applied for both AgNPs and AuNPs.

AgNPs or AuNPs synthesized were firstly cleaned by centrifugation 5400 rpm (2500 g) 20 min and adjusted to approx. $2.9x10^{10}$ NPs/mL with Milli-Q water calculated by UV-vis extinction. Raman probe MBA and stabilizer CTPEG12 were prepared in ethanolic solution with 10^{-3} M concentration and stored in 4 ºC. CTPEG12 and MBA amounts were calculated based on the metallic surface of the NPs which would be used for modification. 1 molecule/nm^2 of the CTPEG12 and 3 molecules/nm^2 of MBA added to certain volume of ethanol under vigorous stirring. Equal volume of cleaned NPs ($2.9x10^{10}$ NPs/mL) aqueous solution were added to this alcoholic solution under strong stirring after 5 min of the MBA and CTPEG12 addition. Then fresh prepared NaOH solution with final concentration 1.15 mM was added to NPs mixture. Reaction was kept under stirring for 24 h to finish modification.

MBA modified AgNPs and AuNPs were agglomerated in a controlled manner by two centrifugation steps. First centrifugation at 4800 rpm (2000 g) 20min and a second centrifugation at 2000 rpm (350 g) 15min. NPs were redispersed with Milli-Q water.

The SERS spectra of MBA modified AgNPs agglomeration (AgNPs@MBA) were collected with a Renishaw's inVia Qontor Raman system equipped with a Leica confocal microscope. The spectrograph used a high-resolution grating (1200 l cm^{-1}), band-pass filter optics, a NIR laser (785 nm) and a Peltier cooled CCD array detector, equipped with Windows-based Raman Environment

(Wire™) software. $4.55X10^{10}$ NPs/mL (calculated by UV-vis extinction) 200 µl of AgNPs@MBA solution was added into 96 well plate for SERS spectra acquisition. The laser was focused into the samples with an 5X objective (NA 0.12), providing a laser spot diameter of approximate 8 µm. The spectra were collected with 1s exposure time and 100 mW laser power at the samples.

2.3.4 SiO_2 encapsulation

Silica encapsulation was conducted in the same way for agglomerated and non-agglomerated MBA modified AgNPs and agglomerated and non-agglomerated MBA modified AuNPs.

304.7 µl of NH_4OH (35%) were added into 15 mL of EtOH and mixed properly, followed by adding 2.3 mL (approx. $7x10^{10}$ NPs/mL) of modified NPs in aqueous solution, and mixing the whole system properly. 12.4 µl of TEOS 10% v/v diluted by ethanol were added consecutively into this mixture, and mixing the solution by stirring for 30 seconds. Then leave the reaction system undisturbed for approx. 12 h. Silica coated modified NPs were cleaned by centrifugation thrice (6000 rpm, 20min). Samples were stored at 4 ºC and protected from light.

The morphology of silica encapsulated MBA modified AgNPs and AuNPs agglomerations (AgNPs@MBA@SiO_2 and AuNPs@MBA@SiO_2) were checked with transmission electron microscopy (TEM), using a JEOL JEM 1010 TEM operating at an acceleration voltage of 80 kV with a tungsten filament. For the preparation of TEM samples, 10 µL of AgNPs@MBA@SiO_2 or AuNPs@MBA@SiO_2 ethanolic solution were drooped on a TEM

grid. TEM samples were completely dry at room temperature before starting TEM analysis. The morphology was checked and the average size and polydispersity was calculated with at least 100 particles by using image process software “Image J”.

Dynamic light scattering (DLS) and zeta potential measurements were performed with Malvern Zetasizer Nano ZS. Aqueous samples were transferred into disposable polystyrene cuvette for size measurements and disposable folded capillary cells for zeta potential measurements. Each sample was measured 3 repeats.

The extinction spectrum of each synthetic intermediate was recorded with Ultrospec™ 2100 pro UV-Visible spectrophotometer. 600 µL diluted aqueous samples were added into a Quartz cuvette (104-002-10-40, Hellma), and the extinction spectra between 250 and 900 nm wavelength were collected with Milli-Q water as a reference.

2.3.5 AgNPs@MBA@SiO_2 deposited materials preparation

20 µl $7x10^{10}$ NPs/mL of AgNPs@MBA@SiO_2 were dropped on different materials and the composition was left to dry at room temperature. The materials used here are listed as following: semi-aniline leather, aniline leather, pigmented leather, polyester, silk, plastic (PVC), glass, brass, cotton, pigmented leather.

SERS characterization of all samples prepared here were conducted using Renishaw inVia Qontor Raman. 20X Leica objective was used with integration time 0.1 s and a power at the sample of 3 mW.

The surface of AgNPs@MBA@SiO_2 deposited materials were analyzed with a scanning electron microscope (SEM) from Phenom XL Desktop SEM with a Backscattered electron detector. The elemental analysis was conducted by energy-dispersive X-ray spectroscopy equipped with the SEM.

2.3.6 Antibody immobilization on AgNPs@MBA@SiO_2

Encoded AgNPs@MBA@SiO2 were primed with commonly used silane coupling agent GPTMS by mixing 1mL $4.5x10^{10}$ NPs/mL AgNPs@MBA@SiO_2 ethanolic solution with 105 µl 0.01% v/v GPTMS ethanolic solution under stirring at 60 °C for 12 h. This amount of GPTMS was calculated to provide approx. GPTMS 20 molecules/nm^2 of AgNPs@MBA@SiO_2 surface. Then GPTMS modified AgNPs@MBA@SiO_2 (AgNPs@MBA@SiO_2@GPTMS) was cleaned by centrifugation at 4000 rpm 8min with ethanol and phosphate buffered saline (PBS).

This 1mL AgNPs@MBA@SiO_2@GPTMS was further diluted with PBS into 2.5 mL before biofunctionalization with SARS-CoV/SARS-CoV-2 Spike antibody (Anti-COV spike Ab, Cat: 40150-D003, MW 150 kDa). Then 2.5 mL of 2 M freshly prepared Ammonium sulphate solution in PBS and 25 µg Anti-COV spike Ab were added into AgNPs@MBA@SiO_2@GPTMS solution and reaction was kept for 24h on a rocker table with 110 rpm in a 37℃ room. When immobilization was concluded, final concentration of 0.1% bovine serum albumin (BSA) solution in PBS was added to avoid the adhesion of the NPs to the centrifuge tubes during

centrifugation. The Anti-COV spike Ab functionalized AgNPs@MBA@SiO_2@GPTMS (AgNPs@MBA@SiO_2@Ab) were cleaned by centrifugation at 4000 rpm 8min with 0.1% BSA PBS solution three times to eliminate any unbound antibody. AgNPs@MBA@SiO_2@Ab was resuspended into 0.1% BSA PBS solution to further stabilize the NPs in the saline environment with approx. concentration $9x10^9$ NPs/mL.

This successful immobilization was confirmed with confocal laser scanning microscope (CLSM) (Leica SP2 (inverted)). 10 µL $9x10^9$ NPs/mL AgNPs@MBA@SiO_2@Ab mixed with 15µL PBS and 25 µL secondary antibody (5µg/mL, Alexa Fluor® 488 AffiniPure Goat Anti-Mouse IgG) for 1 h at room temperature. One negative control was conducted with AgNPs@MBA@SiO_2 following exactly the same method used for AgNPs@MBA@SiO_2@Ab.

2.3.7 SERS based Elisa biosensing

Coating ELISA plates with capture Ab: Thawed and mixed by gently vortexing SARS-CoV/SARS-CoV-2 Spike antibody vials (capture Ab, Cat: 40150-D001, MW 150 kDa) before diluting in PBS. 96-well microtiter ELISA plates were coated with 50 µl of 6 µg/mL capture Ab per well. To avoid bubbles and ensure homogenous coating on the bottom of every well, lightly taped the plate against hard surface. Elisa plates were sealed with parafilm and aluminium foil to protect from the light and incubated at 4°C overnight.

Blocking ELISA plates: Coated ELISA plates were washed 3 times with PBS containing 0.1% Tween 20 (PBS-T) solution by adding

300 μL PBS-T solution for each wash. To remove residual buffer, plates were blotted forcefully on a paper towel after each wash. Blocking solution was prepared by mixing BSA into PBS-T solution with concentration of 1%. 200 μl blocking solution was added into each well of the plates and incubated in a 37°C hot room for one hour. After the blocking incubation, throwed off the blocking solution and tapped the plates dry on a paper towel to remove residuals.

Spike protein assay: Spike protein (SARS-CoV Spike/RBD Protein, MW 26.5 kDa) were diluted with PBS into a series concentration: 0.01, 0.02, 0.1, 0.2, 0.4, 0.6, 0.8, 1, 1.2, 1.6 ng/μL. 50 μl of diluted spike protein (and PBS used as negative control) were transferred into wells in the ELISA plate. Plates were placed in a 37 ℃ hot room for 1h, followed by washing with PBS thrice. Then 50 μl $9x10^9$ NPs/mL AgNPs@MBA@SiO_2@Ab solution was added to each working well of the plate. Be sure to avoid touching the walls in order to avoid high background. Plates were incubated in a 37 ℃ hot room for 1h, then washed with PBS thrice. Plates were analyzed with Raman by checking SERS signal of labelled AgNPs@MBA@SiO_2@Ab. 5X Leica objective with integration time 1 s and a power at the sample of 50 mW was used for SERS spectra acquisition. SERS spectra were collected and intensity at 1075 cm^{-1} were calculated by averaging with 8 spectra from 8 random places in Elisa wells.

2.4 RESULTS AND DISCUSSION

2.4.1 AgNPs@MBA@SiO_2 synthesis and characterization

We have synthesized a SERS encoded core-shell nanostructure comprising silver NPs agglomerates. In briefly, a SERS probe MBA and a polymeric stabilizer CTPEG12 controlled co-absorption and covalent binding formation on the metallic surfaces of the AgNPs was conducted, followed by a controlled agglomeration step by centrifugation. Then these agglomerates were encapsulated and protected with a homogenous layer of silica.

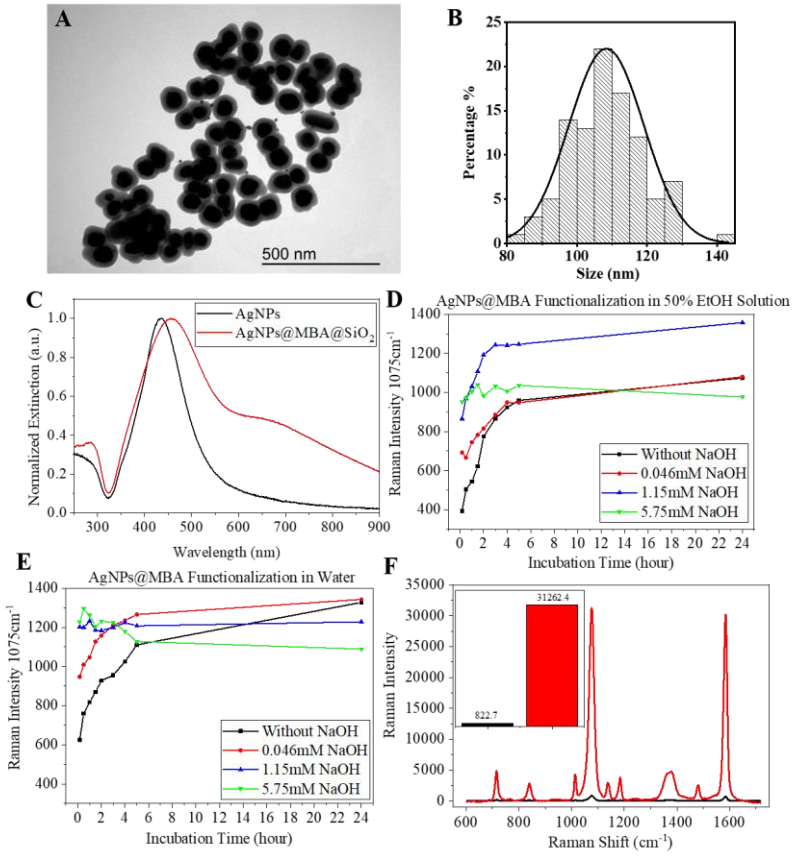

Figure 1: Synthesis and characterization of AgNPs@MBA@SiO_2. (A) TEM image of AgNPs@MBA@SiO_2. (B) size distribution of AgNPs@MBA@SiO_2

based on 100 nanoparticles from TEM images analyzed with ¨ Image J ¨. (C) UV-Visible extinction spectra of AgNPs (in black) and AgNPs@MBA@SiO_2 (in red). (D&E) Kinetic results calculated by SERS intensity at 1075 cm^{-1} of AgNPs@MBA with different amount of NaOH in 50% EtOH/water solution (D) and in aqueous solution (E). Black line: without NaOH; Red line: with 0.046 mM NaOH; Blue line: with 1.15 mM NaOH; Green line: with 5.75 mM NaOH. (F) SERS spectra and SERS intensity at 1075 cm^{-1} (inset image) of non-agglomerated AgNPs@MBA@SiO_2 (in black), and AgNPs@MBA@SiO_2 (in red).

Figure 1A showed the TEM image of AgNPs@MBA@SiO_2, which clearly demonstrated that each agglomerate was encapsulated with silica coating. The AgNPs core was spherical and the anisotropy aspect ratio was close to 1. There were around 1% of the particles non-spherical, *i.e.*, rod-shaped particles or quasi-flat triangles calculated with approx. 100 particles. Based on more than 100 AgNPs@MBA@SiO_2 from TEM images, we calculated the size of AgNPs@MBA@SiO_2 having each particle 4 different angles for measurement. The core of AgNPs was approx. 60-70 nm and the SiO_2 layer was estimated around 20 nm. The complete size of AgNPs@MBA@SiO_2 was around 110 nm as shown in Figure 1B. We could also estimate that there were more than 60% of the agglomerates in form of isolated dimers, trimers, tetramers, pentamers, hexamers, or mixtures thereof. Figure SI-1 showed the hydrodynamic diameter of AgNPs@MBA@SiO_2 was 133.8 nm with PDI 0.130 and the zeta potential average was -24.7 mV. This hydrodynamic size agreed to the average size we measured with TEM. And the negative surface charge agreed with silica property. The size, concentration and agglomeration of the NPs can also be measured by UV-Vis spectrum[21]. Figure 1C showed the normalized extinction spectra of the citrate capped AgNPs obtained and

AgNPs@MBA@SiO_2. The characteristic localized-surface plasmon resonances (LSPRs) of silver spherical nanoparticles was shown in the UV-Vis spectra of AgNPs which centered in the UV spectral range around 430 nm. As for AgNPs@MBA@SiO_2, the new prominent of a shoulder absorption at around 700 nm, and the red-shift and broadening of this characteristic LSPRs to higher wavelengths indicated the significant formation of agglomerates.

For AgNPs synthesis, the bottom up synthesis relying on the chemical reduction of metal salts was performed, with shape and size control, by citrate reduction of $AgNO_3$ that are well known[22].

Aromatic compounds are commonly used as Raman probes as they have high Raman cross section. Previous reported articles used ethanol as solvent during Raman probe modification based on the consideration of low solubility of hydrophobic Raman probes[23]. While to the best of our knowledge, there is still lack of detailed information on the fundamental factors affecting Raman probes modification. The formation of thiol-silver bond as a function of pH and solvent has been studied here. The SERS probe used here is an aromatic molecule MBA which has high Raman cross section[24] and the polymeric stabilizer CTPEG12 is an aliphatic chain polymer with 12 carbon atoms and a carboxylic group at the end of the chain. Both MBA and CTPEG12 were bonded to AgNPs through their thiol group by forming covalent bonds.

SERS characterization of AgNPs@MBA were conducted to study the pH and solvent effect on MBA modification. The complete SERS spectra and zoomed spectra showing characteristic peak at

1075 cm^{-1} of AgNPs@MBA in 50% EtOH/water solution were shown in Figure SI-2 and in aqueous solution were shown in Figure SI-3, from 10 min to 24 h after the modification start point, with different amount of NaOH addition resulting in different reaction pHs. Figure 1D and 1E showed the absorption and bonding kinetic results of AgNPs@MBA under different codification conditions, including aqueous system and 50% ethanol/water system with different amount of NaOH, represented by the SERS intensity of the characteristic ring breathing band of adsorbed MBA at 1075 cm^{-1} over the time[25].

Because of the physical property differences (*e.g.,* pKa and dielectric constant) between water and ethanol, the pH will be different even with the same amount of NaOH addition[26]. Table SI-1 showed the values we got from pH test strips in aqueous system and in 50% ethanol/water system.

When comparing the first 10 min after the addition of Raman code, in both 50% ethanol/water solution and aqueous solution, the intensity at 1075 cm^{-1} increased along with the system pH as shown in Figure 1D and 1E. The time needed for codification reaching their plateau intensity also varied with the pH of systems, *i.e.*, shorter time needed for more alkaline systems. The absorption of thiol onto silver mental surface follows physisorption to chemisorption where breaks the S-H bond and forms silver thiol covalent bond[27]. Environmental pH will affect the deprotonation of thiol group, thus the formation speed of silver thiol bond. As we observed in our system, an alkaline environment facilitated the codification of MBA onto silver metallic surface.

When comparing the plateau intensity after 24 h, the number of MBA absorbed were similar when MBA codification was performed in 50% ethanol/water solution with 1.15mM NaOH (pH 8) and in aqueous solution with 0.046 mM NaOH (pH 8.5), which reached the maximum intensity among all the conditions. When continually increasing pH, the amount of codified MBA started to decrease in both 50% ethanol/water solution and aqueous solution. Considering the pKa of MBA and CTPEG12 were around 4 to 5[28], the deprotonated MBA and CTPEG12 were both negatively charged. This electrostatic repulsion on the surface and the competition between MAB and CTPEG12 will hamper MBA bonding from the balk solution, since in general, compared with aromatic thiols, aliphatic thiols have better electrochemical and thermodynamic stability[29]. Dissociation was also favored at higher pH[30] may also related with this dynamic equilibrium.

Ethanol has little effect on the modification and stability of metal-thiol bond. Although it was demonstrated that because of the reduction effect of ethanol on gold, the strength of metal-thiol contacts can be weakened[31]. When hydrophobic Raman probes were used, ethanol was still encouraged to use.

The packing of the monolayer and the number of the MBA molecules absorbed on the metallic surface were the results of aspects, as we discussed here, including the metal-thiol bonding formation speed which is affected by pH, the electrostatic repulsion on the metallic surface, and the competition between Raman probe and stabilizer. To achieve optimized modification of thiolated aromatic compound onto metallic surfaces, the controlling of

reaction pH is critical.

UV-vis characterization of AgNPs and AgNPs@MBA in all codification conditions after 24 h of the addition of the Raman code were performed and shown in Figure SI-4. No evidence of agglomeration events in our colloidal system monitored by UV-Vis spectroscopy, comparing the spectra of AgNPs and AgNPs@MBA under all codification conditions, with the appearance of LSPRs at around 435 nm associated to isolated AgNPs, and the absence of absorption feature in the NIR range (approx. 650 nm) which attributed to plasmonic contribution of interacting particles (*i.e.*, agglomeration). Further, compared with the plamonic absorption of AgNPs, AgNPs@MBA suffered a red shift around 12 nm indicating MBA was properly absorbed and bonded onto the metallic surface. This conclusion went well for all the codification conditions we used, thus no agglomeration happened under all circumstances, supporting the different performance we got based on the kinetic results were caused by the final packing quality which was affected by the reaction pH and system solvent.

With controlled agglomeration of AgNPs@MBA by following different centrifugation steps under certain pH conditions, we managed to increase the SERS efficiency up to nearly 40 times when comparing the SERS spectra of AgNPs@MBA@SiO_2 and non-agglomerated AgNPs@MBA@SiO_2 and their characteristic peak intensity at 1075 cm^{-1}, as shown in Figure 1-F. This high SERS response was contributed by the active SERS structures called “hot spots”, which are highly localized regions of intense local field enhancement caused by the plasmonic coupling of the

particles when they are very close to each other[8]. In comparation with aggregation or uncontrolled agglomeration, where the particles merged thus without hot spots[23], controlled agglomeration offered a useful tool for Raman detection.

Silica coating was performed by a modified Stöber method[32]. A carboxylic group at the end of the chain of the polymer modified on the metallic surface would help the proper growth of silica oxide. The SiO_2 layer protects the silver agglomerates from oxidation, contaminations and promises the SERS signal stability for a long period of time, thanks to the unique properties of the SiO_2 layer (*e.g.*, surface chemistry, biocompatibility, optical transparency, and colloidal stability).

Our optimized protocol for synthesizing a SERS encoded core-shell nanostructure can be further applied to gold nanomaterials to broaden the application field. AuNPs are synthesized following the method reported so-called sodium citrate method[33]. Then the modification with MBA and CTPEG12, the controlled agglomeration and the SiO_2 encapsulation were following the same protocol as for AgNPs as described in experimental section. Figure SI-5A showed the TEM image of AuNPs@MBA@SiO_2. The AuNPs were spherical and more than 60% of the particles were agglomerated based on 100 particles from TEM images. Figure SI-5B represents the size histogram of AuNPs@MBA@SiO_2 and the average diameter around 107 nm was obtained by measuring 4 different angles of 100 nanostructures, with all populations (isolated NPs, dimers, trimers, tetramers, pentamers, and hexamers) included. Figure SI-5C showed the hydrodynamic diameter of

AgNPs@MBA@SiO_2 was 113.6 nm with PDI 0.199 and the zeta potential average -27.9 mV was shown in Figure SI-5D. Figure SI-5E showed the normalized extinction spectra of AuNPs and AuNPs@MBA@SiO_2. The absorption feature attributed to agglomerated particles was shifted to approx. 750 nm and the LSPR of spherical AuNPs was shown at around 540 nm. The SERS spectra and their intensity at 1075 cm^{-1} of AuNPs@MBA@SiO_2 and non-agglomerated AuNPs@MBA@SiO_2 were shown in Figure SI-5F and the controlled agglomeration increased the SERS efficiency by 2 times.

2.4.2 AgNPs@MBA@SiO_2 SERS signal robustness analysis

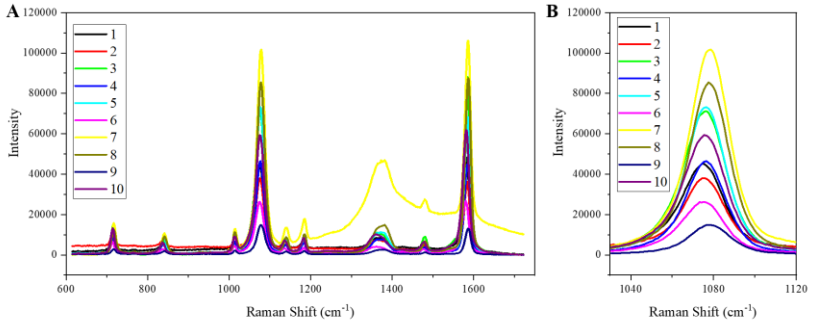

Figure 2: SERS characterization of different substrates wherein the AgNPs@MBA@SiO_2 has been placed on the surface. (A) SERS spectra and (B) zoomed spectra showing characteristic peak at 1075 cm^{-1} of AgNPs@MBA@SiO_2 on different subjects: 1. semi-aniline leather; 2. aniline leather; 3. pigmented leather; 4. polyester; 5. silk; 6. plastic (PVC); 7. glass; 8. brass; 9. cotton; and 10. dyed pigmented leather.

We analyzed the robustness of our synthesized AgNPs@MBA@SiO_2 by depositing them onto 10 different

substrates made of different materials and analyzing their SERS signals. Figure 2 showed the SERS spectra and zoomed characteristic peak at 1075 cm^{-1} of AgNPs@MBA@SiO_2 on different substrates, including semi-aniline leather, aniline leather, pigmented leather, polyester, silk, plastic (PVC), glass, brass, cotton and dyed pigmented leather, and Figure SI-6 showed the photos of these deposited substrates. The characteristic SERS bands of MBA were clearly observed. Except for glass, the background signal originated from the substrates was insignificant. However, the broad band between 1000 to 1800 cm^{-1} for glass did not significantly affect to the characteristic bands of MBA. This uneven SERS intensity for all the materials can be explained by the distribution differences of AgNPs@MBA@SiO_2 on different properties of substrates. To study the morphology and their distribution of AgNPs@MBA@SiO_2 on materials, SEM was applied. The deposited dyed pigmented leather and cotton were characterized and shown in Figure 3A and 3B, separately, with elemental analysis supporting the distribution of AgNPs@MBA@SiO_2 on dyed pigmented leather as shown in Figure 3C-F, spectrum 1 indicating the area covered by AgNPs@MBA@SiO_2 and spectrum 2 indicating the area without AgNPs@MBA@SiO_2. SEM images showed the distribution can vary with the surface properties of materials, including flatness and porosity, thus the SERS signal we obtained and showed in Figure 2 can be affected. The SERS signals we got from dyed pigmented leather were higher than cotton which was mainly caused by the higher flatness of dyed pigmented leather than cotton. With depositing AgNPs@MBA@SiO_2 on porous

materials, herein dyed pigmented leather and cotton, particles can be deposited on the surface or hided in-between the fibers.

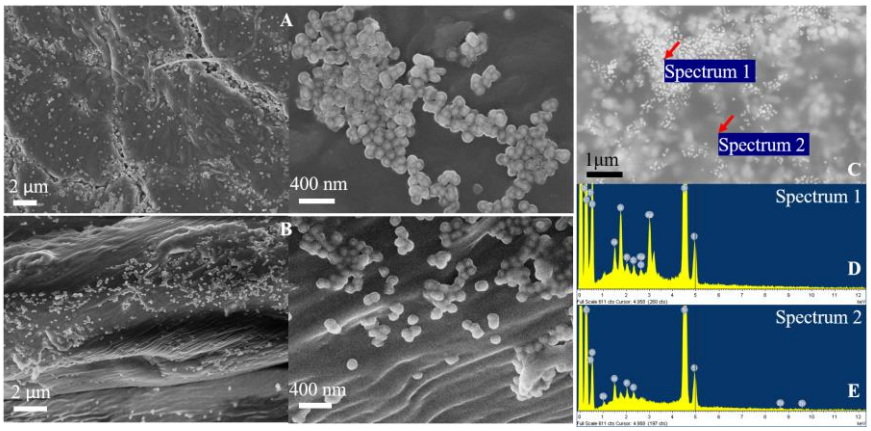

Figure 3: SEM and elemental analysis (EDX) of AgNPs@MBA@SiO_2 deposited materials. (A) SEM images of AgNPs@MBA@SiO_2 deposited on dyed pigmented leather. (B) SEM images of AgNPs@MBA@SiO_2 deposited cotton. (C) SEM images of AgNPs@MBA@SiO_2 deposited on dyed pigmented leather, showing pointed positions for elemental analysis and their corresponding spectra (D) spectrum 1 and (E) spectrum 2.

AgNPs@MBA@SiO_2 has robust SERS signals (as indicated, obtained in 0.1 s) and almost insignificant interfere by any material we used and demonstrated here. This provides our particles various potential applications where high Raman signal needed. One example, by using AgNPs@MBA@SiO_2 to label any type of good, it is possible to track along the whole supply chain, thus developing a method to avoid counterfeiting. Here, we demonstrated another bioapplication of our device and offered a detailed protocol for SARS-CoV-2 proteins detection in which combined SERS high sensitivity and ELISA selectivity.

2.4.3 SERS based ELISA for sensing spike protein of SARS-CoV-2

The surface of our devices was first modified with GPTMS through the reaction called epoxy-silanization[34]. To immobilize antibody to our devices, GPTMS here worked as a linking agent between the surface of silica and the antibody taking advantage of the free amino groups presented.

To confirm the successful immobilization of the antibody onto the silica surface, we carried out a parallel test using Confocal microscope. AgNPs@MBA@SiO_2 and the biofunctionalized AgNPs@MBA@SiO_2@Ab were incubated with a secondary antibody labeled with a fluorophore (Alexa Fluor® 488 AffiniPure Goat Anti-Mouse IgG). Figure SI-7 showed the confocal images obtained. Compared with no fluorescence signal coming from secondary antibody incubated AgNPs@MBA@SiO_2, the presence of bright fluorescence signal indicated the successful synthesis of biofunctionalized AgNPs@MBA@SiO_2@Ab.

SERS-based ELISA sensing surface is constructed by coating a capture antibody onto an ELISA plate, followed by the addition of spike protein solution. After washing out the non-specifically bonding protein, the surface was treated with AgNPs@MBA@SiO_2@Ab which would bind to targeted spike protein via a second recognition site and be resistant to washing.

We demonstrated that SERS signal from the plate which is made of polystyrene had no interfere with our characteristic SERS peak at 1075 cm^{-1}, as shown in Figure SI-8 by comparing the SESR spectra

of Elisa plate, AgNPs@MBA@SiO_2@Ab in buffer and Elisa results with 1 ng/μL spike protein.

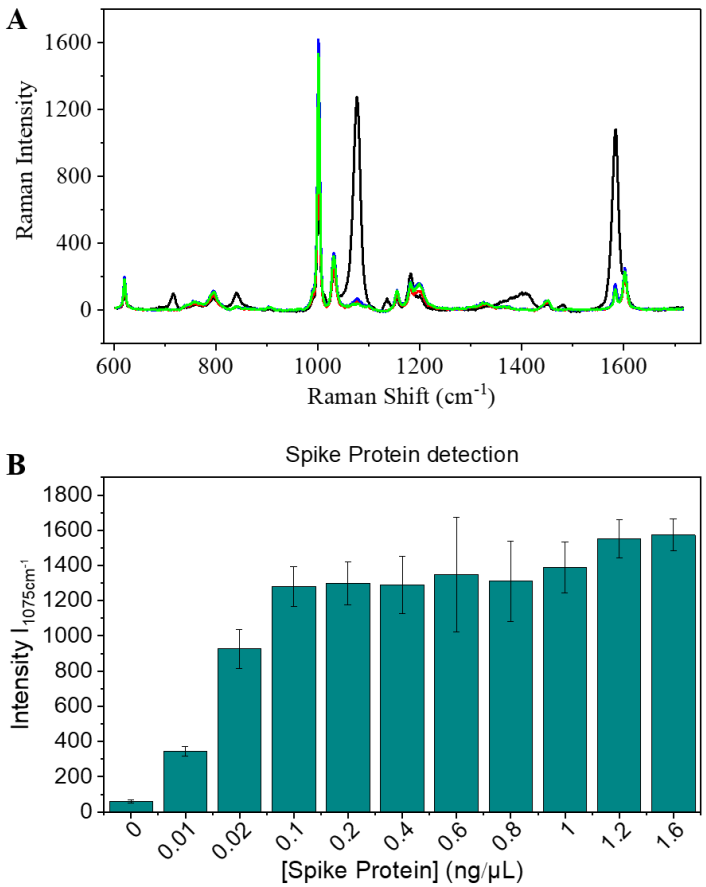

Figure 4: (A) Averaged SERS spectra collected in the presence of 0.1 ng/μL spike protein (black), and SESR spectra resulted from experiments omitting one or more of the elements of the assay (red, no spike protein; blue, no capture antibody; and green, neither spike protein nor capture antibody). Each spectrum was the average of 8 spectra of 8 random places in Elisa well. (B) SERS intensity at 1075 cm^{-1} showing Elisa results of AgNPs@MBA@SiO_2@Ab incubated with different amount of spike protein, from left to right: 0, 0.01, 0.02, 0.1, 0.2, 0.4, 0.6, 0.8, 1, 1.2, 1.6 ng/μL. Standard deviation are calculated with 8 spectra of 8 random places in Elisa well.

To confirming that the overall approach for spike protein detection

is effective, we did a serious of control assays as shown in Figure 4A. We obtained the most intense SERS signal from 0.1 ng/ μL spike protein treated sample, compared with the controls, which omitting one or more of the assay elements, including the absence of spike protein, the absence of capture antibody (the concentration of spike protein was increased to 1 ng/ μL), and the absences of both spike protein and capture antibody. The surfaces were treated with AgNPs@MBA@SiO_2@Ab in all the cases mentioned. The intensity ratio between 0.1 ng/ μL and absence of spike protein was more than 20 times, corresponding to MBA characteristic peak at 1075 cm^{-1}, showing excellent differentiation.

Then we conducted SERS-based ELISA assay with established protocol with a serious concentration of spike protein: 0, 0.01, 0.02, 0.1, 0.2, 0.4, 0.6, 0.8, 1, 1.2, 1.6 ng/μL. And the results based on the intensity of MBA characteristic peak at 1075 cm^{-1} was shown in Figure 4B. Intensity ratio between 0.01 and 0 ng/μL at 1075 cm-1 was close to 6, revealing a limit of detection (LOD) would be less than 0.01 ng/μL, based on a 3:1 threshold ratio. We also need to mention that with spike protein concentration higher than 0.1 ng/μL, the assay response would be less sensitive to concentration of the targeted spike protein. This would not be a problem when applying for qualitatively assay in this range since all clearly showed positive response to targeted spike protein. This designed AgNPs@MBA@SiO_2@Ab, with amplification by SERS signals offering high sensitivity and selectivity from antibodies, can be used in sandwich type protocols of ELISA.

2.5 CONCLUSION

We designed and synthesized one nanostructure made of silver silica nanocomposites. We studied the fundamental factors for the modification of AgNPs. In general, weak basic environment facilitated the codification of Raman probe onto silver metallic surface forming silver thiol bond. While, dissociation of this silver thiol covalent bond would be favored with continuous increasing system pH. Thus, controlled system pH is critical for optimized modification of thiolated compound onto metallic surfaces. We also found that ethanol has less effect on the formation of silver thiol bond. The final packing quality of the Raman probe monolayer would be affected by the metal-thiol bonding formation speed, the electrostatic repulsion on the metallic surface, and the competition between Raman probe and stabilizer. Then controlled agglomeration to increase the percentage of hot spots performed, with SERS signal increase nearly 40 times. This encoded silver nanoagglomerates were encapsulated and protected by silica layer which can be potentially multi-functionalized. This nanostructure was deposited onto different materials and showed robust signal without interfere. With robust and homogeneous SERS signal, this nanostructure can be potentially applied for many applications. With further biofunctionalization with antibody onto silica layer, we built up a device for SERS-based ELISA SARS-CoV-2 detection targeting to the spike protein. We offered one convenient and reliable tool for biosensing.

2.6 REFERENCES

1. Seale-Goldsmith, M-M. & Leary J. F. Nanobiosystems. *Wiley Interdiscip. Rev. Nanomed. Nanobiotechnol.* **1**, 553-567 (2009).

2. Tiu, B. D. B. & Advincula, R. C. Plasmonics and templated systems for bioapplications. *Rend. Fis. Acc. Lincei* **26**, 143–160 (2015).

3. Im, H. *et al.* Label-free detection and molecular profiling of exosomes with a nano-plasmonic sensor. *Nat. Biotechnol.* **32**, 490–495 (2014).

4. Kim, E., Baaske, M. D., Schuldes, I., Wilsch, P. S. & Vollmer, F. Label-free optical detection of single enzyme-reactant reactions and associated conformational changes. *Sci. Adv.* **3**, : e1603044 (2017).

5. Wu, X. *et al.* Propeller-Like Nanorod-Upconversion Nanoparticle Assemblies with Intense Chiroptical Activity and Luminescence Enhancement in Aqueous Phase. *Adv. Mater.* **28**, 5907–5915 (2016).

6. Beeram, S. R. & Zamborini, F. P. Selective attachment of antibodies to the edges of gold nanostructures for enhanced localized surface plasmon resonance biosensing. *J. Am. Chem. Soc.* **131**, 11689–11691 (2009).

7. Hudson, S. D. & Chumanov, G. Bioanalytical applications of SERS (surface-enhanced Raman spectroscopy). *Anal. Bioanal. Chem.* **394**, 679–686 (2009).

8. Maher R. C. SERS Hot Spots. In: Kumar C.S.S.R. (eds) Raman Spectroscopy for Nanomaterials Characterization. Springer, Berlin, Heidelberg. https://doi.org/10.1007/978-3-642-20620-7_10. (2012).

9. Anderson, D. J. & Moskovits, M. A SERS-active system based on silver nanoparticles tethered to a deposited silver film. *J. Phys. Chem. B* **110**, 13722–13727 (2006).

10. Tabatabaei, M. *et al.* Optical properties of silver and gold tetrahedral nanopyramid arrays prepared by nanosphere lithography. *J. Phys. Chem. C* **117**, 14778–14786 (2013).

11. Kang, T. *et al.* Ultra-specific zeptomole MicroRNA detection by plasmonic nanowire interstice sensor with Bi-temperature hybridization. *Small* **10**, 4200–4206 (2014).

12. Si, Y. *et al.* Alkyne-DNA-Functionalized Alloyed Au/Ag Nanospheres for Ratiometric Surface-Enhanced Raman Scattering Imaging Assay of Endonuclease Activity in Live Cells. *Anal. Chem.* **90**, 3898–3905 (2018).

13. Zhang, C., Liu, X., Xu, Z. & Liu, D. Multichannel Stimulus-Responsive Nanoprobes for H_2O_2 Sensing in Diverse Biological Milieus. *Anal. Chem.* **92**, 12639–12646 (2020).

14. Hwang, J., Lee, S. & Choo, J. Application of a SERS-based lateral flow immunoassay strip for the rapid and sensitive detection of staphylococcal enterotoxin B. *Nanoscale* **8**, 11418–11425 (2016).

15. Tripp, R. A., Dluhy, R. A. & Zhao, Y. Novel nanostructures

for SERS biosensing. *Nano Today* **3**, 31–37 (2008).

16. Corman, V. *et al.* Detection of 2019 -nCoV by RT-PCR. *Euro Surveill* **25**, 2000045 (2020).

17. Moitra, P. *et al.* Selective Naked-Eye Detection of SARS-CoV-2 Mediated by N Gene Targeted Antisense Oligonucleotide Capped Plasmonic Nanoparticles. *ACS Nano* **14**, 7617–7627 (2020).

18. Huang, C., Wen, T., Shi, F. J., Zeng, X. Y. & Jiao, Y. J. Rapid Detection of IgM Antibodies against the SARS-CoV-2 Virus via Colloidal Gold Nanoparticle-Based Lateral-Flow Assay. *ACS Omega* **5**, 12550–12556 (2020).

19. Qiu, G. *et al.* Dual-Functional Plasmonic Photothermal Biosensors for Highly Accurate Severe Acute Respiratory Syndrome Coronavirus 2 Detection. *ACS Nano* **14**, 5268–5277 (2020).

20. Qiu, M. *et al.* Antibody responses to individual proteins of SARS coronavirus and their neutralization activities. *Microbes Infect.* **7**, 882–889 (2005).

21. Paramelle, D. *et al.* A rapid method to estimate the concentration of citrate capped silver nanoparticles from UV-visible light spectra. *Analyst* **139**, 4855–4861 (2014).

22. Lee, P. C. & Meisel, D. Adsorption and surface-enhanced Raman of dyes on silver and gold sols. *J. Phys. Chem.* **86**, 3391–3395 (1982).

23. Mir-Simon, B., Reche-Perez, I., Guerrini, L., Pazos-Perez, N.

& Alvarez-Puebla, R. A. Universal one-pot and scalable synthesis of SERS encoded nanoparticles. *Chem. Mater.* **27**, 950–958 (2015).

24. Michota, A. & Bukowska, J. Surface-enhanced Raman scattering (SERS) of 4-mercaptobenzoic acid on silver and gold substrates. *J. Raman Spectrosc.* **34**, 21–25 (2003).

25. Kneipp, J., Kneipp, H., Wittig, B. & Kneipp, K. One-and Two-Photon Excited Optical pH Probing for Cells Using Surface-Enhanced Raman and Hyper-Raman Nanosensors. *Nano Lett.* **7**, 2819-2823 (2007).

26. Gelsema, W. J., de Ligny, C. L., Remijnse, A. G. & Blijleven, H. A. pH- Measurements in alcohol- water mixtures, using aqueous standard buffer solutions for calibration. *Recl. des Trav. Chim. des Pays - Bas* **85**, 647–660 (1966).

27. Tielens, F. & Santos, E. AuS and SH bond formation/breaking during the formation of alkanethiol SAMs on Au(111): A theoretical study. *J. Phys. Chem. C* **114**, 9444–9452 (2010).

28. Hiramatsu, H. & Osterloh, F. E. pH-controiled assembly and disassembly of electrostatically linked CdSe-SiO_2 and Au-SiO2 nanoparticle clusters. *Langmuir* **19**, 7003–7011 (2003).

29. Jung, J., Kang, S. & Han, Y. K. Ligand effects on the stability of thiol-stabilized gold nanoclusters: $Au_{25}(SR)_{18}$-, $Au_{38}(SR)_{24}$, and $Au_{102}(SR)_{44}$. *Nanoscale* **4**, 4206–4210

(2012).

30. Bhatt, N., Huang, P. J. J., Dave, N. & Liu, J. Dissociation and degradation of thiol-modified DNA on gold nanoparticles in aqueous and organic solvents. *Langmuir* **27**, 6132–6137 (2011).

31. Xue, Y., Li, X., Li, H. & Zhang, W. Quantifying thiol-gold interactions towards the efficient strength control. *Nat. Commun.* **5**, 5348 (2014).

32. Wong, Y. J. *et al.* Revisiting the Stöber method: Inhomogeneity in silica shells. *J. Am. Chem. Soc.* **133**, 11422–11425 (2011).

33. Turkevich, J., Stevenson, P. C. & Hillier, J. A study of the nucleation and growth processes in the synthesis of colloidal gold. *Discuss. Faraday Soc.*, **11**, 55–75 (1951).

34. Banjanac, K. *et al.* Epoxy-silanization - tool for improvement of silica nanoparticles as support for lipase immobilization with respect to esterification activity. *J. Chem. Technol. Biotechnol.* **91**, 2654–2663 (2016).

2.7 SUPPORTING INFORMATION

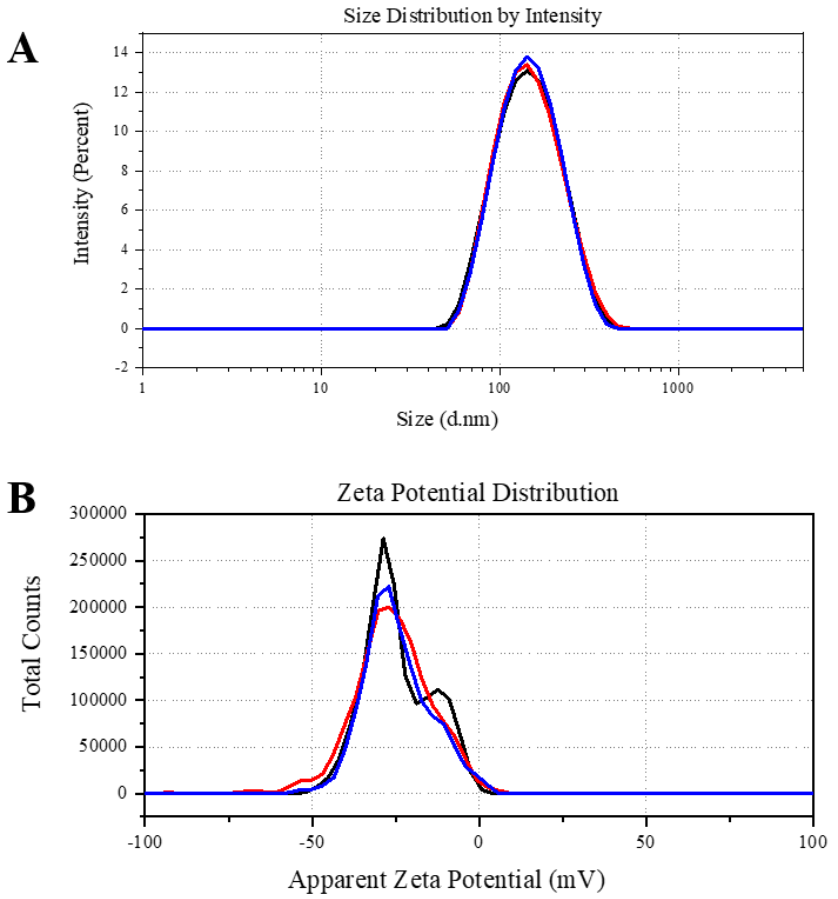

Figure SI-1: Characterization of AgNPs@MBA@SiO_2. (A) Size measurements (3 repeated runs) of AgNPs@MBA@SiO_2, with mean value 133.8 nm and PDI 0.130. (B) Zeta potential measurements (3 repeated measurements) of AgNPs@MBA@SiO_2, with mean value -24.7 mV.

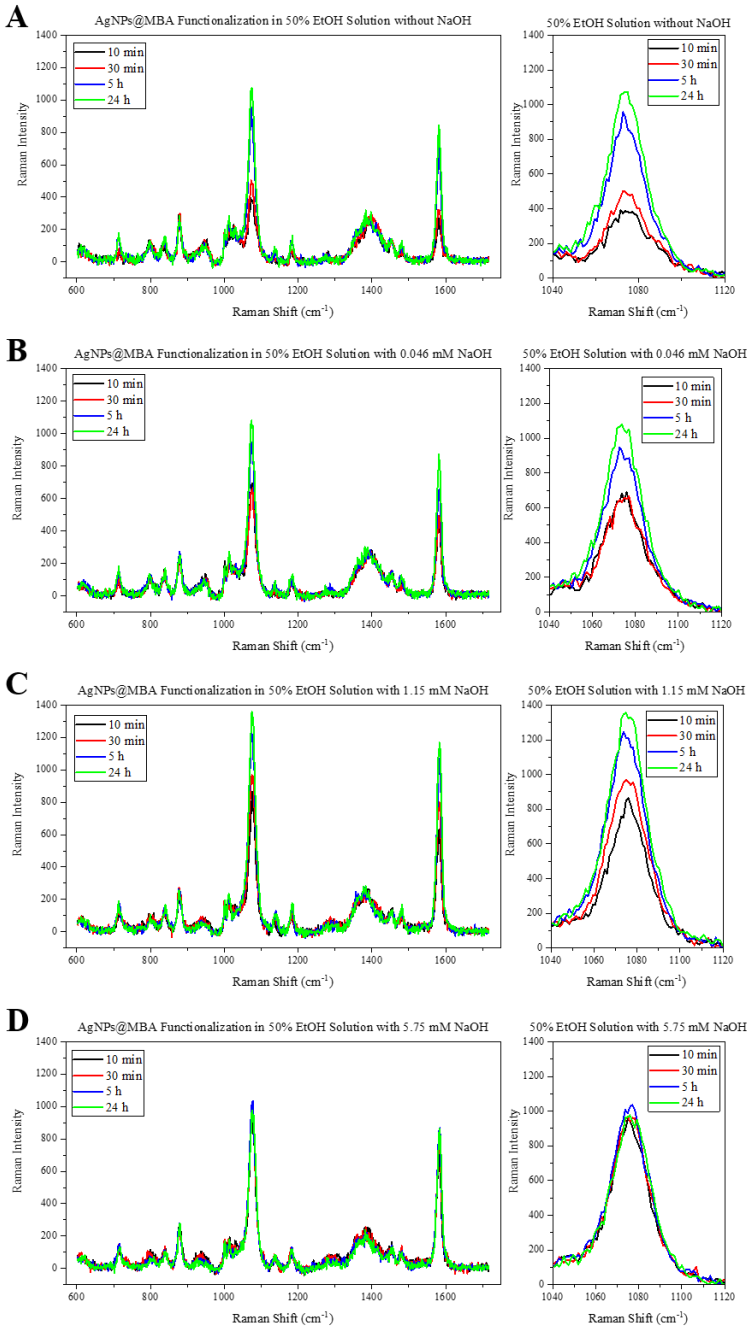

Figure SI-2: SERS spectra and zoomed spectra showing characteristic peak at 1075 cm^{-1} of AgNPs@MBA in 50% EtOH/water solution without NaOH (A), with 0.046 mM NaOH (B), with 1.15 mM NaOH (C) and with 5.75 mM NaOH (D) at 10 min (in black), 30 min (in red), 5 h (in blue) and 24 h (in green).

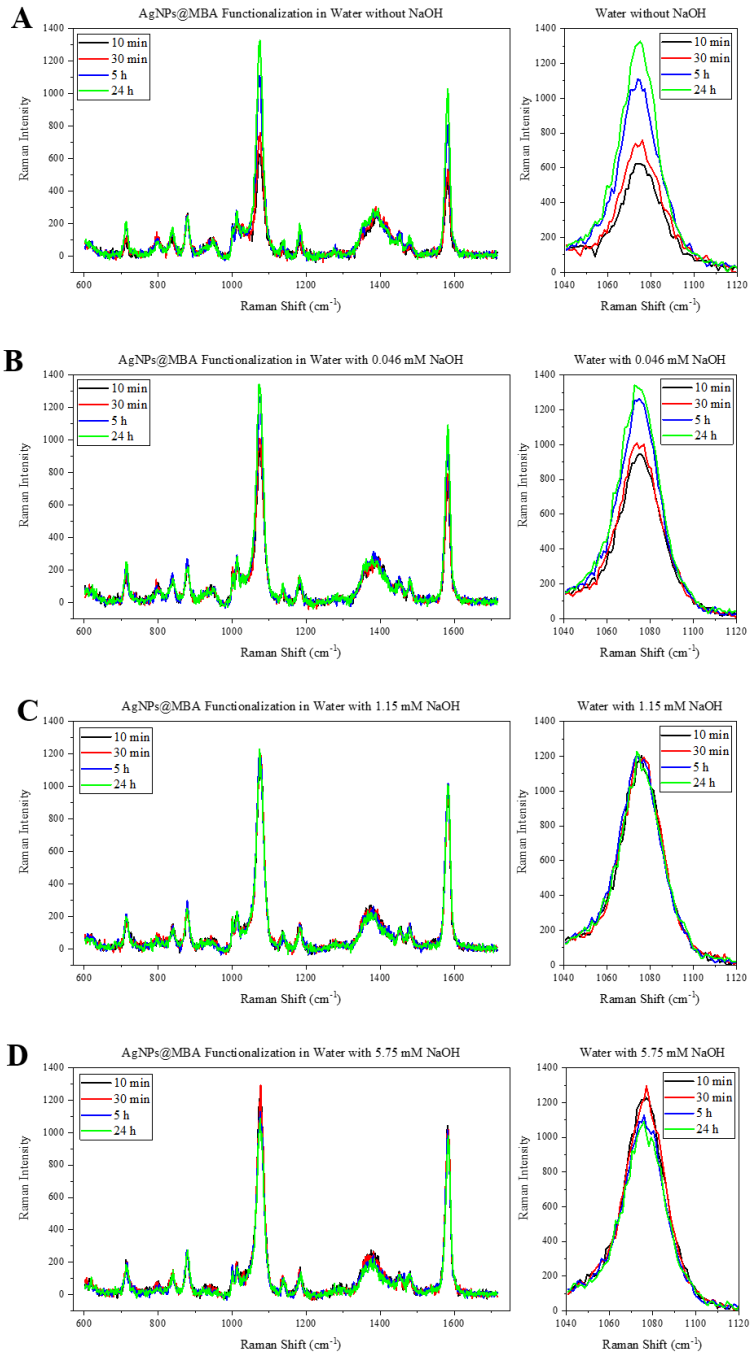

Figure SI-3: SERS spectra and zoomed spectra showing characteristic peak at 1075 cm^{-1} of AgNPs@MBA in aqueous solution without NaOH (A), with 0.046 mM NaOH (B), with 1.15 mM NaOH (C) and with 5.75 mM NaOH (D) at 10 min (in black), 30 min (in red), 5 h (in blue) and 24 h (in green).

NaOH Amount	pH in aqueous solution	pH in 50% ethanol/water solution
without NaOH	6	6.5
0.046mM NaOH	8.5	6.5
1.15mM NaOH	11	8
5.75mM NaOH	11.5	9.5

Table SI-1: pH of all codification systems used for MBA modification, measured by pH test strips.

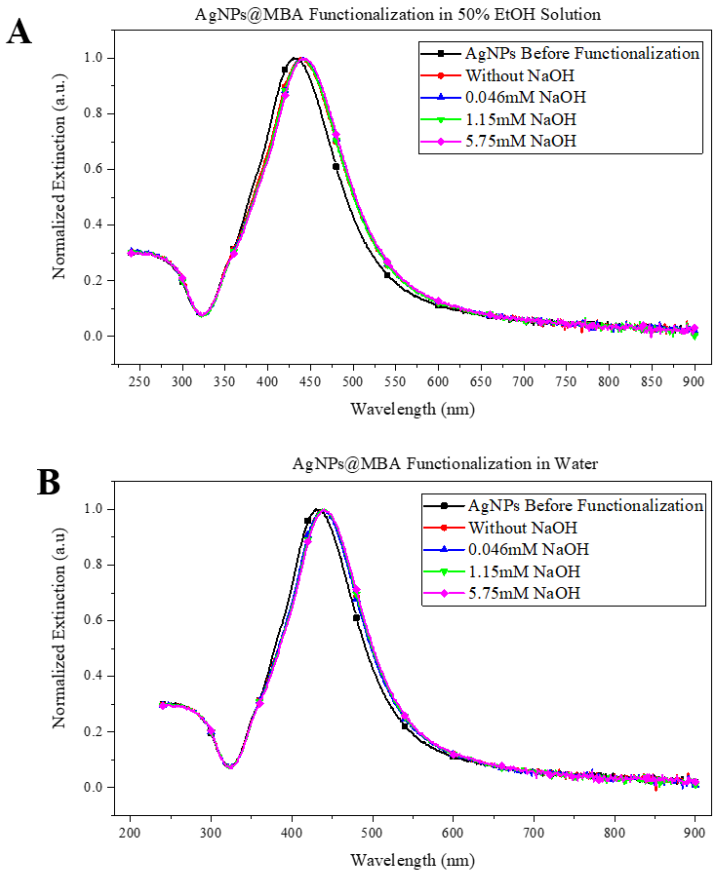

Figure SI-4: UV-Visible extinction spectra of MBA modified AgNPs (AgNPs@MBA) with different amount of NaOH in 50%EtOH/water solution (A) and in aqueous solution (B). Black line: AgNPs; Red line: AgNPs@MBA without NaOH; Blue line: AgNPs@MBA with 0.046 mM NaOH; Green line: AgNPs@MBA with 1.15 mM NaOH; Magenta Line: AgNPs@MBA with 5.75 mM NaOH.

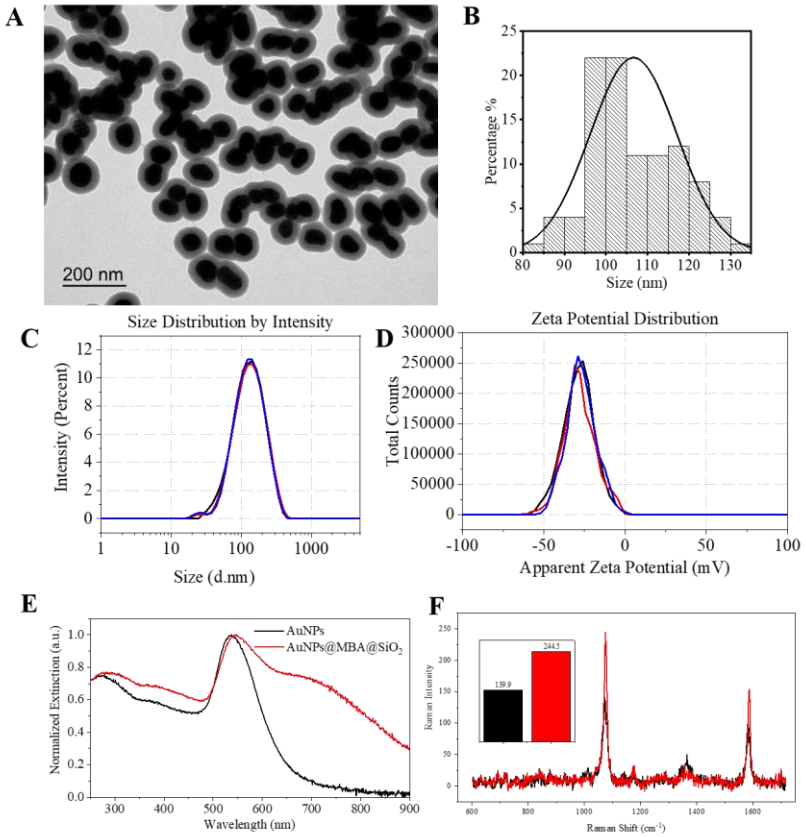

Figure SI-5: Characterization of AuNPs@MBA@SiO_2. (A) TEM image of AuNPs@MBA@SiO_2. (B) Size distribution of AuNPs@MBA@SiO_2 based on 100 nanoparticles from TEM images analyzed with ¨Image J¨. (C) Size measurements (3 repeated runs) of AuNPs@MBA@SiO_2, with mean value 113.6 nm and PDI 0.199; (D) Zeta potential measurements (3 repeated measurements) of AuNPs@MBA@SiO_2, with mean value -27.9 mV. (E) UV-Visible extinction spectra of AuNPs (in black) and AuNPs@MBA@SiO_2 (in red). (F) SERS spectra and SERS intensity at 1075 cm^{-1} (inset image) of non-agglomerated AuNPs@MBA@SiO_2 (in black) and AuNPs@MBA@SiO_2 (in red).

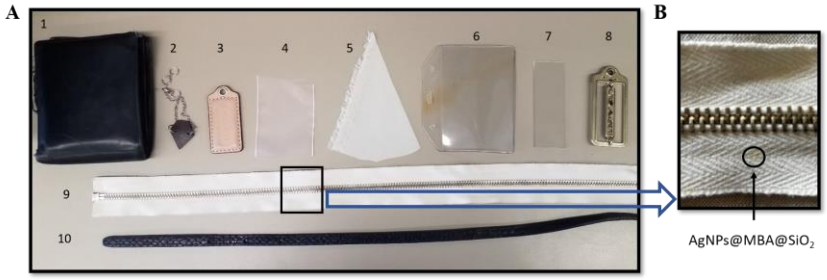

Figure SI-6: (A) Photos of 10 substrates which have AgNPs@MBA@SiO_2 deposited on the surface. (B) zoomed photo showing AgNPs@MBA@SiO_2 deposited on cotton. 1, semi-aniline leather; 2, aniline leather; 3, pigmented leather; 4, polyester; 5, silk; 6, plastic (PVC); 7, glass; 8, brass; 9, cotton; and 10, dyed pigmented leather.

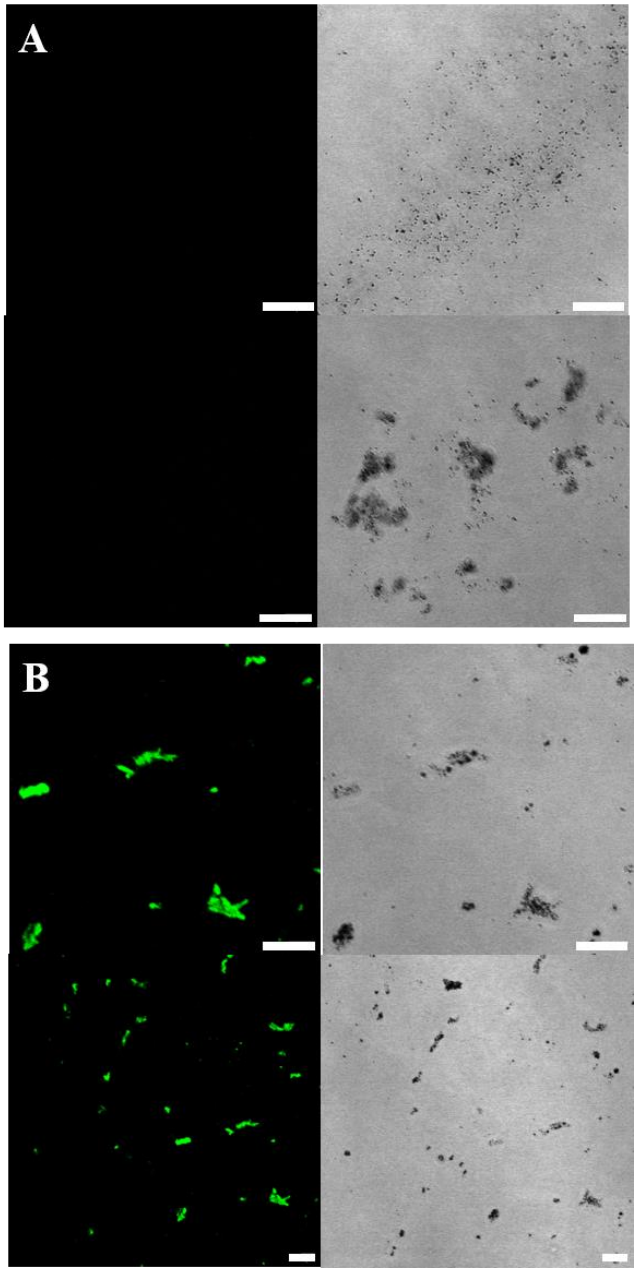

Figure SI-7: Synthesis and characterization of AgNPs@MBA@SiO_2@Ab. (A) Confocal images showing fluorescence results of AgNPs@MBA@SiO_2 incubated with secondary antibody. (B) Confocal images showing fluorescence results of AgNPs@MBA@SiO_2@Ab incubated with secondary antibody. Secondary antibody used here is Alexa Fluor® 488 AffiniPure Goat Anti-Mouse IgG. Scale bar in all confocal images is for 10 μm.

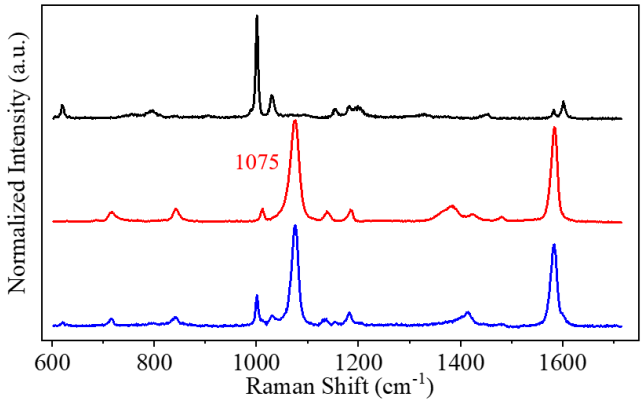

Figure SI-8: SESR spectrum of Elisa plate (made of polystyrene) (in black), SESR spectrum of AgNPs@MBA@SiO_2@Ab in buffer showing characteristic peak at 1075 cm^{-1} (in red), and Elisa results after AgNPs@MBA@SiO_2@Ab incubated with 1 ng/µL spike protein (in blue).

3. Real time and spatiotemporal quantification of pH and hydrogen peroxide imbalances with a multiplex SERS nanosensor

3.1 ABSTRACT

Hydrogen peroxide (H_2O_2) serves as a key metabolite in physiological and pathological processes. The quantification of H_2O_2 is essential for mechanistic understanding on redox reactions and redox therapeutics. We provided a plasmonic sensor for sensitive and reliable *in vitro* H_2O_2 and pH determination based on 3-mercaptophenylboronic acid and 4-mercaptobenzoic acid modified gold/silica nanocapsules coupled with surface-enhanced Raman spectroscopy (SERS). The complexation of boronic acid with a third hydroxyl group in 3-mercaptophenylboronic acid modified nanocapsules enhanced this B-C bond cleavage sensitivity by H_2O_2 when suspended in alkaline pH, thus different calibration curves were obtained under physiological pH range. This pH effect on oxidation can be further applied to all H_2O_2 measurements which are based on aromatic boronic acid oxidation coupled with fluorescence or SERS. Lysosomal H_2O_2 was quantified to complement intracellular H_2O_2 profile. We found intracellular H_2O_2 concentration in different organelles of endocytic pathways were equivalent. The gradient was approx. 40-fold between extracellular and intracellular hydrogen peroxide concentration which enrich the database to build a compartmental model for understanding

intracellular H_2O_2 based on observing extracellular H_2O_2 perturbations. We offered a real time multiplex nanosensor for local H_2O_2 and pH analysis within single cell.

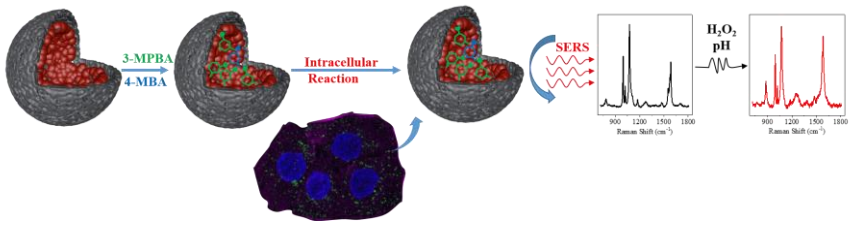

Scheme 1: Scheme representing the methodology for intracellular hydrogen peroxide and pH monitoring.

3.2 INTRODUCTION

The presence and progression of certain diseases are associated with the changes of biomolecules[1]. There are close interrelations between diseases markers which can affect clinical outcome. To understand cellular mechanisms in healthy state and diseases progression, multiplex analysis of biomolecules in a complex mixture is essential. Compared with classical bioanalytical strategies, which each analyte is individually determined, multiplex technologies permit simultaneous measurements of multiple analytes in a single run of the assay within a small sample[2]. Multiplex sensing is a rapid and accurate diagnostic method, which also provide significantly more information about the health state of an individual.

Reactive oxygen species (ROS) are generated under both physiological and pathological situations. Imbalance generation of

ROS results in oxidative stress, which involves in neurodegenerative disorder (like Alzheimer disease[3]), carcinogenesis[4,5] and aging[6]. Among all the species of ROS, hydrogen peroxide (H_2O_2), one of the most important transcription independent signal molecule[7], serves as a key metabolite in redox sensing, signaling and redox regulation, because of its unique chemistry properties: long lifetime and uncharged nature allowing transportation and remote signaling[8]. Cellular effects are initiated under permeation of H_2O_2 through cells and tissues. Average intracellular H_2O_2 physiological concentration in mammalian cells likely ranges from 1 to 700 nM. Stress and adaptive stress responses, even inflammatory responses and cell death occur at higher H_2O_2 concentrations[9]. No matter for better understanding on redox reactions or for better control of redox therapeutics, facile measurement of the intracellular concentration of hydrogen peroxide has been a focused interest and a long-standing challenge.

The classical methods for H_2O_2 concentration determination are with fluorescent dyes, among which the most common chemical assays are horseradish peroxide (HRP)-dependent probes (ref10). The noteworthy disadvantage of those assays is that the detection is limited to extracellularly available H_2O_2[10]. More sophisticated sensors are genetically encoded fluorescent indicators, like HyPer probe[11] and roGFP-orp1[12], which are designed to be used for intracellular H_2O_2. Despite the common fluorescence limitations, *e.g.*, complicated synthesis of probes and photobleaching issues, they have their specific limitations. Hyper probes are pH sensitive, and virus transfected cells are needed for roGFP-orp1, and *in situ*

quantification are complicated to realize, which hampers their popularity[10].

Surface-enhanced Raman spectroscopy (SERS) retains the rich chemical and structural information provided by Raman spectroscopy but overcomes its inherent limitation to the investigation of low amounts of material, especially when interparticle hot-spots occur. This provides a nondestructive and sensitive tool to investigate chemical modifications of the probe molecule onto the platform since the analyte recognition can induce characteristic spectral changes. Nanosphere[13,14], core-satellite[15] and core-shell[16] nanoparticles based on gold have been previously reported for H_2O_2 SERS sensing. The Raman probes used for *in vitro* H_2O_2 SERS sensing are mainly boronate molecules with high Raman cross-section: 3-Mercaptophenylboronic acid (3-MPBA)[13], 4-MPBA[15] and others[14]. However, all of them carried the Raman probes in the outer side of the nanostrucrture, *i.e.*, at the interface with the media. Biomolecules can come in close contact and further be adsorbed on the metallic surface when nanoparticles are exposed to biological media. The presence of biomolecules (*e.g.*, Glutathione) can replace or remove the Raman probes from the metallic surface since they are not well protected[17]. And detectable Raman signals of biomolecules can be induced which interferes with the signal of the Raman probes. This has important limitations hampering the sensitivity and reliability of the quantification, thereby compromising their biomedical sensing applications. Besides, the reported nanoparticles are in a size range below 100 nm, thus isolated nanoparticles are not visible with a Raman

microscope. Uncontrollable agglomeration and aggregation occur in biological and physiological media which can induce strong heterogeneous SERS response[18]. Moreover, none of the articles discussed the pH effect on aromatic boronates oxidation for H_2O_2 sensing. Especially when nanoparticles were internalized inside cells, identifying the location and the local pH are essential for H_2O_2 sensing.

Lysosomal H_2O_2 reacts with labile iron forming hydroxyl redicals, which may cause lysosomal rupture and further proapoptotic cascade[19]. And the accumulation of peroxidized lipids and proteins in lysosomes of the brain cells is one of the known reasons in Alzheimer disease[20]. To complete intracellular H_2O_2 profile, apart from previous studies on mitochondria and cytosol H_2O_2 [11,21], it is important to understand lysosomal H_2O_2. Another aspect, concentration gradients exist both from extracellular to intercellular and between subcellular compartments[8]. Previous estimations suggested that extracellular H_2O_2 is around 10-fold[22] or 650-fold[23] higher than intracellular concentration, due to the intracellular H_2O_2 metabolism[24], varying with cell type and locations inside cells and various parameters[8,25]. By building a compartmental model to estimate the gradients between extracellular and intracellular H_2O_2, the intracellular H_2O_2 concentration and cellular responses can be potentially estimated by simply observing extracellular H_2O_2 perturbations[23]. To address this need, sensors which can be used for both extracellular and intracellular monitoring are required.

In this study, nanocapsules (NCs) were synthesized as a sensitive and reliable *in vitro* H_2O_2 and pH sensor. NCs which assembled

gold nanostructures produce strong and homogenous SERS response and allow for single-nanocapsule analysis taking advantage of interparticle hot-spots concentrated in their inner shell. Moreover, the silica shell offers intrinsic resistance against aggregation and prevents physicochemical interaction between the gold nanoparticles and the proteins from biological media. As shown in Scheme 1, multiplex sensors were obtained by modifing the gold surface with thiolated aromatic molecules 3-MPBA and 4-mercaptobenzoic acid (4-MBA) for H_2O_2 and pH determination, respectively, as their chemical modifications can be recognized as characteristic Raman spectral changes. Moreover, our sensor offered more information to study both intracellular and extracellular H_2O_2. We created one convenient multiplex sensor for intracellular and extracellular H_2O_2 and pH determination.

3.3 EXPERIMENTAL SECTION

3.3.1 Materials and Reagents

3-MPBA, 4-MBA, 3-Mercaptophenol (3-MP), 2,2´-Azobis(2-methylpropionamidine) dihydrochloride (AIBA), Polyvinylpyrrolidone (PVP, MW: 10000), Styrene, polysodium(styrene sulfonate) (PSS, MW: 70000), Poly(allylamine hydrochloride) (PAH, MW: 50000), Tetrakis(hydroxymethyl)phosphonium chloride solution (THPC), Gold(III) chloride trihydrate, Ammonia solution, Tetraethyl orthosilicate (TEOS), Phosphoric acid, Sodium phosphate monobasic, Sodium phosphate dibasic, Hydrogen peroxide solution

and Menadione were purchased from Sigma-Aldrich. Sodium hydroxide, lysotracker, cellmask and mitotracker were purchased from ThermoFisher. Bafilomycin A1 was purchased from ChemCruz and Chloroform was purchased from Scharlau. All the chemicals were used without further purification.

Polystyrene (PS) beads were synthesized as previous reported[26]. Polymerization was carried out with AIBA as an initiator. Styrene was added to PVP and AIBA mixture at 70 ºC. The reaction was kept at 70 ºC for 24 h. (Controlling Size and Distribution for Nano-sized Polystyrene Spheres)

PSS solution and PAH solution (1 mg/ml containing 0.5 M NaCl) were prepared freshly before use. 100 mM phosphate buffer with pH ranging from 4 to 9 were prepared with phosphoric acid, sodium phosphate monobasic and sodium phosphate dibasic. By adding series concentrations of H_2O_2 solution into phosphate buffer (0.5% (v/v)), H_2O_2 concentration from 10^{-2} M to 10^{-8} M under full range of pH obtained. pH was measured again and confirmed to be maintained after H_2O_2 addition.

3.3.2 NCs synthesis

NCs were produced with the method reported[27]. Briefly, polystyrene (PS) beads were decorated with gold nanoparticles by using a layer-by-layer (LbL) assembly protocol. Negatively charged PSS and positively charged PAH were alternatively deposited onto PS beads of 450 nm diameter to form a final dense external layer of PAH. Consecutively, significant excesses of negatively charged 3-5 nm diameter of Au nanoparticles (Au-seeds) were added and left to

adhere *via* electrostatic interaction. The PS@Au-seeds structures were then extensively washed to remove the unbound nanoparticles. Thereafter, PS@Au-seeds were coated with a polyvinylpyrrolidone (PVP) layer and covered with a silica shell. Hollow silica capsules containing Au-seeds were obtained by dissolving the PS cores with an ethanol/chloroform mixture. In order to increase the plasmonic efficiency of the nanostructure, Au-seeds inside the NCs were grown by *in situ* seed catalyzed reduction of gold ions with formaldehyde.

3.3.3 Morphological characterization

The morphology of the NCs synthesized have been examined by using a JEOL JEM 1010 transmission electron microscopy (TEM) operating at an acceleration voltage of 80 kV with a tungsten filament. The absorption spectrum of each synthetic intermediate has been analyzed with an UV-Vis spectrometer (GE Healthcare Ultrospec 2100 pro). Dynamic light scattering (DLS) and zeta potential analysis were performed with Zetasizer Nano ZS (Malvern Instruments, UK) which is capable of both particle size analysis and zeta-potential measurement.

3.3.4 SERS sensor preparation

Mixed self-assembled monolayer (SAM) methodology was used for the modification of NCs. Nanosensors were obtained by saturating the gold surface with thiolated aromatic molecules (3-MPBA, 3-MP and 4-MBA). 3-MPBA and 3-MP feedstock solutions were prepared with a concentration of 5 mM in ethanol. NCs were mixed and incubated with feedstock solutions for at least 3 h, followed by

centrifugation to remove the excess molecule. Centrifugation (5k rcf, 2 min) were repeated 4 times. After each centrifugation, NCs were resuspended into ethanol.

3.3.5 SERS measurements

The laser was focused into the samples with an 60X (NA 1.00) water immersion objective, providing a laser spot diameter of approximate 1 μm. The inelastic radiation was collected with a Renishaw's inVia Qontor Raman system equipped with a confocal optical microscope, a grating of 1200 $l \cdot mm^{-1}$, a NIR laser (785 nm) and a Peltier cooled CCD array detector. Samples were studied with Windows-based Raman Environment (Wire™) software.

Glass bottom dishes (IBIDI) were used for Raman measurements. For non-cell samples, modified NCs were suspended into phosphate buffer or cell growth medium with a concentration of 0.018 pmol/L (calculated by number of NCs). NCs were incubated with H_2O_2 solution for 30 minutes before Raman measurements. Integration time was set to 10 s and a power at the sample of 5 mW. Laser power of 10 mW and exposure time 20 s used for *in vitro* Raman experiments. Living cells were incubated in growth media when collecting Raman signals.

The pre-processing steps were done with Spyder (anaconda3). Spectra baseline were subtracted by asymmetric least squares smoothing algorithm in order to eliminate the auto fluorescence background[28].

3.3.6 Cell culture and viability assay

HT29 cells (colon cancer cells) were cultured in Dulbecco's Modified Eagle Medium/Nutrient Mixture F-12 (DMEM/F12, Thermofisher) supplemented with 10% Fetal bovine serum(FBS) 1% L-glutamine and 1% penicillin-streptomycin.

Cell viability assay was conducted with *in vitro* Toxicology Assay Kit (Resazurin based). 20k cells per well HT29 cells were seeded in a 96-well in triplicate in 100 µl growth medium. After cell attachment and 70% confluence, cells were treated with SiO_2 NCs with concentrations from 0.018 to 2.3 pmol/L. After 24 h of incubation, a solution of 10% resazurin in cell growth media is added to each well at a final volume of 100 µl/well. Then, cells were placed for 3 h in the incubator to metabolize the resazurin (non-fluorescent compound) into resorufin (fluorescent compound). The 96-well plate was read by fluorescence measurement, 560 nm and 580 nm for excitation and emission respectively, using a fluorescence spectrophotometer (Agilent Technologies). Fluorescence intensities of treated samples were normalized to the untreated control (cells without SiO_2 NCs treatment). Data was plotted with GraphPad Prism6.

3.3.7 *In vitro* experiments

HT29 were grown onto glass bottom dishes (IBIDI). After sufficient cell attachment, 0.072 pmol/L modified NCs were incubated with HT29 for 24 h. Living cells were incubated in cell growth medium for Raman measurements. The internalization of NCs by HT29 after 24 hours has verified with confocal laser scanning microscope (CLSM) (Leica TCS SP5 AOBS (inverted)). For H_2O_2 treated

HT29, cells were incubated with 0.5 to 10 mM H_2O_2 in cell growth media for 30 min before Raman and CLSM analysis. Intracellular H_2O_2 was checked by CLSM with Premo™ Cellular Hydrogen Peroxide Sensor. For Bafilomycin A1 stimulation, HT29 cells were incubated with 500 nM Bafilomycin A1 in cell growth media for 2 h. pH changes inside lysosomes were verified by CLSM with lyostracker green.

3.4 RESULTS AND DISCUSSION

3.4.1 Synthesis and characterization of 3-MPBA modified NCs

We have synthesized a complex nanostructure composed of hollow polymeric silica NCs with a high density of plasmonic gold nanoparticles placed on the inner surface of the NCs following previously established protocol[27]. This hybrid material acts as a robust nanocarrier of large ensembles of interparticle hot spots concentrated in their internal surface. This provides high SERS activity *via* interparticle coupling and a highly averaged plasmonic response that ensures great homogeneity within capsule-to-capsule Raman signal enhancement. To obtain the colloidal H_2O_2 sensor, we saturated the gold surface with a thiolated aromatic molecule 3-MPBA which has high Raman cross section. The functionalization of the NCs surface occurs *via* strong covalent gold-thiol bond. We selected 3-MPBA as a H_2O_2 sensor molecule because it can be oxidized into 3-hydroxyl thiophenol (3-MP) in the presence of H_2O_2 showing new SERS characteristic bands of 3-MP[13].

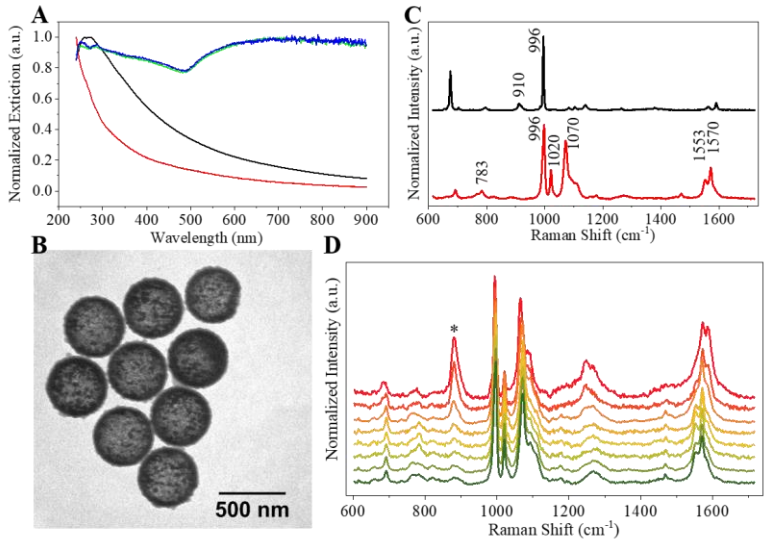

Figure 1: Synthesis and characterization of NCs@3-MPBA. (A) UV-Visible extinction spectra of the different steps during the synthesis of NCs@3-MPBA. Black line: PS beads; Red line: Au seeds@SiO_2 NCs; Green line: AuNPs@SiO_2 NCs; Blue line: NCs@3-MPBA. (B) TEM image of AuNPs@SiO_2 NCs. The size of the NCs was approx. 450 nm. (C) Raman spectrum of 3-MPBA in powder (Black line) and SERS spectrum of 3-MPBA anchored in AuNPs@SiO_2 NCs (Red line). (D) NCs@3-MPBA dispersed in pH7 phosphate buffer with different H_2O_2 concentrations (10^{-2} M, 10^{-3} M, 10^{-4} M, 10^{-5} M, 10^{-6} M, 10^{-7} M, 10^{-8} M, 0 M) (from red to green), showing how the intensity at 882 cm^{-1} (*) decreased from red to green, respectively. Each spectrum was the average of 5 spectra gotten from 5 different NCs@3-MPBA.

The normalized extinction spectra of the NCs during the different steps of the synthesis are shown in Figure 1A. In black, the overall spectrum of PS beads showed a large scattering background that was characterized by a well-defined band centered at approx. 290 nm and a long tail at longer wavelengths. In red, the NCs before the growing step, revealed that PS beads were correctly dissolved. There was no characteristic localized-surface plasmon resonances (LSPRs) of isolated spherical gold nanoparticles in spectral range because of the small size of gold nanoparticles (2-3 nm). No

evidence of plasmonically interacting nanoparticles at that point. In green, once the growing step was performed, the dominant contribution was shifted to higher wavelengths and broadened, indicating the significant formation of gold nanoparticle agglomerates and plasmon coupling. In blue, no significant change was observed in the extinction spectra when 3-MPBA was adsorbed on the metallic surface. Figure 1B showed the TEM characterization of the nano-scaled NCs with an average diameter of 450 nm, disclosing nanoparticle homogeneity and the porosity of the silica shell that allows the diffusion of small molecules such as H_2O_2. More TEM images of the different synthetic intermediates generated during NCs synthesis showed in Figure SI-1A to SI-1C. DLS confirmed the homogeneity of the NCs in suspension showing an average hydrodynamic size of 467.6 nm (Figure SI-1D) and zeta potential value of -36.7 mV (Figure SI-1E) due to the presence of deprotonated silanol groups in the silica shell. Figure 1C showed the Raman spectrum of 3-MPBA in powder form (black line) and SERS spectrum of 3-MPBA modified NCs (NCs@3-MPBA; red line). The differences between the two spectra are caused by the surface selection rules and the surface enhancement. The formation of Au-S bond, resulting in the deprotonation of the thiol group (-SH), promotes the disappearance of the vibrational mode at 910 cm^{-1} [29]. Moreover, the appearance of the intense SERS features characteristic of the 3-MPBA molecule adsorbed on the inner metallic surface of NCs, such as the bands at 783 cm^{-1} assigned to C-H out of plane bending mode, at 996 cm^{-1} resulting from C-C in plane bending mode, at 1020 cm^{-1} attributed to C-H in plane

bending mode, at 1070 cm^{-1} issued from C-C in plane bending coupled with C-S stretching modes, at 1553 cm^{-1} referred to non-totally symmetric ring stretching mode, and at 1570 cm^{-1} imputed to totally symmetric ring stretching mode, confirmed the successful functionalization of 3-MPBA on the metallic surface of the NCs[13].

Reaction time of NCs@3-MPBA with H_2O_2 was studied in phosphate buffered saline and 30 min was selected as shown in Figure SI-2A. To confirm the H_2O_2 sensing capability of NCs@3-MPBA, we measured the SERS spectra of the NCs@3-MPBA dispersed in different biological-relevant media, saline buffer (pH 7.0, Figure 1D) and cells growth medium (pH 7.2-7.4, Figure SI-2B) containing variable amounts of H_2O_2. On one hand, new prominent bands at 882 and 1589 cm^{-1} emerged which are assigned to the benzene ring stretching (ν_{12}) and the totally symmetric ring stretching (ν_{89}) of 3-MP, respectively. If the H_2O_2 concentration was increased, the SERS intensity of these bands was also increased, consistent with previous studies[13] and with the oxidation of 3-MPBA to 3-MP and the conversion of boronate to hydroxyl functional group. On the other hand, we observed that the band at 1553 cm^{-1} progressively decreased in intensity and almost disappeared when the H_2O_2 concentration is higher that 10^{-3} M. Moreover, the oxidation of 3-MPBA did not change significantly the molecular orientation of the mercaptobenzene group on the gold surface since a large set of different perturbations on the SERS spectra of the mercaptobenzoyl moiety was not observed[30]. We also found that the C-C in plane bending mode (996 cm^{-1}) was no affected by the oxidation of the molecule and therefore, we took it

as a reference band which was insensitive to oxidation. To have an internal calibration to correct signal fluctuation and to minimize the impact of external parameters such as NCs batch-to-batch variability or different cellular loading, we used SERS intensity ratiometric values. Figure SI-2C showed the relations between intensity ratio of 882 cm^{-1} and 996 cm^{-1} (log [I_{882}/I_{996}]) and the concentration of H_2O_2 (log[H_2O_2]) in phosphate buffered saline (black line) and in cell growth media (red line) after suspending NCs@3-MPBA in those two systems. Interestingly, we did not observe a significant difference if the NCs were suspended in phosphate buffer or in growth media, proving the value of our sensor in biological environments.

3.4.2 NCs cell internalization and biocompatibility

Under steady conditions, spatial distribution of intracellular H_2O_2 is not equal[21]. It is critical to verify the location of intracellular NCs with the purpose to analyze local concentration of H_2O_2. Depending on the size and physiochemical properties of nanoparticles, there are different pathways (phagocytosis, micropinocytosis, endocytosis) to determine its location[31]. Endocytosis pathway seems to be the logical approach for our NCs (diameter ~450 nm and SiO_2/gold hybrid material). Figure 2A and 2B showed fluorescent labeling of different cellular organelles and the NCs. The intracellular localization of the NCs by HT29 cells after 24 hours was verified to be within lysosomes. We also demonstrated the lysosomal localization of NCs based on the colocalization of the signal coming

from different dyes and scattering light of NCs shown in Figure SI-3.

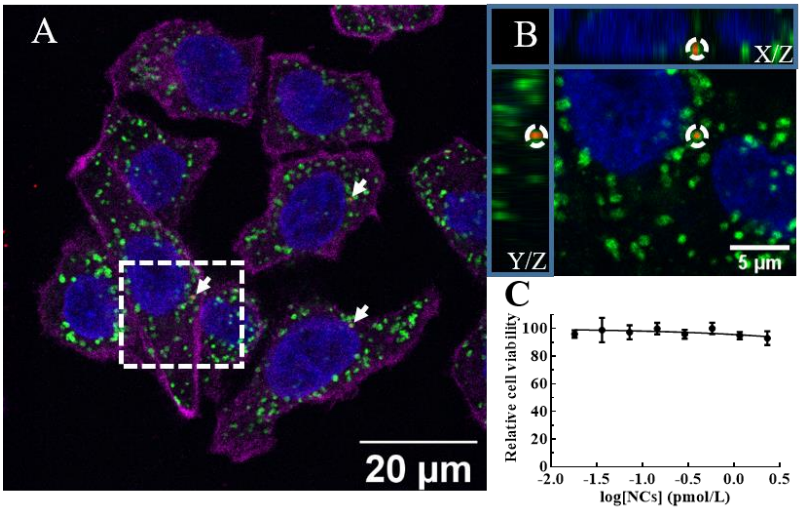

Figure 2: NCs cells internalization and biocompatibility. (A) Cellular uptake of NPs by HT29 cells using CLSM, corresponding to the Z- scan of a cells area. Nucleus: blue; lysosomes: green; PS@SiO_2 NPs: red; and cytoskeleton: magenta. NPs were shown with white arrow and white dash circle. (B) Different planes (X/Y; X/Z; Y/Z) of selected area (dashed square in A). Only NPs, lysosome and nucleus were shown for the sake of better recognition of lysosomal localization. Internalized NPs were localized within lysosomes as observed by the co- localization of the signal intensities of the different dyes and the fluorescence of NPs. (C) Cell viability was determined by Resazurin-Based Assay after the internalization of NCs.

Previous results on these NCs have pointed out a safety profile of the NCs in addition to their excellent SERS capabilities for sensing[27,32]. In this study, we confirm the biocompatibility of the NCs based on an unaltered mitochondrial activity. Colon cancer cells, HT29, were exposed to the NCs with a concentration range from 0.018 to 2.3 pmol/L (by number of NCs; Figure 2C and Figure SI-4). As it can be observed in Figure SI-4, the NCs were plainly visible (dark points) under an inverted optical microscope. At very

high concentrations (≥1.15 pmol/L), the HT29 cells were fully covered by NCs. Under any circumstances, including [NCs] 2.3 pmol/L, no or extremely low cytotoxicity was observed after 24 hours of exposure. IC50 was calculated to be 4000 pmol/L, which is significantly higher than the concentration we used in this work (0.072 pmol/L). These results confirmed no effect of the NCs on the cell viability during the SERS sensing.

3.4.3 Influence of pH on NCs@3-MPBA H_2O_2 sensing

Intracellular pH varies among different compartments. Organelles of endocytic pathways also have different luminal acidity (pH 4.7 to 6.7), while cytosol pH ranges between 7.0 to 7.4, and extracellular pH ranges between 7.3 to 7.4[33]. In order to determine local H_2O_2 concentration in physiological milieu, it is necessary to study the influence of pH in the response of sensor. Figure 3 showed how the SERS intensity ratios I_{882}/I_{996} of NCs@3-MPBA varied at different pHs and H_2O_2 concentrations, ranging from pH 4 to pH 9 and H_2O_2 concentrations from 10^{-2} M to 10^{-8} M. Complete SERS spectra were shown in Figure SI-5. The SERS intensity ratio I_{882}/I_{996} increased along with H_2O_2 concentration increasing. Moreover, I_{882}/I_{996} also increased when the pH became more alkaline under same H_2O_2 concentration. For example, I_{882}/I_{996} at pH 9 and $[H_2O_2] = 10^{-6}$ M was approx. 6 times higher than at pH 4.

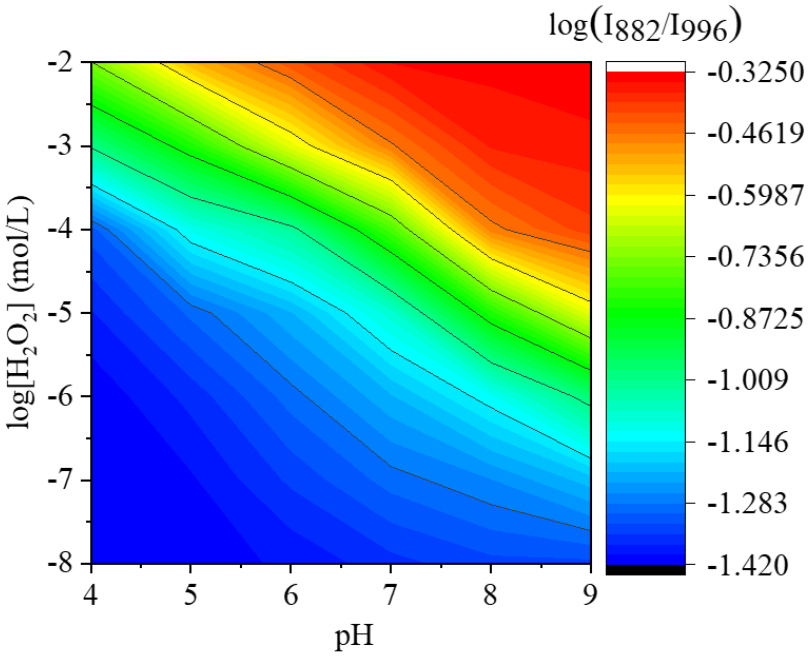

Figure 3: pH effect of 3-MPBA for H_2O_2 sensing based on Intensity ratio of 882 cm^{-1} to 996 cm^{-1}. 3D matrix showed how $\log(I_{882}/I_{996})$ changed with H_2O_2 under different pH. Values were calculated based on SERS spectra of NCs@3-MPBA in suspension in phosphate buffer at different pH and H_2O_2 concentrations, with pH ranging from 4 to 9, and H_2O_2 from 10^{-2} M to 10^{-8} M. Each point was the average of five probes.

An important parameter of 3-MPBA is its pKa value, which is a measure of its Lewis acidity. This value determines the ratio between the trigonal boronic acid and the tetragonal boronate ion (negatively charged) at a specific pH value (Figure SI-6A). In the case of NCs@3-MPBA, the inner gold surface will be fully negatively charged when dispersed in a strongly basic solution because pKa of phenylboronic acid monolayers is reported to be 9.2[34]. These structural changes of the molecule can be observed using SERS spectroscopy. More specifically, the relative SERS

intensity of the 3-MPBA band that is assigned to the non-totally symmetric ring stretching mode (1553 cm^{-1}) varies depending on the environmental pH values, which is a manifestation of charge transfer (CT) processes[35]. Figure SI-6B showed SERS spectra of NCs@3-MPBA dispersed in phosphate buffered saline with pH ranging from 4 to 9. The band at 1553 cm^{-1} decreased in intensity when pH increased. More importantly, pH had relatively low effect on the H_2O_2 sensitive peak at 882 cm^{-1} in the absence of H_2O_2, confirming that the structural change of 3-MPBA in our pH range was not the main reason of pH effect on 3-MPBA responses. 3-MPBA oxidized into 3-MP converting boronate to hydroxyl functional group. This oxidative process produces the rupture of the B-C chemical bond. Comparing with trigonal boronic acid, the complexation with a third hydroxyl group in tetragonal boronate ion facilitates the oxidation to hydroxyl in the presence of H_2O_2, which enhanced this B-C bond cleavage sensitivity and made 3-MPBA oxidation by H_2O_2 base promoted[36]. The equilibrium constants of this oxidation reaction at specific pHs varied which can be estimated using the Henderson-Hasselbach equation using the pKa of the 3-MPBA. Under basic pH, lower amount of H_2O_2 is needed than in acid pH to achieve equivalent SERS readout. With same amount of H_2O_2, since the equilibrium is different for different pHs, the SERS readout will be different, and thus the LODs under different pH are going to be reasonably different. The sensitivity of our sensor NCs@3-MPBA is pH-dependent, being maximum at high pH (9-7) and lowering with decreasing pH (6-4). In general, H_2O_2 measurements are based on direct or indirect oxidation of a

probe by H_2O_2 [10], thus this pH influence on NC@3-MPBA H_2O_2 sensing can be further applied to all H_2O_2 measurements which are based on aromatic boronic acid coupled with fluorescence or SERS.

The LOD of our sensor for H_2O_2 was calculated based on visual definition[37]. We used logarithmic scales for both the horizontal and vertical axes (*i.e.*, log (I_{882}/I_{996}) and log [H_2O_2]), which broaden the linear range to four orders of magnitude (*e.g.*, for pH7 [H_2O_2] from 10^{-2}M to 10^{-6}M), since the linear ranges previous reported were in two orders or less based on numerical scales[13,14,16]. Figure SI-7 showed the different H_2O_2 calibration curves for each pH while table SI-1 showed the pH-dependent LODs of the sensor and corresponding calibration equations. The LOD of H_2O_2 at acid and neutral pH (pH 4 to pH 7) was around 10^{-6} M and close to 10^{-8} M for pH 8 and pH 9.

As a control, we also studied the SERS spectra of 3-MP at different pH values. Interestingly, Figure SI-8 showed that the SERS spectrum of 3-MP was not affected by pH. We did not observe changes (*e.g.*, band shift, intensity ratios, among other) in the vibrational modes of the 3-MP between pH 4 to pH 9. This confirms that pH effect on 3-MPBA responses is not related with 3-MP vibrational differences.

3.4.4 Synthesis of a multiplex sensor to study pH and H_2O_2 interrelation

Considering that pH affects the sensitivity of our NCs@3-MPBA, we added a second Raman probe for pH sensing and studied the interrelation of both parameters. 4-MBA has been previously used

for pH sensing with SERS[38,39], since the ratiometric intensity signal of COO^- stretching vibration mode can be calibrated for pH sensing. The peaks at around 1075 cm^{-1} and 1590 cm^{-1} correspond to aromatic ring vibrations. The peaks at around 1385 cm^{-1} and 1700 cm^{-1} are attributed to symmetric carboxyl stretching mode and C=O stretching vibrations of non-dissociated COOH groups, respectively[39,40].

As shown in Figure SI-9, we collected SERS spectra of 4-MBA modified NCs (NCs@4-MBA) in phosphate buffered saline under pH 4 and pH 7 without H_2O_2 and with H_2O_2 concentration 10^{-2} M. No changes observed in the vibrational modes, confirming that the commonly used pH sensitive peak at around 1385 cm^{-1} [39] can be used for pH sensing even with the presence of H_2O_2.

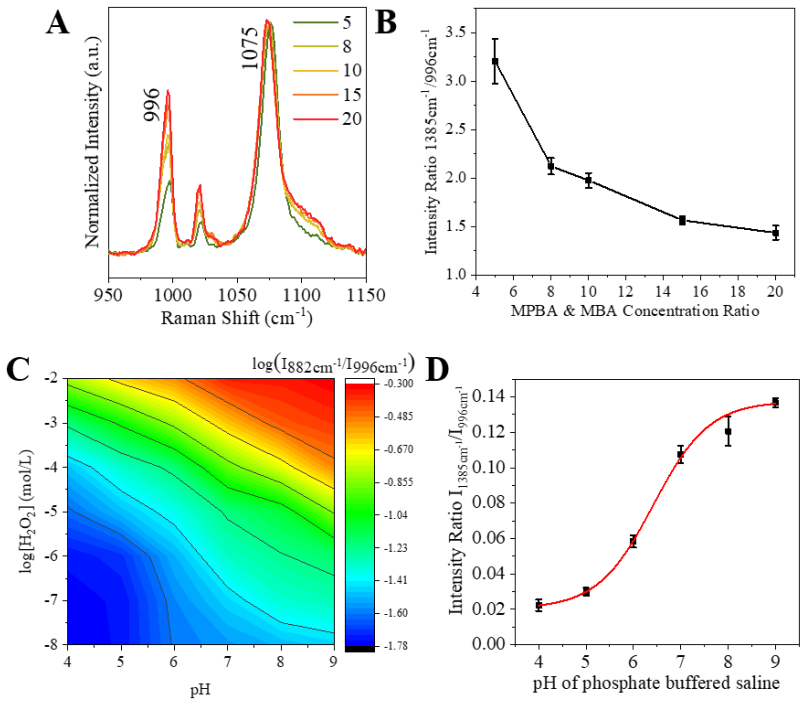

Figure 4: Synthesis of NCs loaded with both Raman probes, 3-MPBA for H_2O_2 and 4-MBA for pH; and calibration curves for H_2O_2 determination. (A) Zoomed SERS spectra of 3-MPBA and 4-MBA modified NCs, with different 3-MPBA and 4-MBA concentration ratios ([3-MPBA]/[4-MBA] =5; 8; 10; 15; 20). Interested bands at 996 cm^{-1} and 1385 cm^{-1} correspond to 3-MPBA and 4-MBA relative occupations on NCs. (B) Intensity ratios between 1385 cm^{-1} and 996 cm^{-1} as a function for 3-MPBA and 4-MBA modification. Error bars represented the standard deviations in five probes. (C) 3D matrix showed how $\log(I_{882}/I_{996})$ changed with H_2O_2 under different pH. Values were calculated based on SERS spectra of NCs@3-MPBA&4-MBA in suspension in saline media at different pH and H_2O_2 concentrations, with pH ranging from 4 to 9, and H_2O_2 from 10^{-2} M to 10^{-8} M. Each point was the average of five probes. (D) Calibration curves of NCs@3-MPBA&4-MBA for pH in phosphate buffer (from 4 to 9). The averages and standard deviations were calculated with all the spectra with H_2O_2 (10^{-2} M, 10^{-3} M, 10^{-4} M, 10^{-5} M, 10^{-6} M, 10^{-7} M, 10^{-8} M) and without H_2O_2 within same pH.

3-MPBA and 4-MBA modified NCs (NCs@3-MPBA&4-MBA) were synthesized following the same procedure as described before. The general approach was to incubate diluted feedstock solution of two modifiers (3-MPBA and 4-MBA) with synthesized NCs in ethanolic solution. The surface composition of modified NCs was monitored by SERS. By simply comparing the strong bands intensities at 996 cm^{-1} and 1075 cm^{-1}, the relative proportions on NCs surface of each modifier can be estimated. The peak around 996 cm^{-1} is attributed to C-C in plane bending mode of 3-MPBA, and the peak around 1075 cm^{-1} attributed to aromatic ring vibrations of 3-MPBA and 4-MBA. We merged the SERS spectra of 3-MPBA and 4-MBA with the ratio 1:1, and calculated the intensity ratio of 1075 cm^{-1} to 996 cm^{-1} (I_{1075}/I_{996}) as shown in Figure SI-10A. When I_{1075}/I_{996} is around 1.55, the signal proportion of those two modifiers will be equivalent. The surface composition is the result of competition for surface site between 4-MBA and 3-MPBA. Thus, we tuned the concentration ratio between 4-MBA and 3-MPBA in

feedstock solutions for multiplex sensor preparation, with the purpose to achieve comparable signals from 4-MBA and 3-MPBA. Figure 4A showed the zoomed SERS spectra of a series of NCs prepared with different 3-MPBA and 4-MBA ratio modifying feedstock solutions, with whole SERS spectra shown in Figure SI-10B. The relative intensities of the marker bands at 1075 cm^{-1} to 996 cm^{-1} changed dramatically. Only 4-MBA bands at 1075 cm^{-1} appeared in the spectra at lower concentration ratio. And 3-MPBA bands could be observed only when the concentration ratio increased. Figure 4B showed the relations of I_{1075}/I_{996} against the ratios of two modifiers. By tuning the ratio from 5 to 20 in feedstock solutions of 3-MPBA and 4-MBA, I_{1075}/I_{996} decreased from 3 to 1.4. The ratio around 15 of 3-MPBA to 4-MBA was selected as working condition, where I_{1075}/I_{996} was around 1.55.

We measured the SERS spectra of NCs@3-MPBA&4-MBA in suspension in saline media at different pH and H_2O_2 concentrations, with pH ranging from 4 to 9, and H_2O_2 from 10^{-2} M to 10^{-8} M. Figure 4C showed the SERS intensity ratios I_{882}/I_{996} of NCs@3-MPBA&4-MBA at different pHs and H_2O_2 concentrations. The signal changes were in agreement with the phenomenon we observed with NCs@3-MPBA: I_{882}/I_{996} increased with both H_2O_2 and pH. Complete spectra showed in Figure SI-11. Bands at around 996 and 1075 cm^{-1} are attributed to aromatic ring vibrations, which are not sensitive to pH neither H_2O_2. Bands at around 1385 cm^{-1} and 1700 cm^{-1} are related to carboxyl group vibrations, and are only sensitive to pH. Intensity at 1385 cm^{-1} increased along with pH increasing, while intensity at 1700 cm^{-1} decreased when pH

increased. Band at 882 cm^{-1}, which corresponding to the benzene ring stretching mode of 3-MPBA, is sensitive to H_2O_2. Its intensity increased along with H_2O_2 increasing. The responsiveness of 3-MPBA and 4-MBA were maintained in the presence of each other when modified onto same NCs. While pH affects the oxidation reaction of 3-MPBA, which will further affect the intensity of 882 cm^{-1}. For pH sensing, we chose the commonly used peak at around 1385 cm^{-1} [39], and intensity ratio of 1385 cm^{-1} to 996 cm^{-1} ($\log(I_{1385}/I_{996})$) was used for pH determination. With known pH, H_2O_2 concentration could be accurately calculated by I_{882}/I_{996} based on calibration curves.

Calibration curves for H_2O_2 determination showed in Figure SI-12 was based on $\log(I_{882}/I_{996})$. The linear ranges for H_2O_2 varied with different pHs since there were different LODs for each pH. Calibration curve functions and the LODs at different pHs were shown in Table SI-2. Although the intensity loss of multiplex sensor at sensitive peak 882 cm^{-1} was calculated around 10% compared with NCs@3-MPBA, the LOD results for H_2O_2 were comparable. Calibration curves for pH measurement based on I_{1385}/I_{996} showed in Figure 4D. NCs@3-MPBA&4-MBA was sensitive to changes in the pH ranging from 5 to 7, presenting typical Henderson–Hasselbalch plots[41], which is in agreement with the SERS results published of 4-MBA covered gold nanoparticles[39].

3.4.5 Intracellular and extracellular H_2O_2 monitoring with NCs@3-MPBA

One of the most common and simply method to understand intracellular H_2O_2 functions is to add H_2O_2 itself directly to experimental system. With permeability coefficients ranging from 0.01 to 0.7 cm/min, H_2O_2 can permeate membrane at relatively rapid speed and establish equilibrium[42]. To demonstrate the feasibility of mimicking cell stress with H_2O_2 incubation, we used one dye to monitoring intracellular H_2O_2 changes. In Figure SI-13A, cells were first transfected with orp1-GFP which is one dye specific for intracellular H_2O_2. After 500 μM H_2O_2 adding into cells growth media, the fluorescence decrease indicated the intracellular H_2O_2 appearance. By calculating integrated density of CLSM images, the intracellular H_2O_2 level went into platform after 10 min treatment as shown in Figure SI-13B.

Cell viability test were established with H_2O_2 concentration from 5 μM to 50 mM, using resazurin for mitochondria activity. Figure SI-14 showed under H_2O_2 treatment, mitochondria activity increased because of H_2O_2 stimulation, thus we were not able to see any toxicity effect. Thus, we changed to trypan blue to check cellular membrane integrity. Under H_2O_2 concentration from 10^{-4} M to 10^{-2} M, after one-hour treatment, Table SI-3 showed that all the integrity results were higher than 90% viability, indicating the feasibility of our treatment.

SERS measurements were performed at a very low NCs concentration (0.072 pmol/L) and single-capsule analysis inside living cells was possible as the nanostructures were plainly visible with Raman microscope. This relatively low working concentration minimized unfocused SERS signals coming from nearby NCs. And

whole NCs illumination was ensured, as the laser spot diameter (1 μm) of our Raman spectrometer was bigger than the NCs diameter. Figure SI-15 showed the intracellular and extracellular NCs@3-MPBA SERS spectra collected with blank HT29 and H_2O_2 treated HT29. By comparing intensity ratio I_{882}/I_{996} of blank cells and H_2O_2 (10 mM, 1 mM and 0.5 mM) treated cells as shown in Figure SI-16, both the intracellular and extracellular H_2O_2 level increased when H_2O_2 concentration added increased, indicating the sensing ability of our sensor. Meanwhile, the intracellular signal was much lower than the extracellular signal. After verified NCs@3-MPBA sensing ability in physiological environment, in order to know the accurate H_2O_2 local concentration, the next step was to use NCs@3-MPBA&4-MBA.

3.4.6 Intracellular and extracellular H_2O_2 and pH monitoring with NCs@3-MPBA&4-MBA

Finally, we validated the performance of our sensors for detecting *in vitro* H_2O_2 and pH. Nanosensors were incubated with cells for 24h for sufficient uptake of NCs through endocytosis process. Bright field images in Figure 5A gotten from Raman equipment indicated that cells morphology was maintained under exposure to NCs and H_2O_2 and/or Bafilonycin A1.

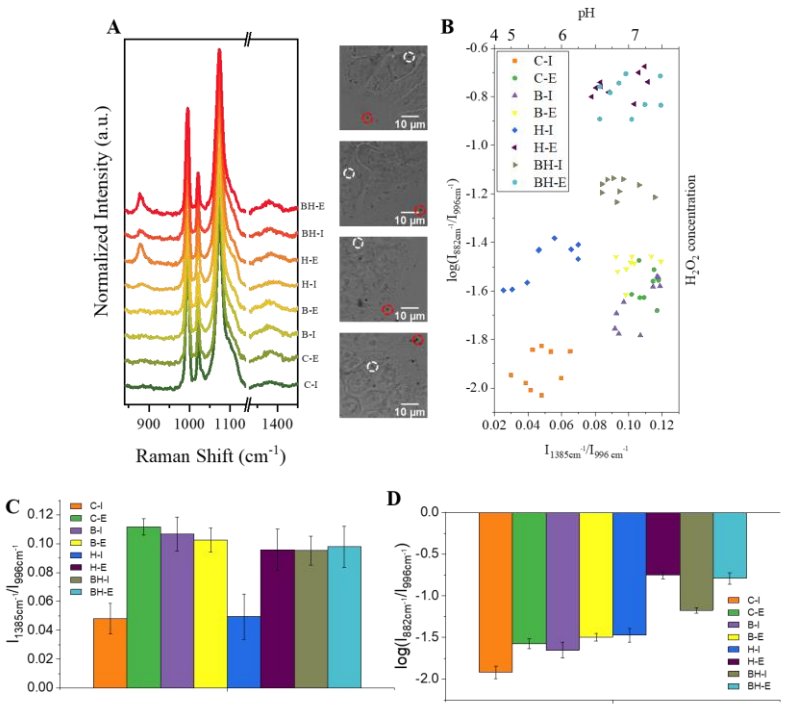

Figure 5: Intracellular and extracellular H_2O_2 and pH SERS determination with NCs@3-MPBA&4-MBA. Intracellular and extracellular SERS spectra were collected with HT29 under different treatments: blank cells, Bafilomycin A1 treated, 1 mM H_2O_2 treated, Bafilomycin A1 and 1 mM H_2O_2 both treated HT29. C-I: intracellular probes of blank HT29; C-E: extracellular probes of blank HT29; B-I: intracellular probes of Bafilomycin A1 treated HT29; B-E: extracellular probes of Bafilomycin A1 treated HT29; H-I: intracellular probes of 1 mM H_2O_2 treated HT29; H-E: extracellular probes of 1 mM H_2O_2 treated HT29; BH-I: intracellular probes of Bafilomycin A1 and 1 mM H_2O_2 treated HT29; BH-E: extracellular probes of Bafilomycin A1 and 1 mM H_2O_2 treated HT29. **(A)** Intracellular and extracellular NCs@3-MPBA&4-MBA SERS spectra of HT29 with different treatments. Optical HT29 images were collected with Raman microscope. White dash circles showed internalized probes, and red dash circles showed extracellular probes, from where SERS signals were collected. **(B)** Intensity ratio between 1385 cm^{-1} and 996 cm^{-1} (I_{1385}/I_{996}) and intensity ratio between 882 cm^{-1} and 996 cm^{-1} ($\log(I_{882}/I_{996})$) were calculated and shown of all the spectra gotten with HT29 under different treatments. I_{1385}/I_{996} reflected local pH value, and $\log(I_{882}/I_{996})$ corresponds to local H_2O_2 concentration. **(C)** I_{1385}/I_{996}, for local pH determination, were calculated of intracellular and extracellular probes with HT29 under different treatment. Each column was the average of 10 different probes. **(D)** $\log(I_{882}/I_{996})$, for local H_2O_2 detection, were calculated of intracellular and extracellular probes with HT29 under different treatment. Each column was the average of 10 different probes.

SERS spectra of extracellular and intracellular NCs@3-MPBA&4-MBA of blank cells were first collected from 10 different NCs separately as showed in Figure 5A (C-I and C-E). Figure 5B showed the distribution of I_{1385}/I_{996} and $\log(I_{882}/I_{996})$ obtained from spectra which corresponding to pH value and H_2O_2 concentration, respectively. And in Figure 5C and Figure 5D showed the average value and standard deviation of I_{1385}/I_{996} and $\log(I_{882}/I_{996})$ separately. The intensity ratios I_{1385}/I_{996} of those 10 spectra of extracellular NCs were around 0.1, according to pH calibration curve, pH there were around 7 which agreed with the cells growth media pH. While intracellular NCs we collected here indicated local pH ranging from 5 to close 7. The intensity ratio $\log(I_{882}/I_{996})$ for extracellular NCs had values around -2, implying the H_2O_2 concentration in cell growth media were lower than 0.8 μM. The intracellular signal was around our negative control signal, which means the physiological lysosomal H_2O_2 above our limit, since our NCs has LOD at lysosomal acidic pH (pH 5) was around 10^{-6} M.

Then we mimic cellular stress by increasing the amount of H_2O_2 exposed to the cells. We used 1 mM H_2O_2 to study intracellular and extracellular H_2O_2 concentration changes as showed in Figure 5 (H-I and H-E). Compared with the calibration curve, extracellular pH maintained the pH of growth media which was around 7, while intracellular pH ranged from 5 to 6. Interestingly, we found that, after the one-shot addition of H_2O_2 to cells growth media, the extracellular H_2O_2 concentration was not the same with the addition concentration. Since we already demonstrated that proteins in our

growth media had no or extremely low effect on H_2O_2 sensing, the rapid removal of extracellular H_2O_2 was because of the active cellular metabolism[24]. The gradient would be around 5 to 10 times extracellular concentration lower than the addition concentration depending on the metabolism of cells. Moreover, intracellular H_2O_2 concentration was around 40 times lower than extracellular concentration.

Bafilomycin A1 is one commonly used agent modifying lysosomal acidification[43]. The vacuolar ATPase (V-ATPase) is a proton pump hydrolysing ATP, controlling the acidification of endosomes and lysosomes. Bafilomycin A1 could inhibit the activity of the V-ATPase. Thus lysosomal pH increase upon the addition of Bafilomycin A1[44]. We also checked the ability in our cell line by using lysotracker as a fluorescence pH indicator shown in Figure SI-17. With Bafilomycin A1 500 nM treated after 2 hours, there was no signals coming from lysotracker, which meant the lysosomal pH was neutral or even basic. We verified the accurate pH with our NCs, shown in Figure 5 (B-I and B-E). Extracellular pH had almost no changes with Bafilomycin A1 treatment compared with blank cells. Intensity ratio I_{1385}/I_{996} from intracellular NCs indicated that intracellular pH was around pH 7. By continuously adding H_2O_2 to Bafilomycin A1 treated cells (Figure 5 BH-I and BH-E), we further proved again pH effect on 3-MPBA H_2O_2 sensing ability. With 1 mM H_2O_2 treatment, intracellular intensity ratio $\log(I_{882}/I_{996})$ gotten from bafilomycin treated HT29 are higher than bafilomycin non-treated HT29. By comparing the H_2O_2 calibration curves, we found

we had consistent H_2O_2 concentration, and this higher signal with Bafilomycin A1 treatment was because of the pH changes.

We continuously used more H_2O_2 concentration (10 mM and 0.5 mM) and further verified again our conclusions. Intracellular and extracellular spectra of NCs@3-MPBA&4-MBA with HT29 under different treatments: Bafilomycin A1 treated and non-treated HT29 with different amount of H_2O_2 addition (10 mM and 0.5 mM) and without H_2O_2 addition were collected and $\log(I_{882}/I_{996})$ and I_{1385}/I_{996} values were summarized in Figure SI-18. While the pH and H_2O_2 values of each NCs were calculated based on pH and H_2O_2 calibration curves and shown in Table SI-4. The complete spectra showed in Figure SI-19. Interestingly, we found that even intracellular NCs located in different lysosomes or endosomes which were during endocytic pathway, even within different pHs, environmental H_2O_2 were consistent under same treatment.

We need to report the effect of irradiation on the stability of this sensor. As shown in Figure SI-20, NCs@3-MPBA&4-MBA were suspended into pH 9 phosphate buffered saline without H_2O_2, with 3-MPBA $5X10^{-3}$M and 4-MBA 10^{-3}M for the modification. We got different spectra under different irradiation time (5s and 20s) with laser power 5 mW on same particle. The intensities of peaks at 1385 cm^{-1} and 1590 cm^{-1}, corresponding to symmetric carboxyl stretching mode and aromatic ring vibrations of 4-MBA, decreased under high irradiation time, indicating that we were losing 4-MBA under high irradiation time. It seems 4-MBA is more sensitive to energy than 3-MPBA. Controlling equal irradiation is critical for multiplex measurements.

3.5 CONCLUSION

We synthesized a complex nanocapsule composed of plasmonic gold nanoparticles placed on the inner surface of silica shell. NCs anchored ensembles of interparticle hot spots in their internal surface and silica shell preventing physicochemical interaction between the gold nanoparticles and the big biomolecules from biological media, which were designed for biological SERS application. Since NCs were colocalized within lysosomes with luminal acidic pH, pH effect on 3-MPBA modified NCs sensing H_2O_2 was studied. The complexation of boronic acid with three hydroxyl groups in alkaline pH environment enhanced this B-C bond cleavage sensitivity, which made 3-MPBA oxidation by H_2O_2 base promoted. This pH influence can be further applied to all H_2O_2 measurements which are based on aromatic boronates oxidation coupled with fluorescence or SERS. 3-MPBA and 4-MBA modified NCs were synthesized as H_2O_2 and pH multiplex sensor. The ratio 15 times between 3-MPBA to 4-MBA in feedstock solution was chosen for the synthesis of 3-MPBA and 4-MBA modified NCs, as 4-MBA has higher cross section than 3-MPBA. Different calibration curves were obtained under physiologic pH range. We validated the performance of our sensors for detecting *in vitro* H_2O_2 and pH with H_2O_2 and/or Bafilomycin A1 treated HT29. The intracellular and extracellular H_2O_2 concentration were not affected with Bafilomycin A1 treated HT29. Intracellular H_2O_2 concentration in different organelles of endocytic pathways (lysosomes and endosomes) were equivalent. The intracellular H_2O_2 concentration were approx. 40 times less than extracellular H_2O_2

concentration, and the extracellular H_2O_2 concentration were around 5 to 10 times less than the addition concentration (with one shot addition) because of the metabolism of HT29. A reliable multiplex sensor for local H_2O_2 and pH analysis within single cell was reported.

3.6 REFERENCES

1. Laing, S., Gracie, K. & Faulds, K. Multiplex *in vitro* detection using SERS. *Chem. Soc. Rev.* **45**, 1901–1918 (2016).

2. Rodriguez-Lorenzo, L., Fabris, L. & Alvarez-Puebla, R. A. Multiplex optical sensing with surface-enhanced Raman scattering: A critical review. *Anal. Chim. Acta* **745**, 10–23 (2012).

3. Dumont, M. & Beal, M. F. Neuroprotective strategies involving ROS in Alzheimer disease. *Free Radic. Biol. Med.* **51**, 1014–1026 (2011).

4. Ishikawa, K. *et al.* ROS-Generating Mitochondrial DNA Mutations Can Regulate Tumor Cell Metastasis. *Science* **320**, 662–664 (2008).

5. Trachootham, D., Alexandre, J. & Huang, P. Targeting cancer cells by ROS-mediated mechanisms: A radical therapeutic approach? *Nat. Rev. Drug Discov.* **8**, 579–591 (2009).

6. Haigis, M. C. & Yankner, B. A. The Aging Stress Response.

Mol. Cell **40**, 333–344 (2010).

7. Cordeiro, J. V. & Jacinto, A. The role of transcription-independent damage signals in the initiation of epithelial wound healing. *Nat. Rev. Mol. Cell Biol.* **14**, 249–262 (2013).

8. Sies, H. Hydrogen peroxide as a central redox signaling molecule in physiological oxidative stress: Oxidative eustress. *Redox Biol.* **11**, 613–619 (2017).

9. Brewer, T. F., Garcia, F. J., Onak, C. S., Carroll, K. S. & Chang, C. J. Chemical approaches to discovery and study of sources and targets of hydrogen peroxide redox signaling through NADPH oxidase proteins. *Annu. Rev. Biochem.* **84**, 765–790 (2015).

10. Rezende, F., Brandes, R. P. & Schröder, K. Detection of hydrogen peroxide with fluorescent dyes. *Antioxidants Redox Signal.* **29**, 585–602 (2018).

11. Belousov, V. V. *et al.* Genetically encoded fluorescent indicator for intracellular hydrogen peroxide. *Nat. Methods* **3**, 281–286 (2006).

12. Gutscher, M. *et al.* Proximity-based protein thiol oxidation by H_2O_2-scavenging peroxidases. *J. Biol. Chem.* **284**, 31532–31540 (2009).

13. Gu, X., Wang, H., Schultz, Z. D. & Camden, J. P. Sensing Glucose in Urine and Serum and Hydrogen Peroxide in Living Cells by Use of a Novel Boronate Nanoprobe Based on Surface-Enhanced Raman Spectroscopy. *Anal. Chem.* **88**,

7191-7197 (2016).

14. Li, X., Duan, X., Yang, P., Li, L. & Tang, B. Accurate *in situ* monitoring of mitochondrial H_2O_2 by robust SERS nanoprobes with a Au−Se interface. *Anal. Chem.* **93**, 4059–4065 (2021).

15. Li, Q. *et al.* Dual Ratiometric SERS and Photoacoustic Core–Satellite Nanoprobe for Quantitatively Visualizing Hydrogen Peroxide in Inflammation and Cancer. *Angew. Chemie - Int. Ed.* **60**, 7323–7332 (2021).

16. Zhang, C., Liu, X., Xu, Z. & Liu, D. Multichannel Stimulus-Responsive Nanoprobes for H_2O_2 Sensing in Diverse Biological Milieus. *Anal. Chem.* **92**, 12639–12646 (2020).

17. Hu, B. *et al.* Avoiding Thiol Compound Interference: A Nanoplatform Based on High-Fidelity Au-Se Bonds for Biological Applications. *Angew. Chemie* **130**, 5404–5407 (2018).

18. Schlücker, S. Surface-enhanced raman spectroscopy: Concepts and chemical applications. *Angew. Chemie - Int. Ed.* **53**, 4756–4795 (2014).

19. Reja, S. I. *et al.* A lysosome targetable fluorescent probe for endogenous imaging of hydrogen peroxide in living cells. *Chem. Commun.* **53**, 3701–3704 (2017).

20. Kim, D., Kim, G., Nam, S. J., Yin, J. & Yoon, J. Visualization of endogenous and exogenous hydrogen peroxide using a lysosome-targetable fluorescent probe. *Sci.*

Rep. **5**, 8488 (2015).

21. Morgan, B. *et al.* Real-time monitoring of basal H_2O_2 levels with peroxiredoxin-based probes. *Nat. Chem. Biol.* **12**, 437–443 (2016).

22. Antunes, F. & Cadenas, E. Estimation of H_2O_2 gradients across biomembranes. *FEBS Lett.* **475**, 121–126 (2000).

23. Huang, B. K. & Sikes, H. D. Quantifying intracellular hydrogen peroxide perturbations in terms of concentration. *Redox Biol.* **2**, 955–962 (2014).

24. Altıntaş, A. *et al.* High-resolution kinetics and modeling of hydrogen peroxide degradation in live cells. *Free Radic. Biol. Med.* **101**, 143–153 (2016).

25. Sousa-Lopes, A., Antunes, F., Cyrne, L. & Marinho, H. S. Decreased cellular permeability to H 2O 2 protects Saccharomyces cerevisiae cells in stationary phase against oxidative stress. *FEBS Lett.* **578**, 152–156 (2004).

26. Yun, D. S., Lee, H. S., Jang, H. G. & Yoo, J. W. Controlling size and distribution for nano-sized polystyrene spheres. *Bull. Korean Chem. Soc.* **31**, 1345–1348 (2010).

27. Sanles-Sobrido, M. *et al.* Design of SERS-Encoded, Submicron, Hollow Particles Through Confined Growth of Encapsulated Metal Nanoparticles. *J. Am. Chem. Soc.* **131**, 2699–2705 (2009).

28. Eilers, P. H. C. & Boelens, H. F. M. Baseline Correction with Asymmetric Least Squares Smoothing. *Leiden University*

Medical Centre Report. (2005).

29. Lee, H. M., Kim, M. S. & Kim, K. Surface-enhanced Raman scattering of ortho- and para-mercaptophenols in silver sol. *Vib. Spectrosc.* **6**, 205–214 (1994).

30. Pazos, E. *et al.* Surface-Enhanced Raman Scattering Surface Selection Rules for the Proteomic Liquid Biopsy in Real Samples: Efficient Detection of the Oncoprotein c-MYC. *J. Am. Chem. Soc.* **138**, 14206–14209 (2016).

31. Kastl, L. *et al.* Multiple internalization pathways of polyelectrolyte multilayer capsules into mammalian cells. *ACS Nano* **7**, 6605–6618 (2013).

32. Rivera_gil, P. *et al.* Plasmonic nanoprobes for real-time optical monitoring of nitric oxide inside living cells. *Angew. Chemie - Int. Ed.* **125**, 13939–13943 (2013).

33. Casey, J. R., Grinstein, S. & Orlowski, J. Sensors and regulators of intracellular pH. *Nat. Rev. Mol. Cell Biol.* **11**, 50–61 (2010).

34. Takahashi, S. & Anzai, J. I. Phenylboronic acid monolayer-modified electrodes sensitive to sugars. *Langmuir* **21**, 5102–5107 (2005).

35. Osawa, M., Matsuda, N., Yoshii, K. & Uchida, I. Charge transfer resonance Raman process in surface-enhanced Raman scattering from p-aminothiophenol adsorbed on silver: Herzberg-Teller contribution. *J. Phys. Chem.* **98**, 12702–12707 (1994).

36. Barriet, D., Yam, C. M., Shmakova, O. E., Jamison, A. C. & Lee, T. R. 4-mercaptophenylboronic acid SAMs on gold: Comparison with SAMs derived from thiophenol, 4-mercaptophenol, and 4-mercaptobenzoic acid. *Langmuir* **23**, 8866–8875 (2007).

37. Şengül, Ü. Comparing determination methods of detection and quantification limits for aflatoxin analysis in hazelnut. *J. Food Drug Anal.* **24**, 56–62 (2016).

38. García-Algar, M. *et al.* Subcellular Optical pH Nanoscale Sensor. *Chem. Select* **2**, 8115–8121 (2017).

39. Kneipp, J., Kneipp, H., Wittig, B. & Kneipp, K. One-and Two-Photon Excited Optical pH Probing for Cells Using Surface-Enhanced Raman and Hyper-Raman Nanosensors. *Nano Lett.* **7**, 2819-2823 (2007).

40. Michota, A. & Bukowska, J. Surface-enhanced Raman scattering (SERS) of 4-mercaptobenzoic acid on silver and gold substrates. *J. Raman Spectrosc.* **34**, 21–25 (2003).

41. Radić, N. & Prkic, A. Historical remarks on the Henderson-Hasselbalch equation: Its advantages and limitations and a novel approach for exact pH calculation in buffer region. *Rev. Anal. Chem.* **31**, 93–98 (2012).

42. Stonr, J. R. & Yang, S. Hydrogen Peroxide: A Signaling Messenger. *Antioxid. Redox Signal.* **8**, 243–270 (2006).

43. Rivera-Gil, P., Nazarenus, M., Ashraf, S. & Parak, W. J. pH-sensitive capsules as intracellular optical reporters for

monitoring lysosomal pH changes upon stimulation. *Small* **8**, 943–948 (2012).

44. Yoshimori, T., Yamamoto, A., Moriyama, Y., Futai, M. & Tashiro, Y. Bafilomycin A1, a specific inhibitor of vacuolar-type H+-ATPase, inhibits acidification and protein degradation in lysosomes of cultured cells. *J. Biol. Chem.* **266**, 17707–17712 (1991).

3.7 SUPPORTING INFORMATION

3.7.1 Section 1: Synthesis and characterization of 3-MPBA modified NCs

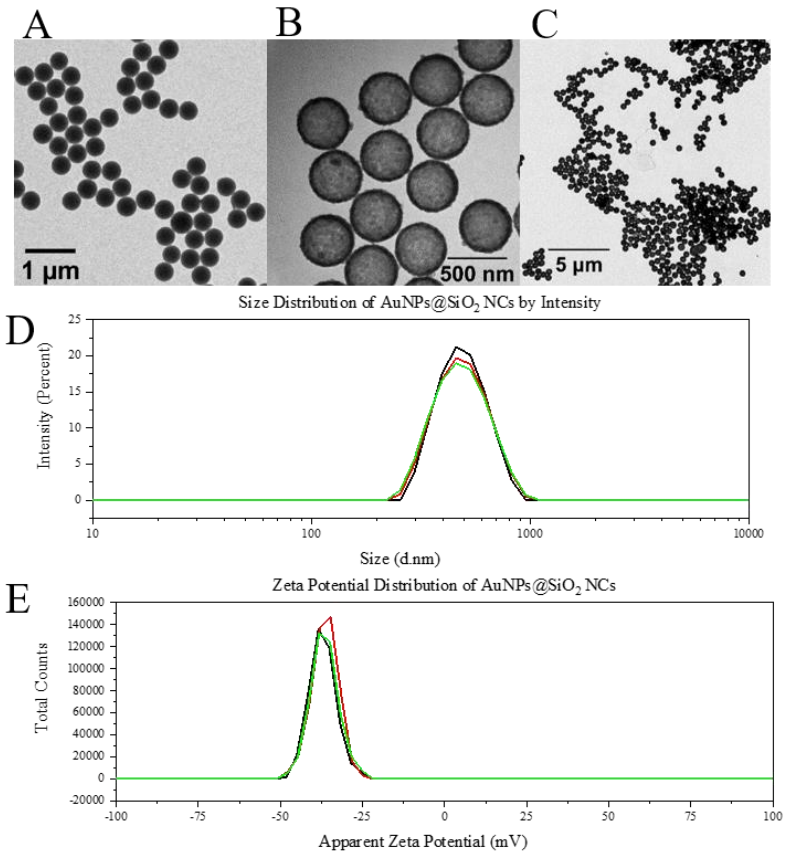

Figure SI-1: Characterization of NCs. (A) TEM image of PS beads after LBL with PSS and PAH; (B) TEM image of Au seeds@SiO_2 NCs; (C) TEM image of NCs; (D) Size measurements (3 repeated runs) of NCs, with mean value 467.6 nm and PDI 0.044; (E) Zeta potential measurements (3 repeated measurements) of NCs, with mean value -36.7 mV.

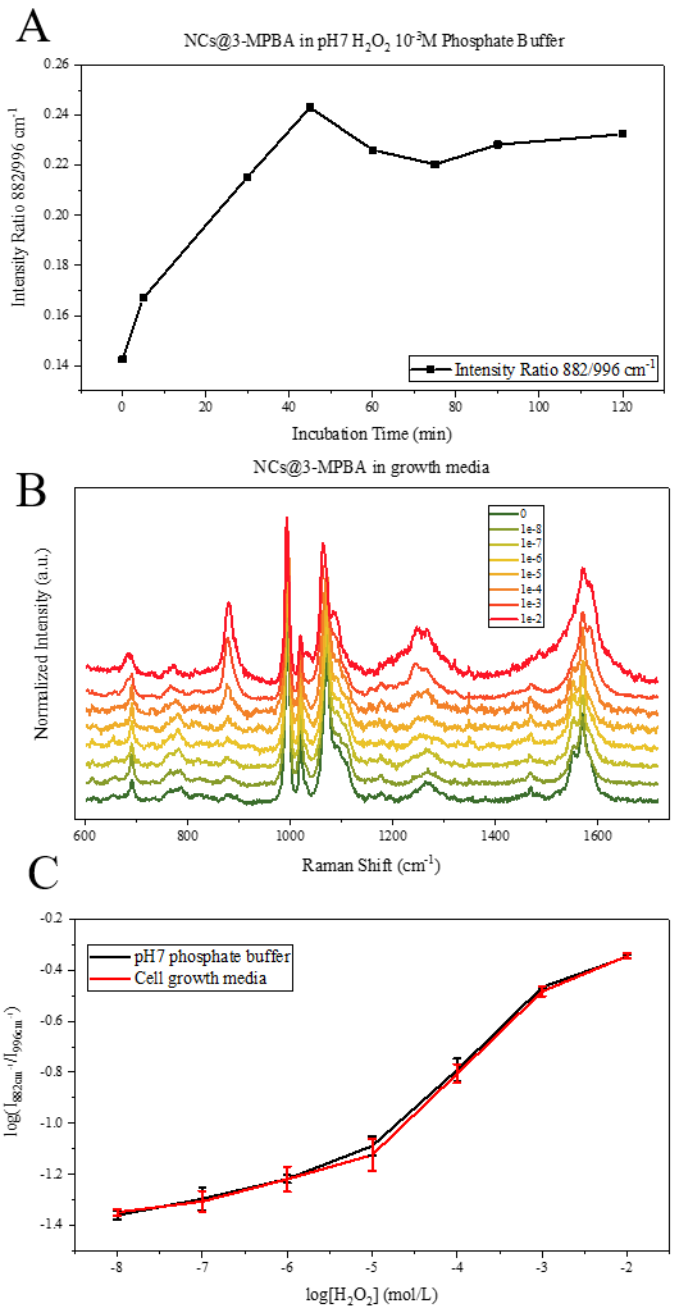

Figure SI-2: 3-MPBA sensing H_2O_2 in cells growth media and calibration curves gotten in phosphate buffer and cells growth media. (A) Kinetic study based on the intensity ratio of 882 cm^{-1} to 996 cm^{-1} by measuring NCs solution mixed with 10^{-3} M H_2O_2 in pH7 phosphate buffered saline; (B) NCs@3-MPBA dispersed in cells growth media with different H_2O_2 concentrations (10^{-2} M, 10^{-3} M, 10^{-4} M, 10^{-}

^{5} M, 10^{-6} M, 10^{-7} M, 10^{-8} M) and without H_2O_2 (from red to green). Each spectrum was the average of 5 spectra gotten from 5 different NCs@3-MPBA; (C) Calibration curves of NCs@3-MPBA determining H_2O_2 in phosphate buffer and in cells growth media followed the same trend, indicating that calibration curves gotten in buffer system can be easily used in growth media environment.

3.7.2 Section 2: NCs cell internalization and biocompatibility

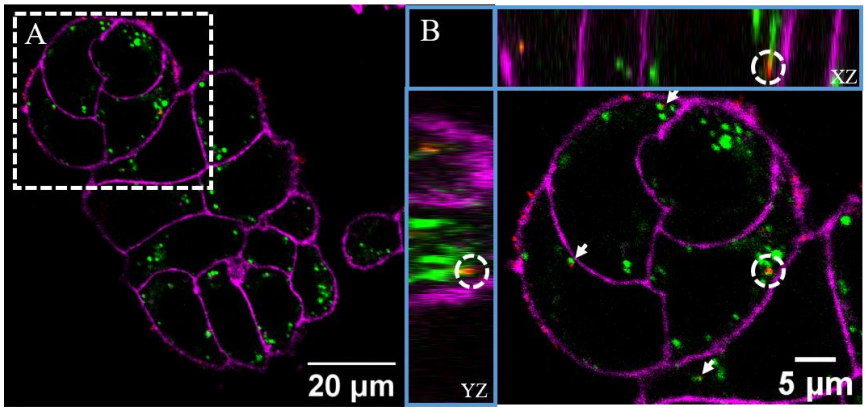

Figure SI-3: Cellular uptake of NCs by HT29 cells using confocal laser scanning microscopy (CLSM). (A) Z- scan of a cells area. NCs were shown with white arrow and white dash circle. (B) Different planes (X/Y; X/Z; Y/Z) of selected area (dashed square in A). Internalized NCs were localized within lysosomes as observed by the co- localization of the signal intensities of the different dyes and the reflected light of the sensor. Lysosomes: green; NCs: red; and cells membrane: magenta.

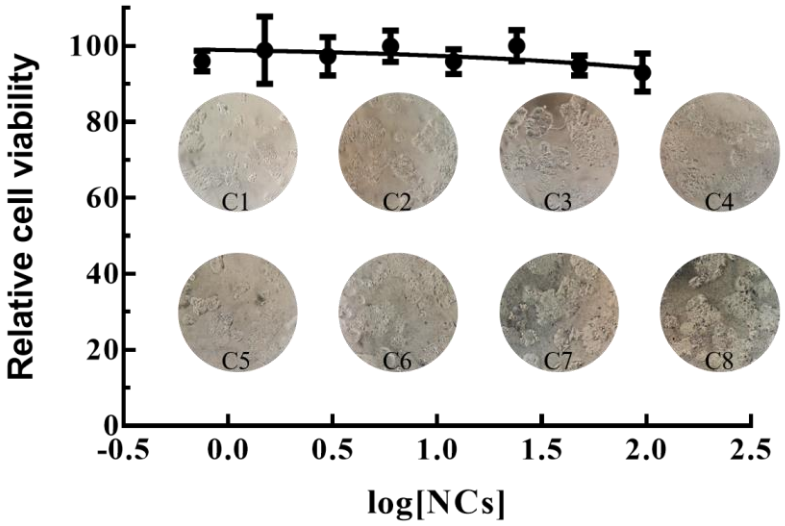

Figure SI-4: Cytotoxicity assay of NCs in HT29 cells. Cell viability was determined by Resazurin-Based Assay after the internalization of NCs. The concentrations of NCs were calculated by number. Optical images were collected with OLYMPUS CKX41 inverted microscope. NCs concentration increased from C1 to C8. Since C7 (NCs concentration higher than 1.15 pmol/L), the HT29 cells were fully covered by NCs.

3.7.3 Section 3: Influence of pH on NCs@3-MPBA H_2O_2 sensing

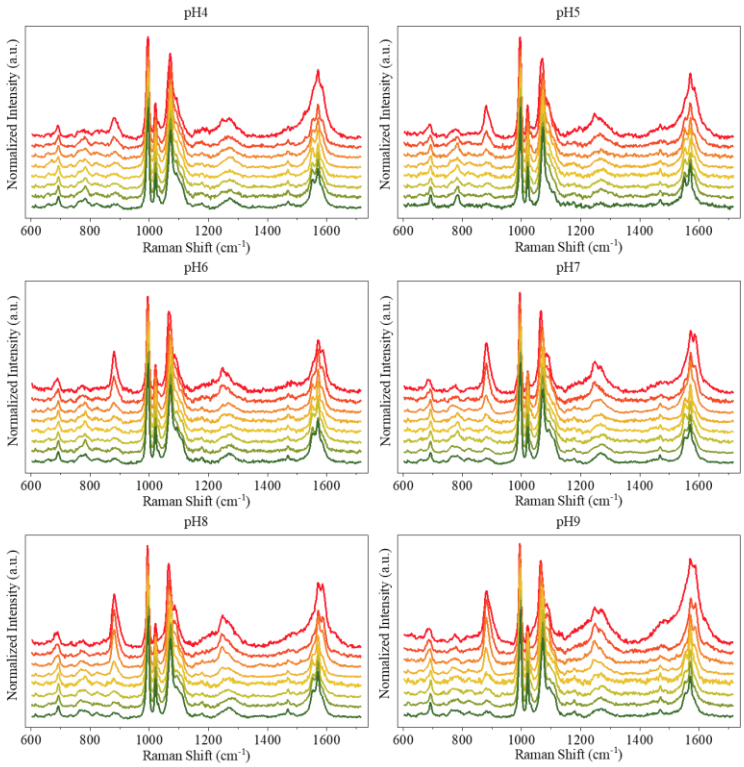

Figure SI-5: SERS spectra of NCs@3-MPBA in phosphate buffer at different pH and H_2O_2 concentrations, with pH ranging from 4 to 9, and H_2O_2 from 10^{-2} M to 10^{-8} M and without H_2O_2 (from red to green H_2O_2 concentration 10^{-2} M, 10^{-3} M, 10^{-4} M, 10^{-5} M, 10^{-6} M, 10^{-7} M, 10^{-8} M, and without H_2O_2), showing how the intensity at 882 cm^{-1} decreased from red to green, respectively. Each spectrum was the average of 5 spectra gotten from 5 different NCs@3-MPBA.

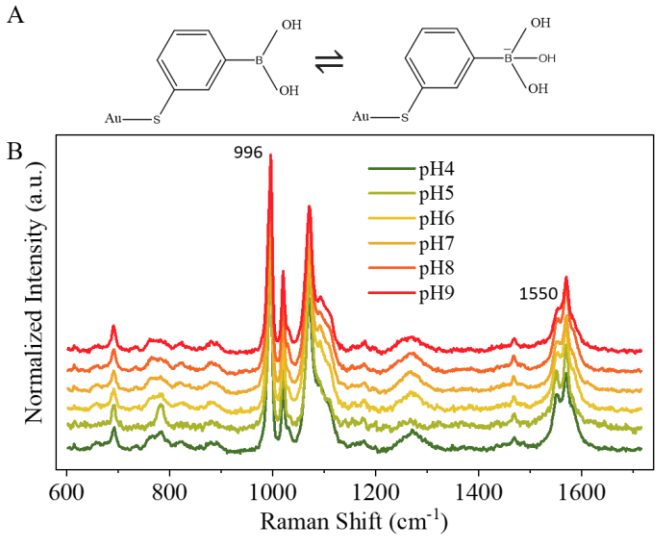

Figure SI-6: NCs@3-MPBA dispersed in different pH buffer without H_2O_2. (A) Scheme of 3-MPBA format in acidic pH (phenylboronic acid) and alkaline pH (boronate acid); (B) SERS spectra of NCs@3-MPBA dispersed in phosphate buffer with pH ranging from 4 to 9, showing that intensity at 1550 cm^{-1} decreased with pH increasing. Each spectrum was the average of 5 spectra gotten from 5 different NCs@3-MPBA.

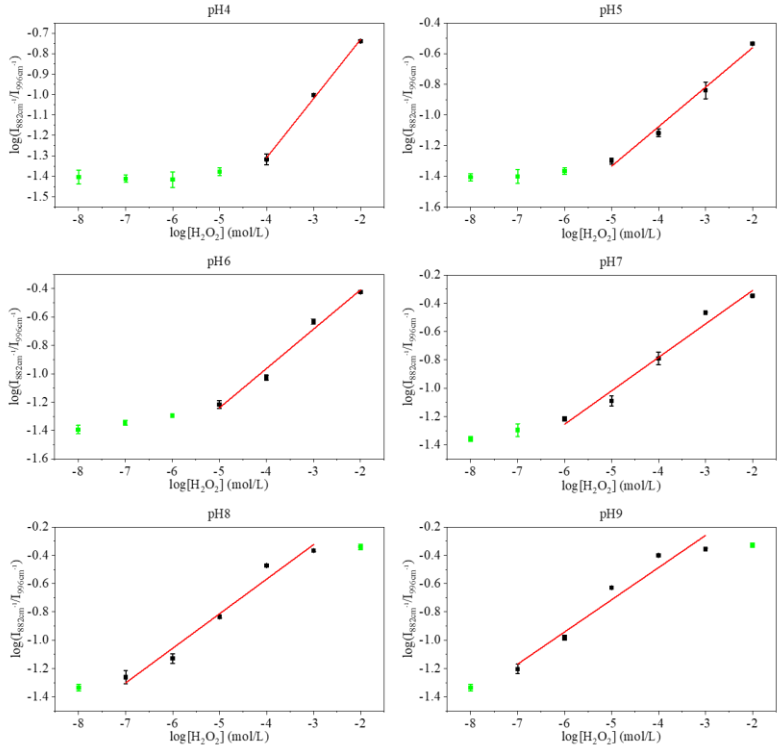

Figure SI-7: Calibration curves and linear ranges of NCs@3-MPBA sensing H_2O_2 under different pH (from 4 to 9). Green dots were masked. Error bars represented the standard deviations of five probes.

pH	Linear fitting: $\log(I_{882}/I_{996}) = a + b*\log[H_2O_2]$				
	Linear range (mol/L)	a-intercept	b-slope	R^2	LOD
4	10^{-2} to 10^{-4}	-0.151	0.289	0.997	57 µM
5	10^{-2} to 10^{-5}	-0.046	0.258	0.988	9.5 µM
6	10^{-2} to 10^{-5}	0.146	0.277	0.980	4.6 µM
7	10^{-2} to 10^{-6}	0.163	0.236	0.975	0.76 µM
8	10^{-3} to 10^{-7}	0.409	0.244	0.970	93 nM
9	10^{-3} to 10^{-7}	0.423	0.227	0.951	39 nM

Table SI-1: Calibration curves equations and LODs of NCs@3-MPBA for H_2O_2 in phosphate buffer with pH ranging from 4 to 9.

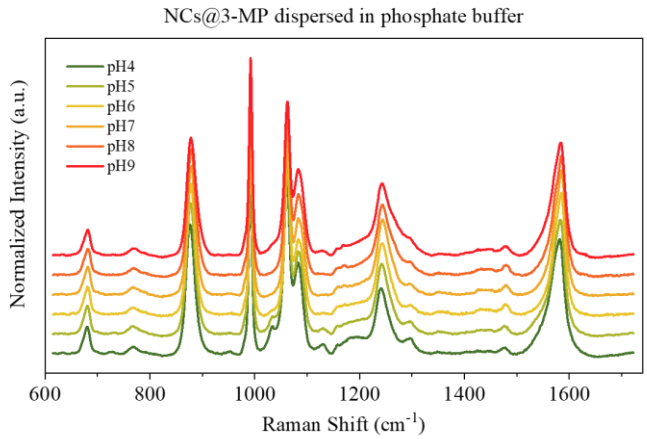

Figure SI-8: SERS spectra of NCs@3-MP dispersed in different pH phosphate buffer from pH 4 to 9.

3.7.4 Section 4: Synthesis of 3-MPBA and 4-MBA modified NCs and detection of H_2O_2 and pH in phosphate buffered saline

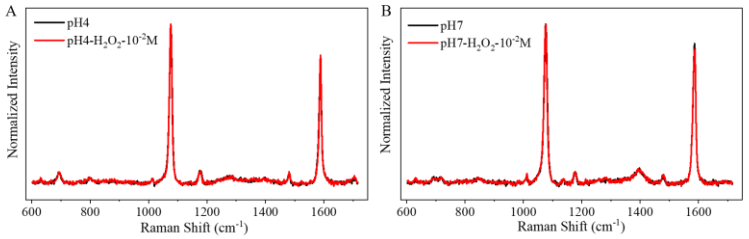

Figure SI-9: SERS spectra of NCs@4-MBA dispersed in buffer with and without H_2O_2. (A) SERS spectra of NCs@4-MBA in pH 4 buffer without H_2O_2 (black line) and with 10^{-2} M H_2O_2 (red line, incubated after 2 hours); (B) SERS spectra of NCs@4-MBA in pH 7 buffer without H_2O_2 (black line) and with 10^{-2} M H_2O_2 (red line, incubated after 2 hours).

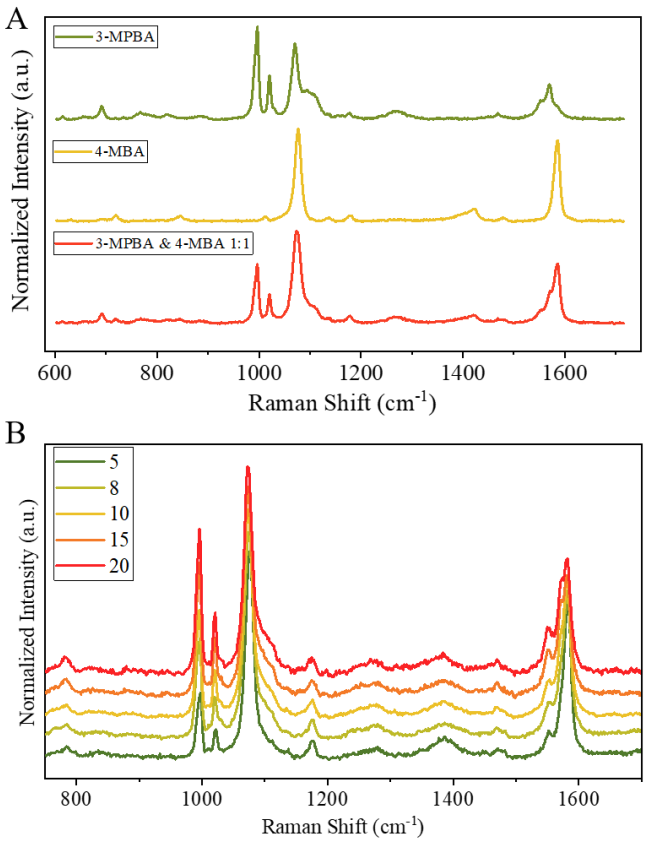

Figure SI-10: Synthesis of 3-MPBA and 4-MBA modified NCs. (A) merged spectra with 3-MPBA and 4-MBA one by one to mimic NCs@3-MPBA&4-MBA with both ligands equivalent modification onto NCs; (B) SERS spectra of 3-MPBA and 4-MBA modified NCs, with different 3-MPBA and 4-MBA concentration ratios ([3-MPBA]/[4-MBA] =5; 8; 10; 15; 20). Each spectrum was the average of 5 spectra gotten from 5 different NCs@3-MPBA&4-MBA.

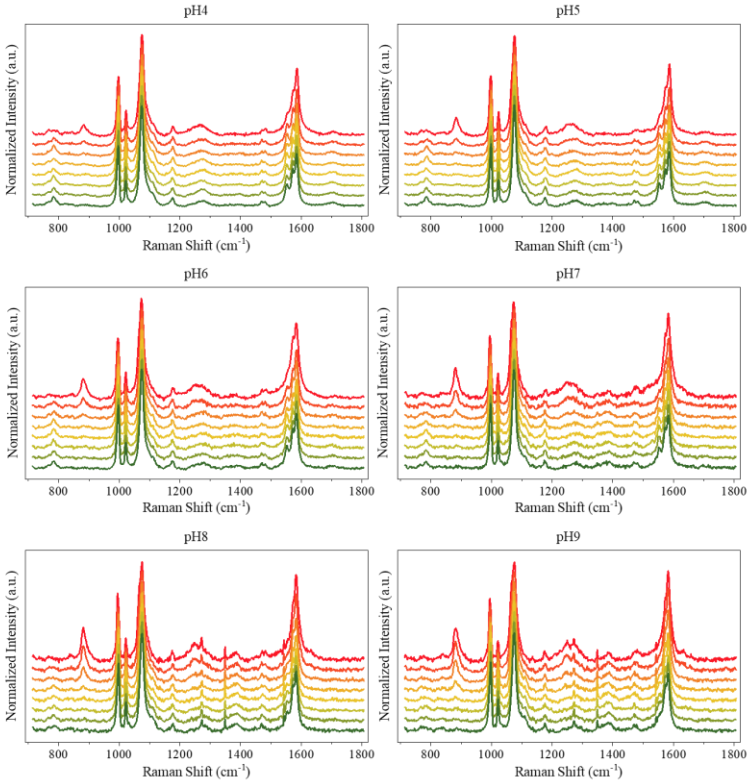

Figure SI-11: SERS spectra of NCs@3-MPBA&4-MBA in phosphate buffer at different pH and H_2O_2 concentrations, with pH ranging from 4 to 9, and H_2O_2 from 10^{-2} M to 10^{-8} M and without H_2O_2 (from red to green, H_2O_2 concentration 10^{-2} M, 10^{-3} M, 10^{-4} M, 10^{-5} M, 10^{-6} M, 10^{-7} M, 10^{-8} M, and without H_2O_2), showing how the intensity at 882 cm^{-1} decreased from red to green and the intensity at 1385 cm^{-1} varied along with pH. Each spectrum was the average of 5 spectra gotten from 5 different NCs@3-MPBA&4-MBA.

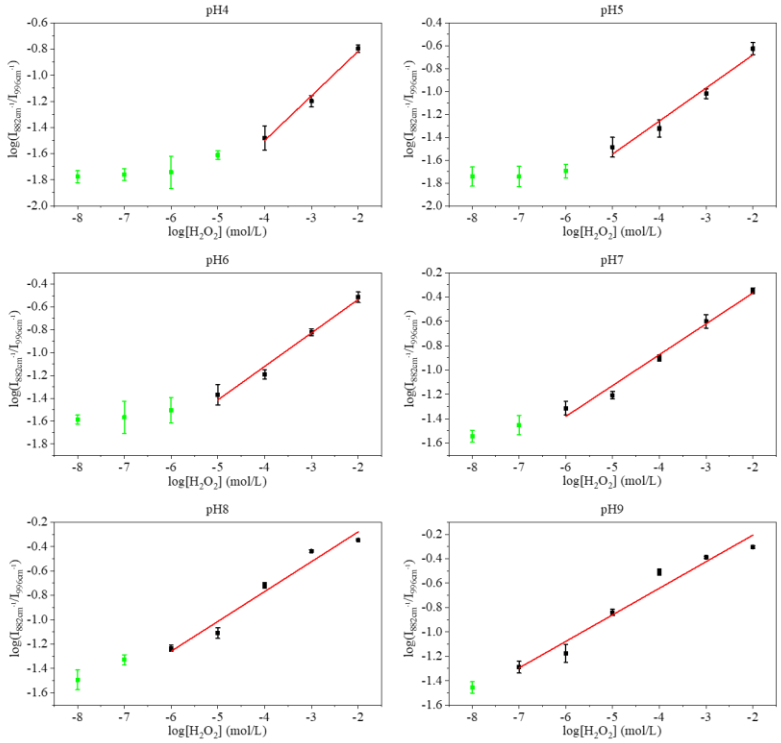

Figure SI-12: Calibration curves of NCs@3-MPBA&4-MBA for H_2O_2 in phosphate buffer with pH ranging from 4 to 9. Red lines are linear fitting results. Green dots are masked data. Error bars represented the standard deviations of five probes.

Linear fitting: $\log(I_{882}/I_{996})=a+b*\log[H_2O_2]$					
pH	Linear range (mol/L)	a-intercept	b-slope	R^2	LOD
4	10^{-2} to 10^{-4}	-0.134	0.342	0.990	48 μM
5	10^{-2} to 10^{-5}	-0.103	0.289	0.969	5.8 μM
6	10^{-2} to 10^{-5}	0.052	0.293	0.983	3.9 μM
7	10^{-2} to 10^{-6}	0.141	0.254	0.981	0.77 μM
8	10^{-2} to 10^{-6}	0.210	0.245	0.961	0.42 μM
9	10^{-2} to 10^{-7}	0.229	0.218	0.956	45 nM

Table SI-2: Calibration curves equations and LODs of NCs@3-MPBA&4-MBA for H_2O_2 in phosphate buffer with pH ranging from 4 to 9.

3.7.5 Section 5: Intracellular and extracellular H_2O_2 monitoring with NCs@3-MPBA

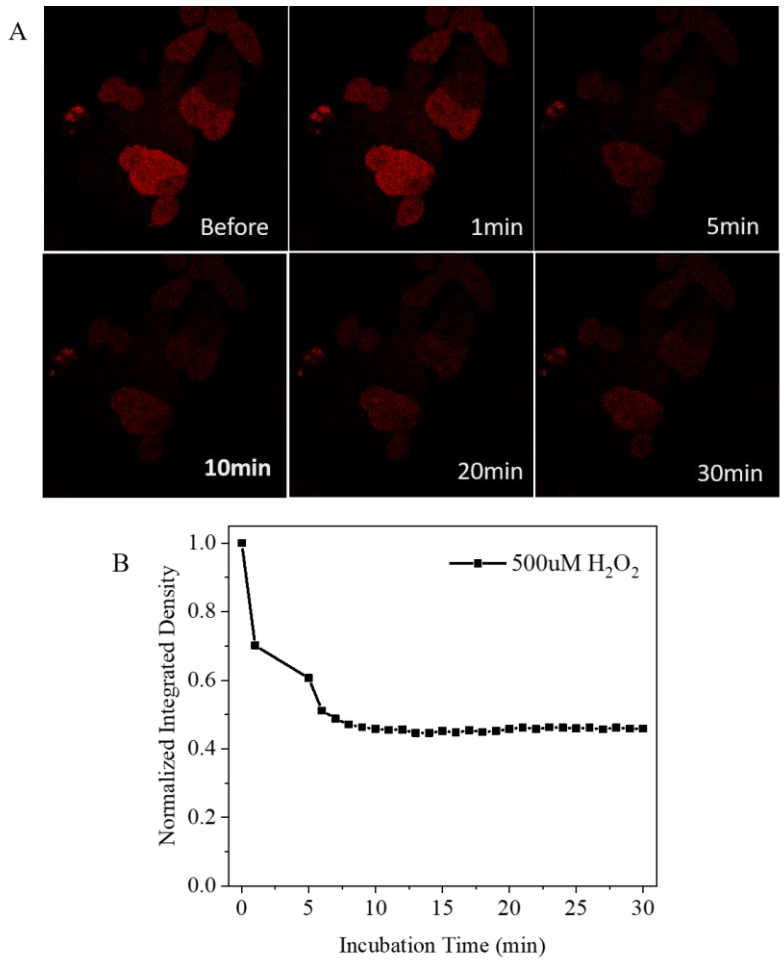

Figure SI-13: Intracellular H_2O_2 level changes by adding H_2O_2 and visualized with orp1-GFP. (A) confocal images of orp1-GFP transfected HT29 (MOI 80): before and after 0.5 mM H_2O_2 addition 1 min, 5 min, 10 min, 20 min and 30 min; (B) Integrated density calculated with ImageJ before and after 0.5 mM H_2O_2 addition. The decrease went into a platform after 10 min.

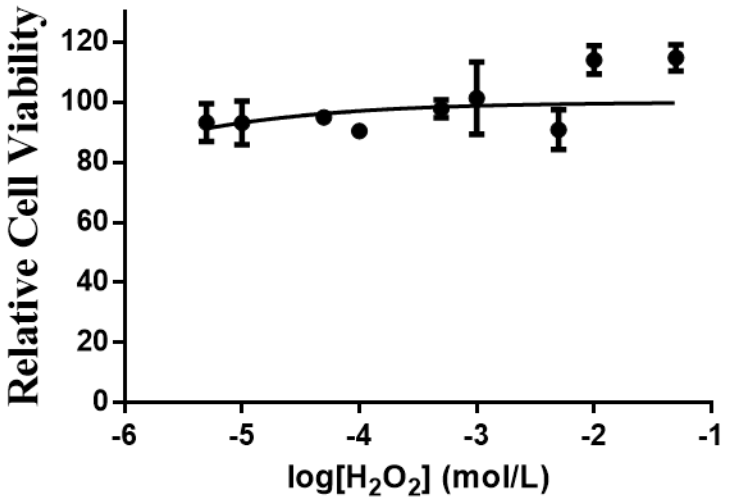

Figure SI-14: Viability test of H_2O_2 treated HT29 with Resazurin. Cell viability was determined by Resazurin-Based Assay after the H_2O_2 addition 30 min, with H_2O_2 concentration $5X10^{-2}$ M, 10^{-2} M, $5X10^{-3}$ M, 10^{-3} M, $5X10^{-4}$ M, 10^{-4} M, $5X10^{-5}$ M, 10^{-5} M, $5X10^{-6}$ M. Mitochondria activity increased under H_2O_2 stimulation.

$[H_2O_2]$	Stained Cells	Total Cells	Percentage of living cells
10^{-1} M	**108**	**250**	**56.8%**
10^{-2} M	**24**	**263**	**90.9%**
10^{-3} M	**19**	**350**	**94.6%**
10^{-4} M	**21**	**367**	**94.3%**
0	**7**	**130**	**94. 9%**

Table SI-3: Viability test of H_2O_2 treated HT29 with Trypan blue to check cellular membrane integrity.

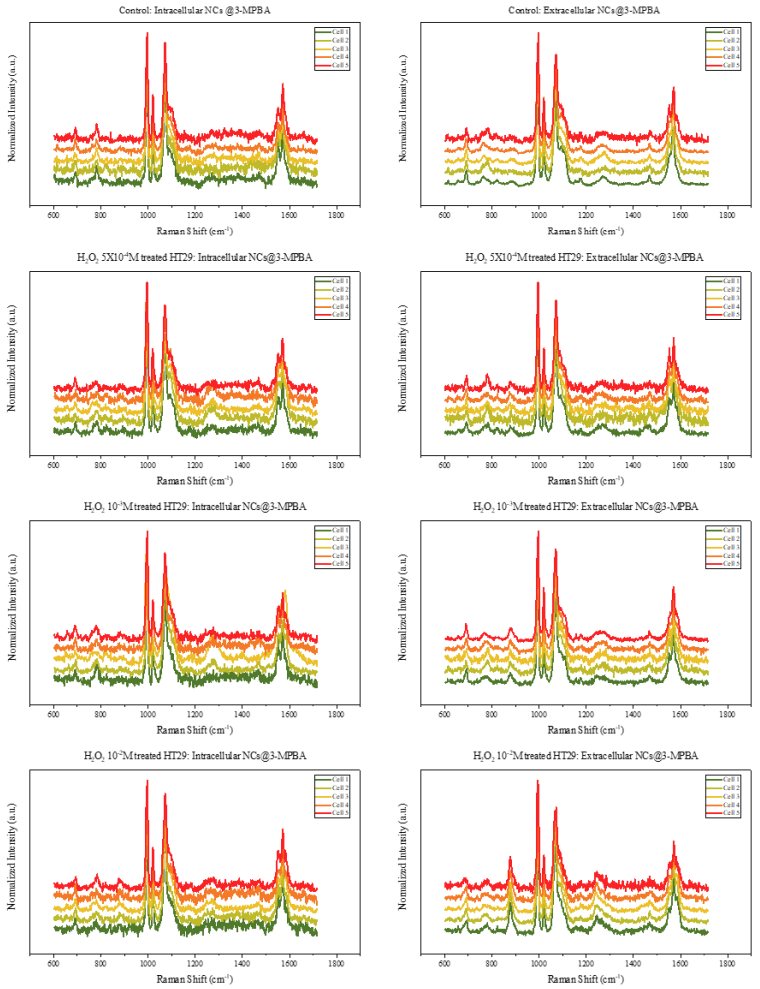

Figure SI-15: SERS spectra of intracellular and extracellular NC@3-MPBA of HT29 with different amount of H_2O_2 treatment (10 mM, 1 mM, 0.5 mM) and without H_2O_2 addition. Each spectrum was collected with one NCs@3-MPBA.

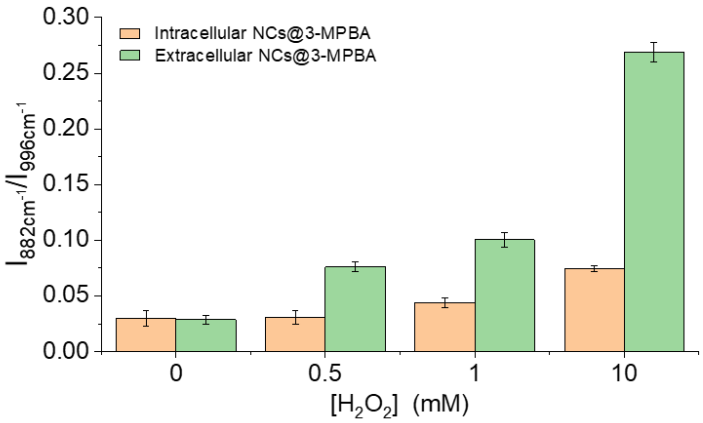

Figure SI-16: Intracellular and extracellular NCs@3-MPBA for H_2O_2 sensing. I_{882}/I_{996}, for local H_2O_2 detection, were calculated of intracellular and extracellular NCs@3-MPBA of HT29 with different amount of H_2O_2 treatment (10 mM, 1 mM, 0.5 mM) and without H_2O_2 addition. Each column was the average of 5 different probes.

3.7.6 Section 6: Intracellular and extracellular H_2O_2 and pH monitoring with NCs@3-MPBA&4-MBA

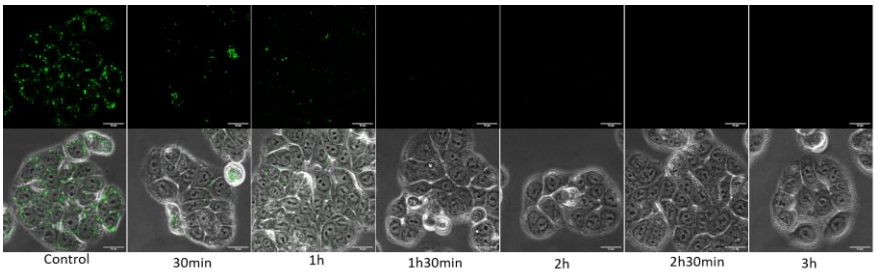

Figure SI-17: 500 nM Bafilomycin A1 treated HT29 lysosomal pH changes visualized by lysotracker (in green). After Bafilomycin A1 500 nM treated 2h, there was no signals coming from lysotracker.

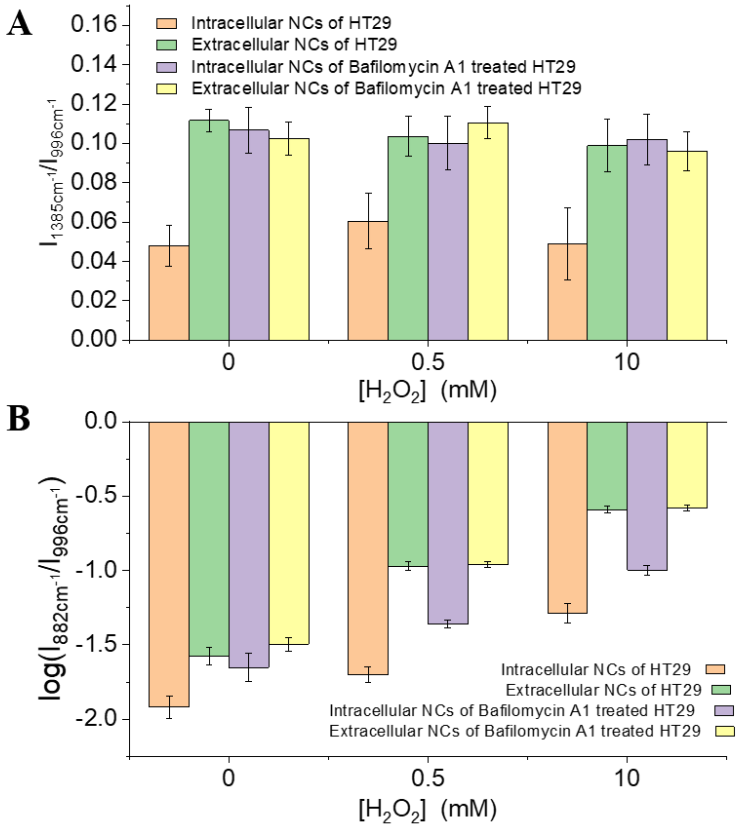

Figure SI-18: Intracellular and extracellular NCs@3-MPBA&4-MBA for pH and H_2O_2 detection of Bafilomycin A1 and/or H_2O_2 treated and non-treated HT29. (A) I_{1385}/I_{996}, for local pH determination, were calculated of intracellular and extracellular NCs@3-MPBA&4-MBA of HT29 under different treatments: Bafilomycin A1 treated and non-treated HT29 with different amount of H_2O_2 addition (10mM, 0.5mM) and without H_2O_2 addition. Each column was the average of 5 different probes. (B) $\log(I_{882}/I_{996})$ for local H_2O_2 detection, were calculated of intracellular and extracellular NCs@3-MPBA&4-MBA of HT29 under different treatments: Bafilomycin A1 treated and non-treated HT29 with different amount of H_2O_2 addition (10mM, 0.5mM) and without H_2O_2 addition. Each column was the average of 5 different probes.

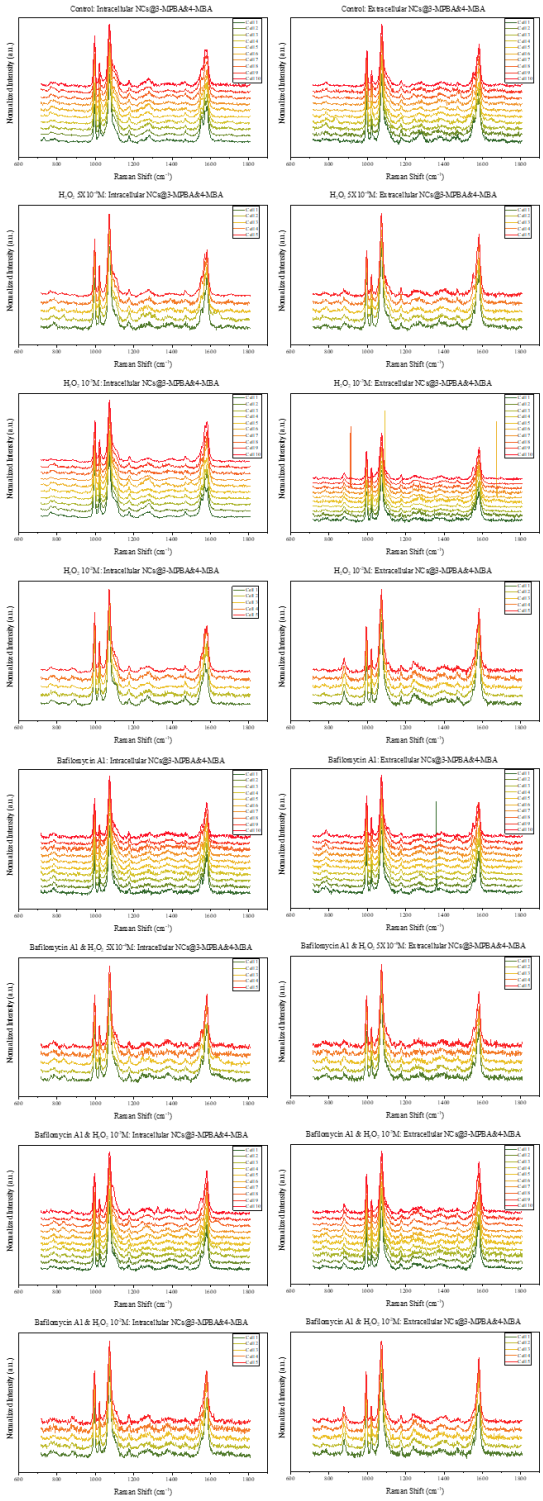
Control: Intracellular NCs@3-MPBA&4-MBA
Control: Extracellular NCs@3-MPBA&4-MBA
H2O2 5X10-3M: Intracellular NCs@3-MPBA&4-MBA
H2O2 5X10-3M: Extracellular NCs@3-MPBA&4-MBA
H2O2 10-3M: Intracellular NCs@3-MPBA&4-MBA
H2O2 10-3M: Extracellular NCs@3-MPBA&4-MBA
H2O2 10-3M: Intracellular NCs@3-MPBA&4-MBA
H2O2 10-3M: Extracellular NCs@3-MPBA&4-MBA
Bafilomycin A1: Intracellular NCs@3-MPBA&4-MBA
Bafilomycin A1: Extracellular NCs@3-MPBA&4-MBA
Bafilomycin A1 & H2O2 5X10-3M: Intracellular NCs@3-MPBA&4-MBA
Bafilomycin A1 & H2O2 5X10-3M: Extracellular NCs@3-MPBA&4-MBA
Bafilomycin A1 & H2O2 10-3M: Intracellular NCs@3-MPBA&4-MBA
Bafilomycin A1 & H2O2 10-3M: Extracellular NCs@3-MPBA&4-MBA
Bafilomycin A1 & H2O2 10-3M: Intracellular NCs@3-MPBA&4-MBA
Bafilomycin A1 & H2O2 10-3M: Extracellular NCs@3-MPBA&4-MBA
Normalized Intensity (a.u.)
Raman Shift (cm-1)

Figure SI-19: Intracellular and extracellular SERS spectra of NCs@3-MPBA&4-MBA with HT29 under different treatments: Bafilomycin A1 treated and non-treated HT29 with different amount of H_2O_2 addition (10 mM, 1 mM and 0.5 mM) and without H_2O_2. Each spectrum was collected with one NCs@3-MPBA&4-MBA.

	C-I		C-E		B-I		B-E		H3-I		H3-E		BH3-I		BH3-E	
	pH	H_2O_2	pH	H_2O_2	pH	H_2O_2	pH	H_2O_2	pH	H_2O_2	pH	H_2O_2	pH	H_2O_2	pH	H_2O_2
Cell 1	6	<4E-6	7	<8E-7	7	<8E-7	7	<8E-7	5	7.E-06	7	1.E-04	7	4.E-06	7	8.E-05
Cell 2	6	<4E-6	7	<8E-7	7	<8E-7	7	<8E-7	5	7.E-06	7	2.E-04	7	5.E-06	7	9.E-05
Cell 3	5	<6E-6	7	<8E-7	7	<8E-7	7	<8E-7	5	9.E-06	7	2.E-04	7	5.E-06	7	1.E-04
Cell 4	6	<4E-6	7	<8E-7	7	<8E-7	7	<8E-7	6	7.E-06	7	3.E-04	7	6.E-06	7	1.E-04
Cell 5	5	<6E-6	7	<8E-7	7	<8E-7	7	<8E-7	6	9.E-06	7	3.E-04	7	7.E-06	7	2.E-04
Cell 6	6	<4E-6	7	<8E-7	7	<8E-7	7	<8E-7	6	9.E-06	7	3.E-04	7	7.E-06	7	3.E-04
Cell 7	6	<4E-6	7	<8E-7	7	<8E-7	7	<8E-7	6	9.E-06	7	3.E-04	7	7.E-06	7	3.E-04
Cell 8	6	<4E-6	7	<8E-7	7	<8E-7	7	<8E-7	6	9.E-06	7	3.E-04	7	9.E-06	7	3.E-04
Cell 9	6	<4E-6	7	<8E-7	7	<8E-7	7	<8E-7	6	1.E-05	7	5.E-04	7	9.E-06	7	4.E-04
Cell 10	6	<4E-6	7	<8E-7	7	<8E-7	7	<8E-7	6	1.E-05	7	6.E-04	7	9.E-06	7	5.E-04
Average	6	<4E-6	7	<8E-7	7	<8E-7	7	<8E-7	6	9.E-06	7	3.E-04	7	7.E-06	7	2.E-04

	H2-I		H2-E		BH2-I		BH2-E		H4-I		H4-E		BH4-I		BH4-E	
	pH	H_2O_2	pH	H_2O_2	pH	H_2O_2	pH	H_2O_2	pH	H_2O_2	pH	H_2O_2	pH	H_2O_2	pH	H_2O_2
Cell 1	6	2.E-05	7	1.E-03	7	2.E-05	7	1.E-03	6	<4E-6	7	3.E-05	7	1.E-06	7	4.E-05
Cell 2	6	3.E-05	7	1.E-03	7	3.E-05	7	1.E-03	6	<4E-6	7	4.E-05	7	1.E-06	7	4.E-05
Cell 3	5	4.E-05	7	1.E-03	7	3.E-05	7	1.E-03	6	<4E-6	7	4.E-05	7	1.E-06	7	4.E-05
Cell 4	6	4.E-05	7	1.E-03	7	4.E-05	7	2.E-03	6	<4E-6	7	5.E-05	7	2.E-06	7	5.E-05
Cell 5	6	5.E-05	7	2.E-03	7	5.E-05	7	2.E-03	5	<6E-6	7	5.E-05	7	2.E-06	7	6.E-05
Average	6	4.E-05	7	1.E-03	7	3.E-05	7	1.E-03	6	<4E-6	7	4.E-05	7	1.E-06	7	5.E-05

Table SI-4: Intracellular and extracellular pH and H_2O_2 concentration calculated based on calibration curve of all the NCs@3-MPBA&4-MBA determined. Intracellular and extracellular SERS spectra were collected with HT29 under different treatments. C-I: intracellular probes of blank HT29; C-E: extracellular probes of blank HT29; B-I: intracellular probes of Bafilomycin A1 treated HT29; B-E: extracellular probes of Bafilomycin A1 treated HT29; H3-I: intracellular probes of 1 mM H_2O_2 treated HT29; H3-E: extracellular probes of 1 mM H_2O_2 treated HT29; BH3-I: intracellular probes of Bafilomycin A1 and 1 mM H_2O_2 treated HT29; BH3-E: extracellular probes of Bafilomycin A1 and 1 mM H_2O_2 treated HT29; H2-I: intracellular probes of 10 mM H_2O_2 treated HT29; H2-E: extracellular probes of 10 mM H_2O_2 treated HT29; BH2-I: intracellular probes of Bafilomycin A1 and 10 mM H_2O_2 treated HT29; BH2-E: extracellular probes of Bafilomycin A1 and 10 mM H_2O_2 treated HT29; H4-I: intracellular probes of 0.5 mM H_2O_2 treated HT29; H4-E: extracellular probes of 0.5 mM H_2O_2 treated HT29; BH4-I: intracellular probes of Bafilomycin A1 and 0.5 mM H_2O_2 treated HT29; BH4-E: extracellular probes of Bafilomycin A1 and 0.5 mM H_2O_2 treated HT29.

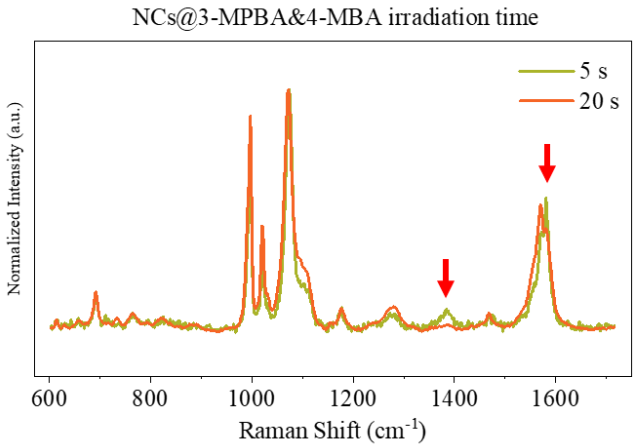

Figure SI-20: SERS spectra of NCs@3-MPBA&4-MBA (3-MPBA $5X10^{-3}$M and 4-MBA 10^{-3}M for modification) in pH 9 phosphate buffered saline under different irradiation time (5s and 20s) with laser power 5 mW. Spectra were collected from same particle. Red arrows indicate 4-MBA peaks at 1385 cm^{-1} and 1590 cm^{-1}.

4. CONCLUSIONS

This thesis focused on the multiplex nanosensors for intracellular hydrogen peroxide and pH quantification. This work was motivated by the challenges on facile devices for intracellular hydrogen peroxide and pH monitoring for potential diseases understanding and diagnosis. To conclude the thesis, the main conclusions are listed as follow:

1. We found that it was critical to control the system pH for thiolated molecules modification onto metallic surfaces. Alkaline environment facilitates the deprotonation of thiol group, thus increases the thiol-metal bond formation speed. While, dissociation of thiolated molecules can be favored in strong basic environment, which will affect the packing quality of thiolated molecules. We also found that solvent has moderate effect on final modification. The quality of Raman label modification will be affected by the bonding speed, the electrostatic repulsion on the metallic surface and the competition between Raman label and stabilizer.

2. Hot spots are critically important for designing one SERS platform, which could dramatically increase Raman enhancement. With controlled agglomeration, we managed to increase the SERS efficiency of silver-silica core-shell nanostructure up to 40 times. Followed by a protecting silica layer, this nanostructure performed robust Raman signal. The robustness test was conducted by depositing this nanostructure on different materials, resulting in robust, stable and non-interfered SERS signal.

3. This silica layer also provide the opportunities for multi-functionalization of nanostructure with biomolecules. This designed nanostructure (silver-silica nanoparticles) were used for SARS-CoV-2 spike protein detection with SERS-based ELISA assay, which combined the selectivity of immunoassay and the sensitivity of SERS. This detail protocol can be potentially applied to *in vitro* biodiagnosis.

4. Based on the knowledge we obtained for the design and synthesis of a robust silver-silica nanostructure, we moved forward to select and synthesize gold silica nanocapsules for *in vitro* hydrogen peroxide and pH multiplex sensing. The nanocapsules act as a robust SERS platform which confined gold nanoislands inside the protected cavity producing interparticle hot spots.

5. 3-mercaptophenylboronic acid and 4-mercaptobenzoic acid modified nanocapsules were established for intracellular hydrogen peroxide and pH quantification. Internalized nanocapsules were located inside endosomes with a range of acidic pH. The complexation of a third hydroxyl group in 3-mercaptophenylboronic acid under alkaline pH facilitates this B-C bond rupture. The equilibrium constants of 3-mercaptophenylboronic acid oxidation by hydrogen peroxide vary with environmental pH. Simultaneous detection of hydrogen peroxide and pH not only offers more information about one sample, but also ensures the accurate hydrogen peroxide readout.

6. The performance of the multiplex nanosensors were verified with HT29 (colon cancer cells). We tuned the intracellular hydrogen

peroxide amount by adding different concentrations of hydrogen peroxide directly to the growth media, and changed the lysosomal pH by incubating Bafilomycin A1 with nanoparticles internalized cells. The changes in pH and hydrogen peroxide were monitored with internalized nanocapsules based on SERS.

7. We found the extracellular hydrogen peroxide was not the same as the one-shot addition concentration, because of the active metabolism of cells, and the value was around 5 to 10 times lower. Also there are gradients between intracellular and extracellular hydrogen peroxide. The gradient was estimated around 40 times lower from the intracellular to the extracellular concentrations. Meanwhile, although the nanocapsules might be located in different organelles of endocytic pathways with different luminal acidity (lysosomes, endosomes), the concentrations of hydrogen peroxide were equivalent.